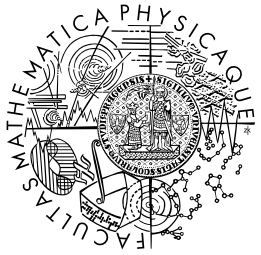

FACULTY
OF MATHEMATICS
AND PHYSICS
Charles University

DOCTORAL THESIS

Mgr. Peter Ondáč

Experimental Investigation of the Anode Area in the Hybrid Water-Gas DC Arc Plasma Torch

Department of Surface and Plasma Science

Supervisor of the doctoral thesis: doc. RNDr. Milan Hrabovský, CSc.

Study programme: Physics

Study branch: Physics of Plasma and Ionized Media

Prague 2020

I declare that I carried out this doctoral thesis independently, and only with the cited sources, literature and other professional sources.

I understand that my work relates to the rights and obligations under the Act No. 121/2000 Sb., the Copyright Act, as amended, in particular the fact that the Charles University has the right to conclude a license agreement on the use of this work as a school work pursuant to Section 60 subsection 1 of the Copyright Act.

In ..... date ....

Author's signature

I would like to thank everybody who helped me any way in the development of this thesis.

I am especially grateful to my kind supervisor Doc. Milan Hrabovský, who secured employment for me in the Institute of Plasma Physics AS CR, without which the writing of the thesis would have been more protracted. He has answered a lot of my questions about the physics behind the hybrid plasma torch and directed my work at the beginning of my doctoral study. He carefully checked and provided valuable feedback to my two most important physics articles and to this thesis. Over the last two years, I received a salary at the Institute thanks to the new head of the Plasma Chemical Technologies department, Dr. Michal Jeremiáš.

I was very fortunate to have the chance to work with physicists from the Institute of Plasma Physics throughout my study at Charles University. I am especially thankful to my colleague Dr. Alan Mašláni (Deputy head of the Plasma Chemical Technologies department), who has devoted much of his energy to me, especially during my early days at the Institute. He helped me with his honest, peaceful and human approach. He also assisted a lot of my experiments at the department. My colleague Ing. Václav Březina answered a lot of my questions about the hybrid plasma torches and he operated the plasma torches during my experiments, often together with Ing. Petr Brom. My two colleagues Mr. Petr Filip and Mr. Antonín Musil helped me with the preparation of electric circuits for my measurements. I also thank Mr. Michal Boušek and Dr. Jiří Adámek, from the Tokamak Department, for making the used electric probes.

I would like to thank Prof. Jana Šafránková for organizational matters connected with the thesis. She also gave me a valuable feedback to this thesis, together with Prof. Zdeněk Němeček. My thanks belong also to the whole Department of Surface and Plasma Science at Charles University for developing my knowledge of plasma physics.

My access to computing and storage facilities owned by parties and projects contributing to the National Grid Infrastructure MetaCentrum, provided under the programme "Projects of Large Infrastructure for Research, Development, and Innovations" (LM2010005), is appreciated.

The thesis is dedicated to the whole Universe.
That means it is dedicated to Me as well as to You.

Title: Experimental Investigation of the Anode Area in the Hybrid Water-Gas DC Arc Plasma Torch

Author: Mgr. Peter Ondáč

Department: Department of Surface and Plasma Science

Supervisor: doc. RNDr. Milan Hrabovský, CSc., Plasma Chemical Technologies

Abstract: This thesis focuses on an experimental study of the anode area of the hybrid water-gas DC arc plasma torch that is used in many industrial applications, including plasma spraying, hydrocarbon reforming, pyrolysis, and organic waste gasification. The effects of ambient pressure and plasma generation conditions on the torch's plasma jet were studied, with particular focus on the torch's anode area. Movement of the anode arc attachment is described in detail, including its speed, range of its motion on the anode surface, restrike periods, and the frequency of its many sudden decelerations and re-accelerations. It was found that the anode erosion can be compared relatively simply by quick processing of high-speed camera videos. The anode erosion was also measured directly. Many electric probe measurements were made in the anode area of this plasma torch for the first time. By using these electric probes, shock waves, turbulent vortices, and plasma potential fluctuations were studied directly. It was found that a mean plasma electric field and a mean plasma electrical conductivity in the anode area can be satisfactorily estimated also non-intrusively by quick processing of high-speed camera videos. Moreover, schlieren videos of the plasma jet in the anode area were created.

Keywords: DC arc plasma torch, Anode area, High-speed camera, Anode arc attachment, Anode erosion

Contents

1. Introduction

A hybrid water-gas DC arc plasma torch is a device that can be used in many industrial applications, such as organic waste gasification [1–4], pyrolysis, hydrocarbon reforming [5], and plasma spraying [6]. This device was invented in Prague at the Institute of Plasma Physics of the Czech Academy of Sciences (IPP CAS), in 1996. Its main characteristics and properties are detailed, for example, in [7, 8]. The torch has a DC (direct current) electric arc stabilized by a gas flow and water vortex, and the arc creates plasma from this gas and water. The plasma flows outside the torch because of the pressure gradient and the flow of the plasma outside the torch is termed the plasma jet.

1.1 Thesis overview

The thesis is structured into six chapters, with this Introduction being the first.

Chapter 2 provides an overview of relevant theory that is the most critical to this work. The *DC electric arc* and *Hybrid water-gas DC arc plasma torch* sections describe the hybrid plasma torches and their principle. The primary characteristics of the plasma created by these plasma torches are described in *Thermal plasma* section. The *schlieren photography* section describes a not very familiar schlieren diagnostic, used in this work. The plasma flow created by the hybrid plasma torch is turbulent and sometimes supersonic.

Necessary information about that turbulence and supersonic structure of the flow is mentioned in the *Turbulence* and *Supersonic flow* sections. Enthalpy probe diagnostics and the entrainment process, which are also mentioned in this thesis, are satisfactorily described in the Ph.D. thesis of Kavka [9]. The interpretation of the electric probes' measurements often leads to Langmuir probe theory; therefore the main idea of this theory is reminded in the *Langmuir probe theory* section, and the interested reader can find more details of this theory in the master thesis of Ondac [10].

Chapter 3 outlines the experimental setup, measuring instruments, and working conditions that we used for this study. Consequently, **chapter 4** summarizes the methods that we used and how we estimated the uncertainties in the measured data.

Chapter 5 provides measured data about the size of turbulence vortices, an average hydrodynamic wave speed, pressures for the transition between a constricted and a diffuse anode arc attachment and between subsonic and supersonic plasma flow, the average attachment speed, the range of the attachment movement on the anode, average periods of the attachment movement in the restrike mode, anode weight loss, the frequency of the attachment's sudden decelerations and re-accelerations, probe potential fluctuations, the electric field in the plasma, and a mean electrical conductivity of the arc in the anode area; all at different arc

currents, different ambient pressures, different argon flows, and different anode's position. The discussion of the results is included in this chapter also.

The chapter focuses on the dependence of the measured variables on the working conditions, and on the mutual comparisons of the measured variables; that is to say on physical phenomena, not on the absolute values of the measured variables. For example, if we have an ambient pressure dependence of an average anode arc attachment speed, the absolute values in the corresponding graph are not crucial because they can be measured differently in different experiments.

The absolute values can be measured differently in the same working conditions because the inside of the hybrid plasma torch changes after each experiment (due to the diameter of the vortex chambers inside the torch, deposits in the input tangential openings or suctions slots, etc.). But, for example, the finding that the average anode arc attachment speed increases with decreases in ambient pressure should be the same for all experiments under the same working conditions.

Chapter 6 summarizes the main conclusions and findings of the thesis.

1.2 Goals of the thesis

This thesis focuses on an experimental study of the anode area of a hybrid water-gas plasma torch. The anode area is the part of the plasma flow in the horizontal distance of about 0-25 mm downstream from the torch's exit nozzle. Characteristics of the plasma created by the hybrid plasma torch depend mainly on processes that occur in its anode area, and these processes are crucial in the practical applications of the torch.

The three main goals of this thesis:

- to present new discoveries about the physical phenomena that were investigated and processes in the anode area, such as transitions between different arc modes, anode arc attachment movement, anode erosion, transitions between subsonic and supersonic plasma flow, transitions between different types of the anode arc attachment, and creation of instabilities in the plasma;
- to provide experimental data for future modeling of the anode area, not only of the hybrid plasma torch but also of water and gas plasma torches;
- to reveal new possibilities for a more detailed future investigation of the anode area.

These goals were pursued by using a high-speed camera, electric probes, and other measuring instruments to measure:

- the speed of the anode arc attachment;
- periods of the attachment's movement;
- the frequency of the attachment's sudden decelerations and re-accelerations;

- the range of the attachment's movement on the anode;
- anode weight loss;
- plasma potential fluctuations;
- the electric field, and;
- a mean/bulk plasma electrical conductivity.

The attached MATLAB scripts show how to calculate the statistical characteristics of the anode arc attachment movement by using videos filmed with a high-speed camera.

2. Theoretical background

This chapter consists of seven sections. The first two sections describe the used hybrid water-gas plasma torches and their main principle. The third section describes the thermal plasma created by the hybrid or water plasma torches, which is investigated in this thesis.

The fourth and fifth section very briefly describes the two essential aspects of the plasma flow created by the hybrid plasma torch. The plasma flow investigated in this thesis is always turbulent and sometimes supersonic. The accompanying phenomenon, called the entrainment process, is satisfactorily well described in the Ph.D. thesis of Kavka [9].

From all the measuring instruments we used, (listed in the next chapter), two require a theoretical background: a system for schlieren imaging, and electric probes. Schlieren photography is described in the sixth section. Electric probes that we used require a continuum probe theory or a hybrid theory [11]; however, in this thesis we only used ideas from the Langmuir probe theory, which is briefly mentioned in the seventh section. The details about the plasma sheath created around the probe's tips can be found, for example, in the master thesis of Ondac [10].

The enthalpy probe system mentioned in this thesis needs a theoretical background too; however, in this work we have not processed any data measured by enthalpy probes. Therefore, understanding measurements with enthalpy probes is not essential here, and the interested reader is referred to the Ph.D. thesis of Kavka [9], where the enthalpy probe system is described in detail.

2.1 DC electric arc

The DC electric arc is a direct electric current that flows between an anode and a cathode, and it has three parts (Fig. 2.1):

a) the cathode region,

b) the arc column, and

c) the anode region.

The arc column is a true plasma that approaches LTE (Local Thermodynamic Equilibrium) in a high-intensity arc that has arc current $I > 50$ A and pressure $p > 10$ kPa. A typical distribution of the electric potential along an electric arc is shown in Fig. 2.1.

As in the case of sausage instability [13], any variation of the current-carrying cross section of the arc leads to induced macroscopic flows inside the arc, due to electromagnetic pinch forces (Fig. 2.2). A typical example of this phenomenon is the cathode jet or anode jet, described by Maecker et al. [14].
In a plasma created by a DC arc plasma torch, the arc is connected with the anode by a so-called anode arc attachment (sometimes it is termed the arc root),

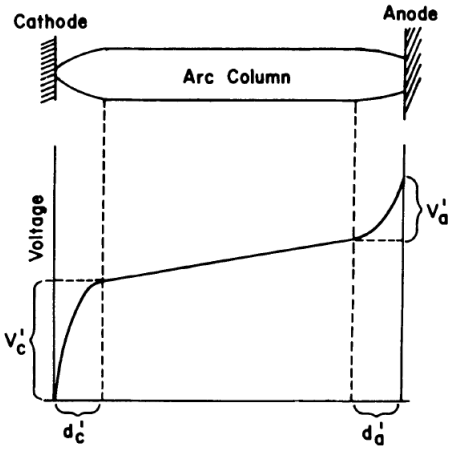

Figure 2.1: Potential distribution along an electric arc [12]

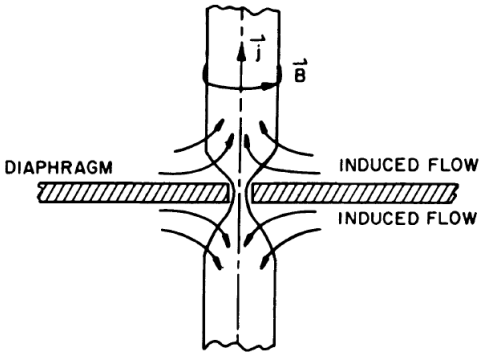

Figure 2.2: Flows induced by arc constriction [12]

and it can have two different forms: constricted and diffuse (Fig. 2.3). The constricted anode arc attachment has a high current density and is used in most cases. The diffuse anode arc attachment has a low current density and a large region on the anode surface.

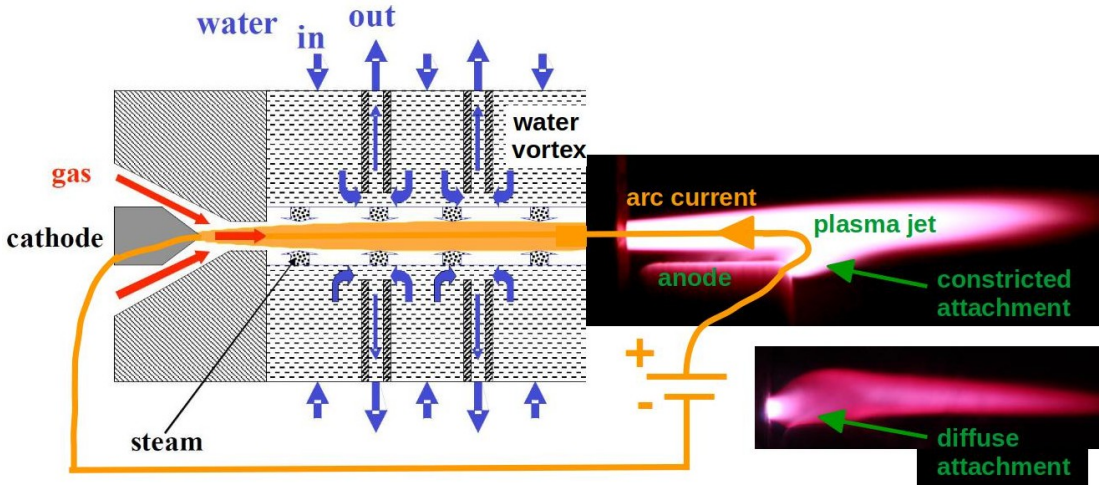

Figure 2.3: Schematics of the electric arc in the hybrid water-gas DC arc plasma torch. The two camera images on the right show a constricted and diffuse anode arc attachment. The image with the diffuse attachment is not part of the schematics

There are three arc modes: restrike, steady, and takeover [15–17]. In the restrike (reattachment) mode, the constricted attachment moves downstream along the anode's surface and suddenly restrikes nearer to the exit nozzle because of an electric breakdown. This process repeats itself, and the corresponding arc voltage waveform is therefore sawtooth-shaped. Rat *et al.* summarized the up-to-date knowledge about the restrike mode in [18].

The position of the constricted anode attachment on the anode surface determines the arc length and consequently the arc voltage and power. In the takeover mode, the anode arc attachment oscillates forth and back along the anode surface, producing a more or less regular sinusoidal voltage waveform on an

oscilloscope [16]. The steady mode is characterized by a fixed location of the anode arc attachment. The two forces act on the constricted anode arc attachment: A dynamic drag force $\boldsymbol{F_D}$ acts in the downstream direction because of the plasma flow above the attachment. The plasma flow is a result of the pressure gradient along the arc. A magnetic Lorentz force $\boldsymbol{F_L}$ acts on the attachment downstream in an upper arc current curvature and upstream in a lower arc current curvature near the anode surface. Both forces are estimated in [15, 19] and discussed in sections 5.2 and 5.3 (they are depicted in Fig. 5.11).

An anode jet arises from the constricted anode attachment into the arc in the direction of the attachment and significantly influences the stability of the main plasma flow created by the arc. The interaction of the anode jet with flowing plasma causes instabilities and flow disturbances propagating through the plasma. This fact was observed in the water plasma torch [20–22] and other non-transferred arc plasma torches [23]. Ghorui *et al.* [24] outlined the correlation between the arc voltage fluctuations and dynamics of the anode arc attachment in a non-transferred air DC arc plasma torch.

For stable operation, the arc must be stabilized by a stabilizing mechanism that keeps the arc column in a stable position (not necessarily in a stationary one). Whenever the arc column accidentally moves from its equilibrium position, the stabilizing mechanism forces the arc column to return to its equilibrium position by interaction with the arc column. The stabilizing mechanism can be for example a magnetic field, a solid wall, a gas vortex, or a water vortex.

For instance, in the case of a solid wall and a water vortex, any accidental excursion of the arc column into the stabilizing medium increases heat conduction to the medium and consequently reduces the temperature and, therefore, the electrical conductivity of the plasma in the unstable location. The decrease of the electrical conductivity close to the stabilizing medium forces the electric current to flow outside the stabilizing medium where the electrical conductivity is higher, that is to say the electric current is forced to flow again in its equilibrium position.

2.2 Hybrid water-gas DC arc plasma torch

The hybrid water-gas DC arc plasma torch (Fig. 2.4) is produced and used only in Prague and has been investigated only at the IPP CAS in Prague. Since the nineties, the hybrid plasma torch has been improved several times (through a few patents), and therefore, at the IPP CAS there are currently a few types of this plasma torch.

The results in this thesis were obtained from two types of the hybrid plasma torch. One type is a commercial version, with the abbreviation of WSP®-H 2011 (Hybrid Water-gas Stabilized Plasma torch developed in 2011), which was used in our measurements at atmospheric pressure (hereinafter referred to as 101 kPa) and its appearance in 2019 is shown in Fig. 2.5. This commercial hybrid plasma torch has been developed at the Thermal Plasma (TP) department of IPP CAS in collaboration with the ProjectSoft HK company, and it is also used in the Laboratory of Plasma Technologies (LPT) in Prague-Letnany for custom plasma spraying. In 2018, the TP department was transformed into the Plasma

Chemical Technologies department.

The second type of hybrid plasma torch, from which most of the results in this thesis were obtained, was used in a low-pressure chamber, at ambient pressures lower than atmospheric pressure (101 kPa). This second type does not have a commercial abbreviation, but for the purpose of this thesis, it can be called the WSP®-HR (Hybrid Water Stabilized Plasma torch inside a Reactor). The main difference between the WSP®-H 2011 and WSP®-HR is only in the part that stabilizes the arc by a water vortex (Fig. 2.4, Drawings). WSP®-HR is also a little smaller (including the anode) than WSP®-H 2011.

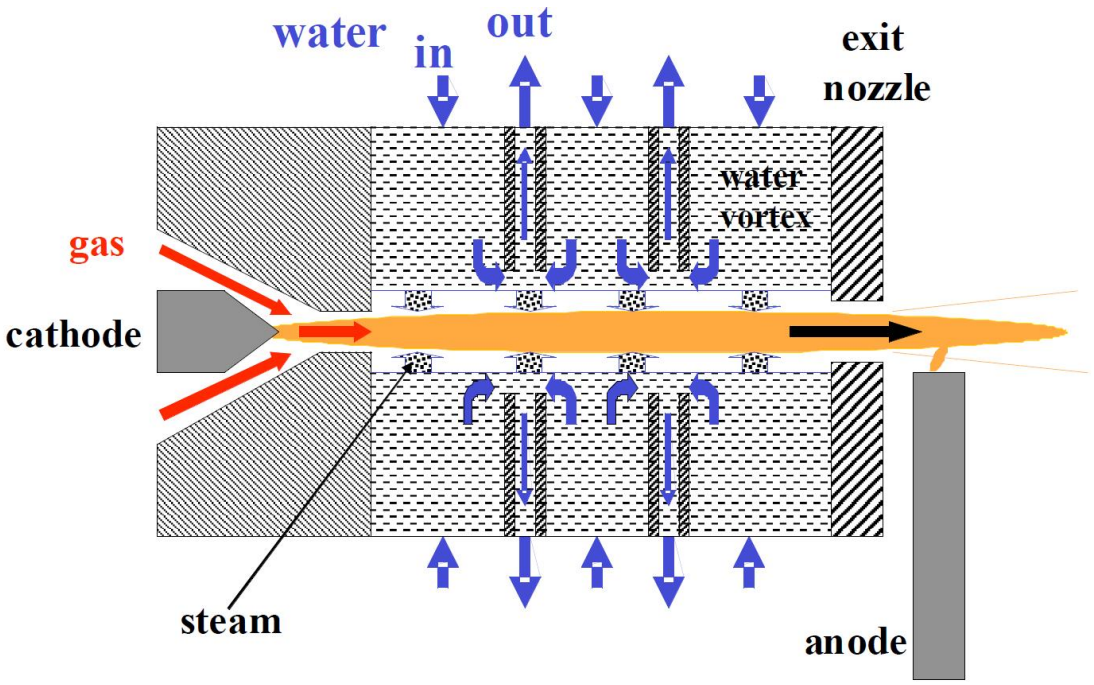

Figure 2.4: Schematics of a hybrid water-gas plasma torch [25]

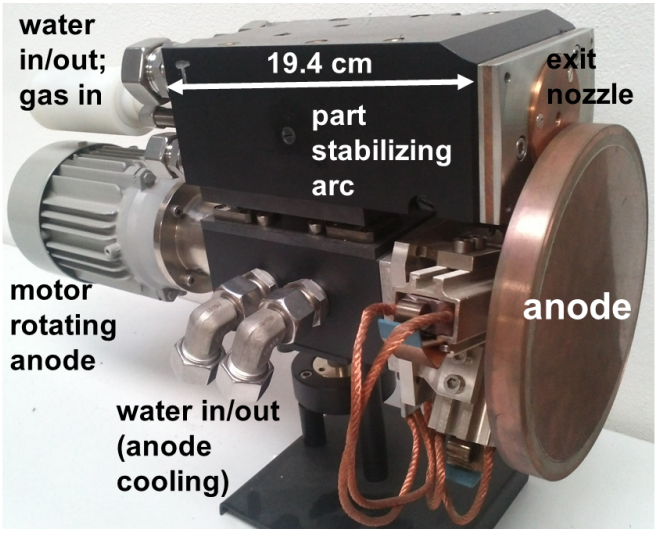

Figure 2.5: Image of WSP®-H 2011, in 2019

A plasma torch that stabilizes the electric arc by water vortex (put simply, a water stabilized plasma torch, Fig. 2.6), which is very similar to the hybrid plasma torch, was described in 1922, by Gerdien and Lotz [26], and experimentally investigated in the fifties, by Maecker [27] and others [28], [29], [30]. The water plasma torch was also investigated and improved at the TP department of IPP CAS before the hybrid plasma torch was designed. The type of water stabilized plasma torch called WSP® 500 (Water Stabilized Plasma, 500 A) (Fig. 2.7) is, together with the hybrid plasma torch, used in LPT for custom plasma spraying. Both water stabilized and hybrid water-gas stabilized plasma torches are so-called non-transferred plasma torches, with an external anode.

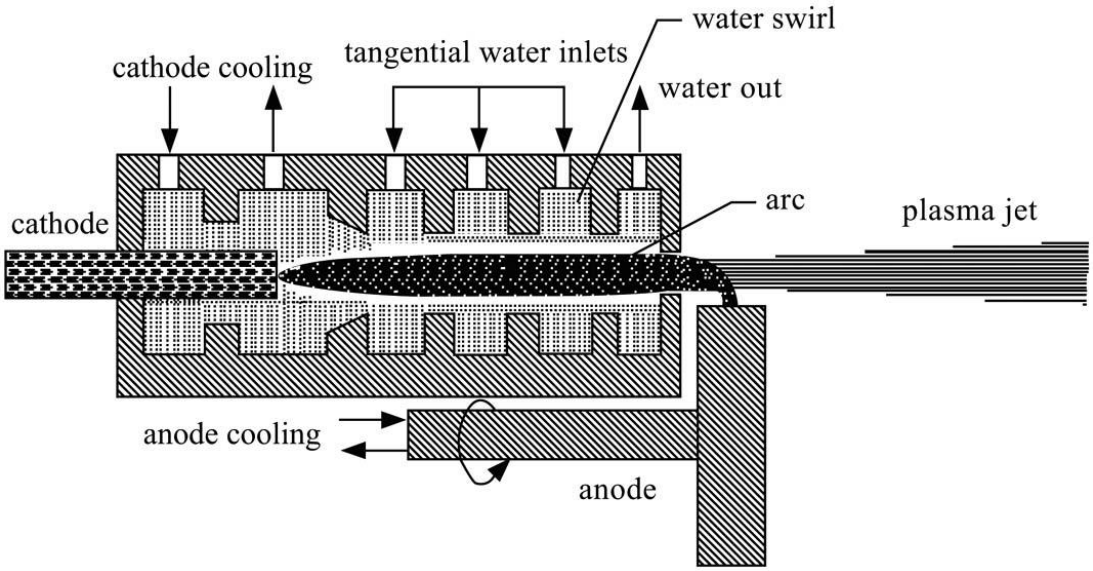

Figure 2.6: Schematics of a water stabilized plasma torch WSP [25]

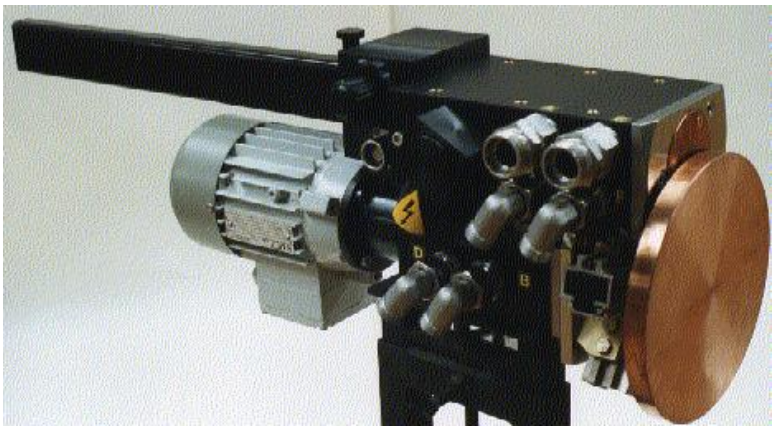

Figure 2.7: Image of the water stabilized plasma torch WSP 500 [31]

Plasma torches that stabilize the electric arc by flowing gas are very common and they are called gas plasma torches (Fig. 2.8). They are of no interest to this thesis, but they will be mentioned later a few times.

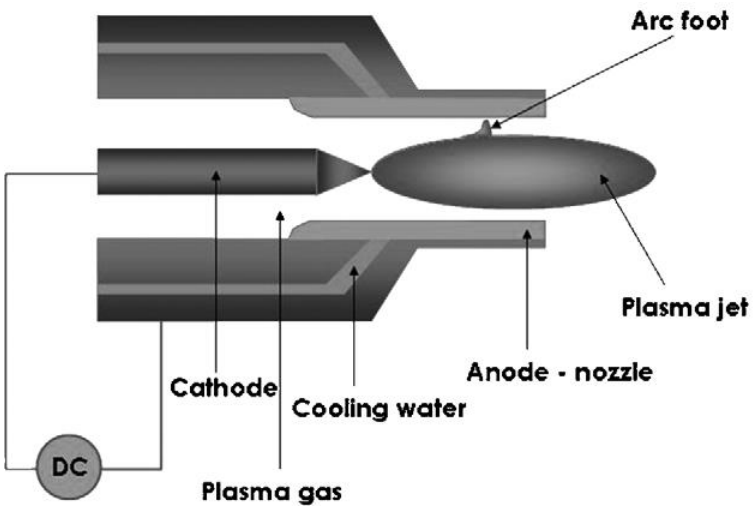

Figure 2.8: Schematics of a gas plasma torch. The "Arc foot" is often called the anode arc attachment [32]

The differences in the operation regime of the three types of plasma torches described above are shown in Fig. 2.9. The water stabilized plasma torches have a low mass flow rate of plasma because of the energy balances of heat transfer in the radial direction (direction from the axis of the plasma flow to the surrounding walls). But it can operate at substantially higher power than gas stabilized torches because the walls of the stabilizing cylinder are created by water (Fig. 2.6). The steam contained in the plasma has a high enthalpy and thermal conductivity and thus provides a high heat flux transferred to powder particles injected into the plasma flow during, for example, plasma spraying applications. On the other hand, the gas plasma torches have a high mass flow rate, which is a different advantage in plasma spraying applications.

In the hybrid water-gas plasma torch the principles of the arc stabilization by gas flow and water vortex are combined, and thus it can vary plasma jet characteristics in a wide range. The plasma flow velocity and mass flow rate in the plasma of a hybrid plasma torch can be varied by controlling the gas flow rate. However, the amount of steam in its plasma cannot be varied in a predefined way.

Processes in the anode area of hybrid or water plasma torches determine the lifetime of these torches or stability of their plasma flow, which is essential, for example in plasma spraying applications [6]. The fastest deterioration and material consumption happen at the anode surface. Therefore the anode erosion significantly reduces the lifetime of the plasma torch and leads to environmental contamination (which is undesirable, for example, in plasma spraying applications).

Generally we can find studies dealing with anode erosion of small anodes that are simultaneously exit nozzles of the corresponding torches [33, 34]. However, the anode erosion of hybrid and water plasma torches is still an unexplored phenomenon and has not been measured before. Processes in the anode area further determine the properties and flow characteristics of the plasma jet. For example, the length of the arc influences the thermal power of the plasma jet, and thermal power influences the effectiveness of hydrocarbon reforming and waste gasifica-

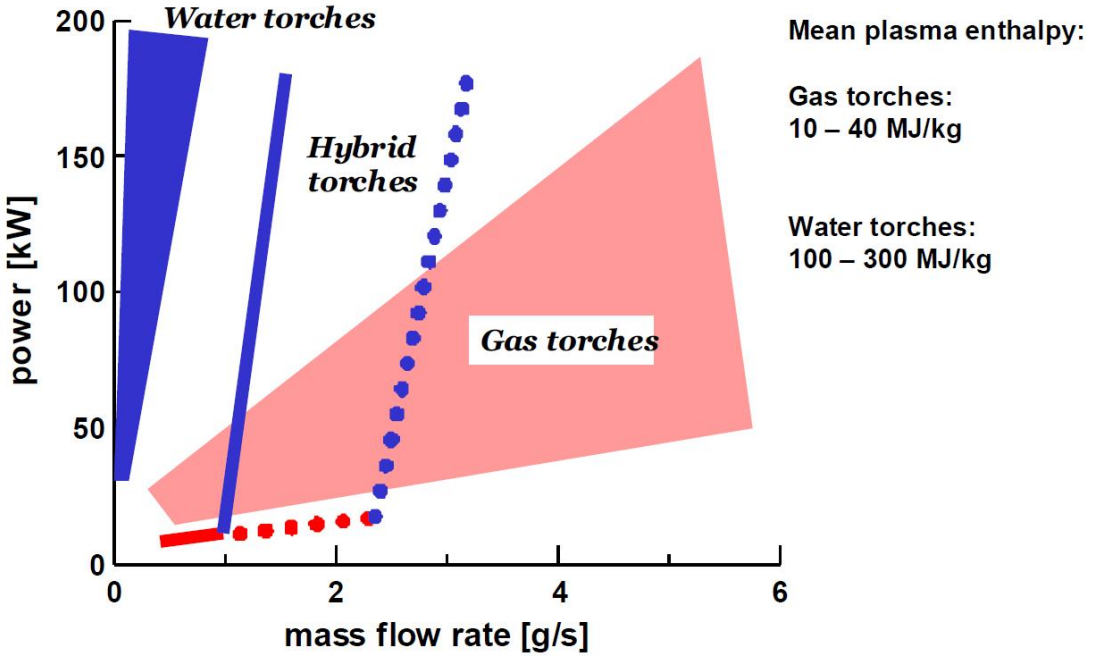

Figure 2.9: Operation regimes of DC arc plasma torches [31]

tion.

The fact that the anode of the hybrid or water plasma torches is outside the plasma torch has advantages as well as disadvantages. The advantage is that the anode processes can be observed directly and clearly. The disadvantage is that these plasma torches are much bigger and heavier than gas plasma torches. As the active surface of the slowly rotating anode is parallel to the plasma jet axis, the conditions in the anode area of the used hybrid plasma torches are similar to the conditions in the anode area of gas plasma torches.

2.3 Thermal plasma

The hybrid water-gas plasma torch in the IPP CAS creates a flow of plasma that can be classified as a thermal plasma. The thermal plasma is by definition in or close to the Local Thermodynamic Equilibrium (LTE). First, we assume that

1) the species that form the plasma have a Maxwellian distribution of speeds.

Then, one of the basic requirements for thermal plasma is that

2) the electron temperature T_e approaches the heavy particle temperature T_h.

Heavy particles in the case of the hybrid plasma torch are various cations, anions, and neutrals made up of elements of argon (or another inert gas that is used), hydrogen, and oxygen [35]. Average plasma temperature values in various positions of the hybrid plasma jet can be found, for example, in [36]. High-mobility electrons pick up energy from the electric field E of the electric arc and partially transfer it to the heavy particles through elastic collisions.

The second requirement ($T_\mathrm{e} \to T_\mathrm{h}$) is called kinetic equilibrium because we assume that the kinetic energy exchanges by elastic collisions are equal to the energy gained by electrons from the electric field. We neglect inelastic collisions because elastic collisions dominate in a plasma. Then we can write the equation for $T_\mathrm{e} - T_\mathrm{h}$ [12]:

$$T_\mathrm{e} - T_\mathrm{h} = \frac{1}{T_\mathrm{e}} \left(\frac{\pi m_\mathrm{h} e^2 E^2}{24 m_\mathrm{e} k^2} \right) l_\mathrm{e}^2, \tag{2.1}$$

where m_e, m_h, l_e, e, and k are the mass of the electrons, the mass of the heavy particles, the mean free path of the electrons, the elementary charge, and the Boltzmann constant, respectively.

It is easy to derive this important equation for stationary heavy particles (with $T_h = 0$ K), but it seems that in the available literature, there is always only a part of this derivation. Let us, therefore, do it completely here:

The positions and masses of the electron and a heavy particle in the laboratory frame are denoted by $\boldsymbol{r_\mathrm{e}}$, $\boldsymbol{r_\mathrm{h}}$, and m_e, m_h. Their relative position is denoted by $\boldsymbol{r_{\mathrm{e,h}}} = \boldsymbol{r_\mathrm{e}} - \boldsymbol{r_\mathrm{h}}$ (Fig. 2.10(a)). If $\boldsymbol{R}$ is the position of the center of mass, T is the kinetic energy of the system electron + heavy particle, and dots above the vectors (denoted by bold font) denote a time derivative, we have the following four equations:

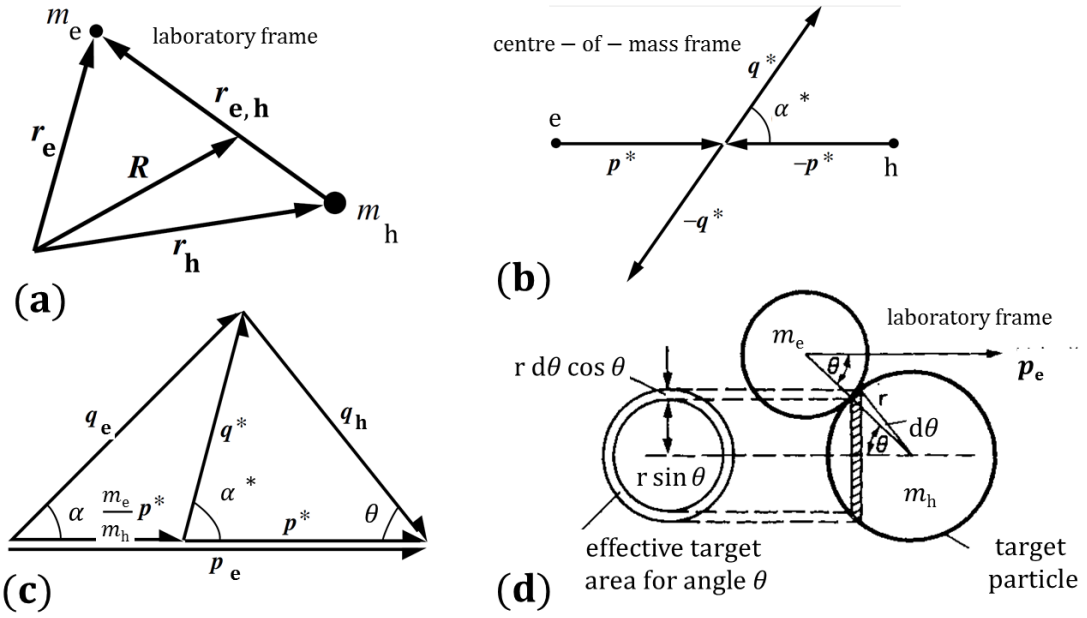

Figure 2.10: ***(a)*** *Position vectors of an electron and a heavy particle in the laboratory frame.* ***(b)*** *Momenta of an electron and a heavy particle before and after a collision in the center-of-mass frame.* ***(c)*** *Vector diagram showing the dependence between the momenta in the center-of-mass frame and laboratory frame. [37]* ***(d)*** *Picture showing two colliding spheres representing an electron and a heavy particle [38]*

$$\boldsymbol{R} = \frac{m_\mathrm{e}\boldsymbol{r_\mathrm{e}} + m_\mathrm{h}\boldsymbol{r_\mathrm{h}}}{m_\mathrm{e} + m_\mathrm{h}} \tag{2.2}$$

$$\boldsymbol{r_e} = \boldsymbol{R} + \frac{m_\mathrm{h}}{m_\mathrm{e}+m_\mathrm{h}}\boldsymbol{r_{e,h}} \tag{2.3}$$

$$\boldsymbol{r_h} = \boldsymbol{R} - \frac{m_\mathrm{e}}{m_\mathrm{e}+m_\mathrm{h}}\boldsymbol{r_{e,h}} \tag{2.4}$$

$$T = \frac{1}{2}m_\mathrm{e}\dot{\boldsymbol{r_e}}^2 + \frac{1}{2}m_\mathrm{h}\dot{\boldsymbol{r_h}}^2 = ... \tag{2.5}$$

$$... = \frac{1}{2}(m_\mathrm{e}+m_\mathrm{h})\dot{\boldsymbol{R}}^2 + \frac{1}{2}\left(\frac{m_\mathrm{e}m_\mathrm{h}}{m_\mathrm{e}+m_\mathrm{h}}\right)\dot{\boldsymbol{r_{e,h}}}^2. \tag{2.6}$$

Now, let's consider the center-of-mass frame, where the center of mass is at rest at the origin ($\boldsymbol{R} = \boldsymbol{0}$), and denote quantities in this frame by an asterisk. Then we have:

$$\boldsymbol{r_e}^* = \frac{m_\mathrm{h}}{m_\mathrm{e}+m_\mathrm{h}}\boldsymbol{r_{e,h}}; \qquad \boldsymbol{r_h}^* = -\frac{m_\mathrm{e}}{m_\mathrm{e}+m_\mathrm{h}}\boldsymbol{r_{e,h}} \tag{2.7}$$

$$\boldsymbol{r_e} = \boldsymbol{R} + \boldsymbol{r_e}^*; \qquad \boldsymbol{r_h} = \boldsymbol{R} + \boldsymbol{r_h}^* \tag{2.8}$$

$$m_e\dot{\boldsymbol{r_e}} = \boldsymbol{p_e} = m_\mathrm{e}\dot{\boldsymbol{r_e}}^* + m_\mathrm{e}\dot{\boldsymbol{R}} = \boldsymbol{p}^* + m_\mathrm{e}\dot{\boldsymbol{R}} \tag{2.9}$$

$$m_\mathrm{h}\dot{\boldsymbol{r_h}} = \boldsymbol{p_h} = m_\mathrm{h}\dot{\boldsymbol{r_h}}^* + m_\mathrm{h}\dot{\boldsymbol{R}} = -\boldsymbol{p}^* + m_\mathrm{h}\dot{\boldsymbol{R}} \tag{2.10}$$

Because of the conservation of angular momentum (in this case also conservation of linear momentum), the electron and a heavy particle in the center-of-mass frame must approach each other with equal and opposite momenta, $\boldsymbol{p}^*$ and $-\boldsymbol{p}^*$, and recede after the collision again with equal and opposite momenta, $\boldsymbol{q}^*$ and $-\boldsymbol{q}^*$ (Fig. 2.10(b)).

Because of the conservation of energy (in this case also conservation of kinetic energy) and the equations (2.6), (2.7) and (2.9), we have:

$$T^* = \frac{1}{2}\left(\frac{m_\mathrm{e}m_\mathrm{h}}{m_\mathrm{e}+m_\mathrm{h}}\right)\dot{\boldsymbol{r_{e,h}}}^2 = \frac{1}{2}\left(\frac{m_\mathrm{e}+m_\mathrm{h}}{m_\mathrm{e}m_\mathrm{h}}\right)\boldsymbol{p}^{*2} = \frac{1}{2}\left(\frac{m_\mathrm{e}+m_\mathrm{h}}{m_\mathrm{e}m_\mathrm{h}}\right)\boldsymbol{q}^{*2}; \tag{2.11}$$

and therefore:

$$|\boldsymbol{p}^*| = |\boldsymbol{q}^*|\,. \tag{2.12}$$

For the momenta $\boldsymbol{q_e}$, $\boldsymbol{q_h}$ in the laboratory frame after the collision, we can use the same procedure we used for $\boldsymbol{p_e}$, $\boldsymbol{p_h}$. Therefore:

$$\boldsymbol{q_e} = \boldsymbol{q}^* + m_\mathrm{e}\dot{\boldsymbol{R}}; \qquad \boldsymbol{q_h} = -\boldsymbol{q}^* + m_\mathrm{h}\dot{\boldsymbol{R}} \tag{2.13}$$

Now, for simplicity, assume that the heavy particles are at rest (or nearly so) in the laboratory frame, so that $\boldsymbol{p_h} = \boldsymbol{0}$. Then we have from (2.9) and (2.10):

$$\boldsymbol{p_e} = \boldsymbol{p}^* + \frac{m_\mathrm{e}}{m_\mathrm{h}}\boldsymbol{p}^* \tag{2.14}$$

and from (2.13) and (2.10):

$$\boldsymbol{q_e} = \boldsymbol{q}^* + \frac{m_\mathrm{e}}{m_\mathrm{h}}\boldsymbol{p}^*; \tag{2.15}$$

$$\boldsymbol{q_h} = -\boldsymbol{q}^* + \boldsymbol{p}^*. \tag{2.16}$$

Therefore $\boldsymbol{p_e} = \boldsymbol{q_e} + \boldsymbol{q_h}$, and we can draw the vector diagram in Fig. 2.10(c), from which we have:

$$|\boldsymbol{q_h}| = 2\,|\boldsymbol{p}^*| \sin\left(\frac{\alpha^*}{2}\right); \tag{2.17}$$

$$\theta = \frac{1}{2}(\pi - \alpha^*). \tag{2.18}$$

Therefore, in the laboratory frame the kinetic energy transferred from the electron to the heavy particle is:

$$\frac{\boldsymbol{q_h}^2}{2m_\mathrm{h}} = \frac{2\boldsymbol{p}^{*2}}{m_\mathrm{h}} \sin^2\left(\frac{\alpha^*}{2}\right), \tag{2.19}$$

and the fraction of the kinetic energy transferred from the electron to the heavy particle is:

$$\frac{\frac{\boldsymbol{q_h}^2}{2m_\mathrm{h}}}{\frac{\boldsymbol{p_e}^2}{2m_\mathrm{e}}} = \frac{\frac{2\boldsymbol{p}^{*2}}{m_\mathrm{h}} \sin^2\left(\frac{\alpha^*}{2}\right)}{\frac{\boldsymbol{p}^{*2}}{2m_\mathrm{e}} \frac{(m_\mathrm{e}+m_\mathrm{h})^2}{{m_h}^2}} = \frac{4m_\mathrm{e}m_\mathrm{h}}{(m_\mathrm{e}+m_\mathrm{h})^2} \sin^2\left(\frac{\alpha^*}{2}\right). \tag{2.20}$$

From (2.18), it follows that

$$\sin^2\left(\frac{\alpha^*}{2}\right) = \sin^2\left(\frac{\pi - 2\theta}{2}\right) = \left(\sin\frac{\pi}{2}\cos\theta - \cos\frac{\pi}{2}\sin\theta\right)^2 = \cos^2\theta. \tag{2.21}$$

Therefore the fraction of the electron's kinetic energy transferred to the heavy particle, during an elastic collision, is:

$$\frac{\frac{\boldsymbol{q_h}^2}{2m_h}}{\frac{\boldsymbol{p_e}^2}{2m_\mathrm{e}}} = \frac{4m_\mathrm{e}m_\mathrm{h}}{(m_\mathrm{e}+m_\mathrm{h})^2} \cos^2\theta. \tag{2.22}$$

All values of θ are equally probable, and the probability of the collision at an angle between θ and $\theta + d\theta$ is proportional to the area of the ring surface defined by these angles and projected normal to the initial electron's momentum $\boldsymbol{p_e}$. According to Fig. 2.10(d), this probability is

$$\frac{dS}{S} = \frac{2\pi r \sin\theta r d\theta \cos\theta}{\pi r^2} = \sin(2\theta)d\theta, \tag{2.23}$$

where S is the total two-particle collisional cross section. Therefore, the average

fraction of the electron's kinetic energy transferred to the heavy particle in all collisions is

$$\frac{4m_{\mathrm{e}}m_{\mathrm{h}}}{\left(m_{\mathrm{e}}+m_{\mathrm{h}}\right)^2}\int_0^{\frac{+\pi}{2}}\cos^2\theta\sin(2\theta)d\theta=\frac{2m_{\mathrm{e}}m_{\mathrm{h}}}{\left(m_{\mathrm{e}}+m_{\mathrm{h}}\right)^2}\rightarrow\frac{2m_{\mathrm{e}}}{m_{\mathrm{h}}}, \tag{2.24}$$

because $m_{\mathrm{e}} \ll m_{\mathrm{h}}$.
Now, according to our assumption that the kinetic energy exchanges by elastic collisions are equal to the energy gained by electrons from the electric field, we have

$$\frac{2m_{\mathrm{e}}}{m_{\mathrm{h}}}\left(\frac{3}{2}kT_{\mathrm{e}}\right)=eEv_{\mathrm{e,d}}\tau_{\mathrm{e}}=eE(\mu_{\mathrm{e}}E)\left(\frac{l_{\mathrm{e}}}{v_{\mathrm{e,t}}}\right)=\frac{e^2E^2{l_{\mathrm{e}}}^2\pi}{8kT_{\mathrm{e}}}, \tag{2.25}$$

where $v_{\mathrm{e,d}}$, τ_{e}, $v_{\mathrm{e,t}}=\sqrt{(8kT_{\mathrm{e}})/(\pi m_{\mathrm{e}})}$, and $\mu_{\mathrm{e}}=(el_{\mathrm{e}})/(m_{\mathrm{e}}v_{\mathrm{e,t}})$ are the drift velocity of the electrons, the mean time between two consecutive collisions of electrons with heavy particles, the mean thermal velocity of the electrons, and the electron mobility respectively.

And, it is precisely the equation (2.1), for $T_{\mathrm{h}} = 0$ K. For high pressure ($p \sim 1/l_{\mathrm{e}}$, [12]), low electric field, and high-temperature plasma, the electron temperature approaches the heavy particle temperature, because the right term in equation (2.1) approaches 0 K, for such conditions.

Other requirements for LTE are:

3) excitation equilibrium:

the excitation processes (excitation by electron impact, excitation by photons, excitation by the impact of atoms or ions) have to be balanced by de-excitation processes (collisions of the second kind during which excitation energy of one particle is transferred to another particle, de-excitation by photoemission, ...);

4) ionization equilibrium:

the ionization processes (ionization by electron impact, ionization by photons, ionization by the impact of atoms or molecules) have to be balanced by recombination processes (three-body recombination, photorecombination, ...);

5) spacial variations (gradients) of the plasma properties are sufficiently small:

the local gradients of plasma properties like temperature, density, etc. must be small enough to enable particles that diffuse from one location of plasma to another to equilibrate.

2.4 Turbulence

Gravitational force in the presence of a heat source can cause a Rayleigh-Benard instability (Fig. 2.11(a)), and flow shear can cause Kelvin-Helmholtz instability (Fig. 2.11(b)). So, the Kelvin-Helmholtz instability can occur where there is a velocity difference across the interface between two fluids, or when

there is a velocity shear in a single continuous fluid. For example, in the water-gas plasma torch, the plasma jet is fast and has a low density, and the ambient pressure is steady and has a high density.

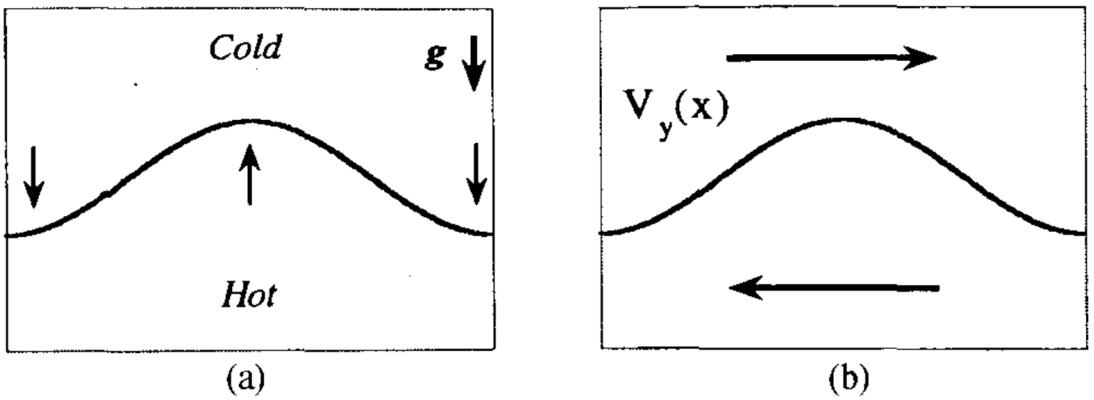

Figure 2.11: (a) Rayleigh-Benard instability in the presence of gravitational acceleration $\boldsymbol{g}$ *and (b) Kelvin-Helmholtz instability in the presence of sheared flow [39]*

Formation of turbulent vortices by Kelvin-Helmholtz instability, on the edge of a free jet, is visualized in Fig. 2.12.

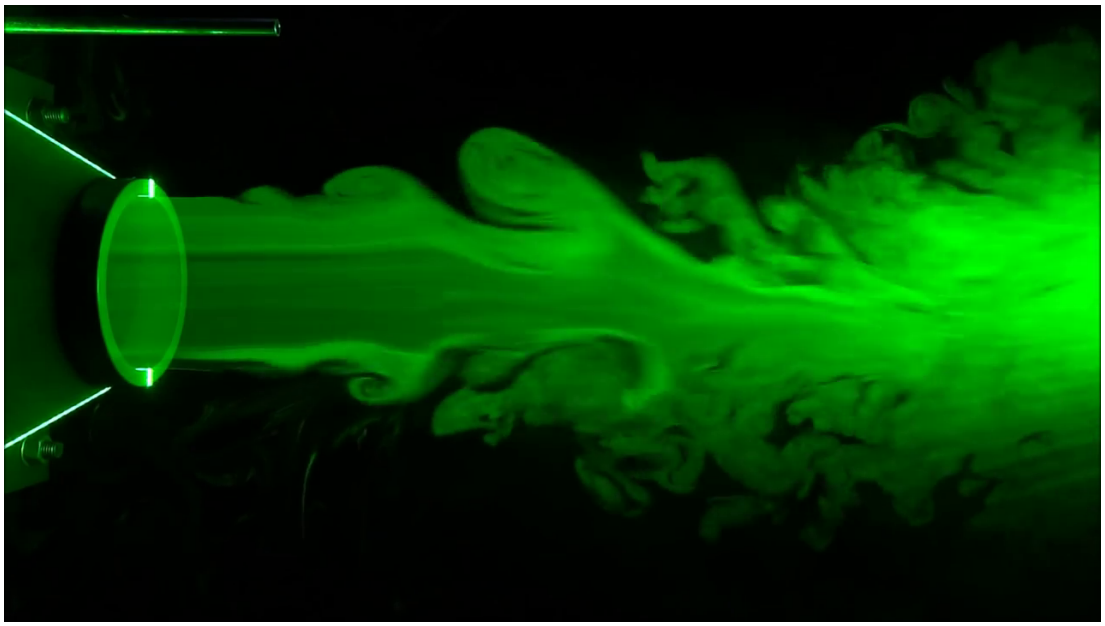

Figure 2.12: The image showing vortex formation in free jet caused by Kelvin-Helmholtz instability. The corresponding video [40] can be seen in the Supplement to this thesis (VIDEO 1)

To predict the transition from laminar to turbulent flow of a fluid, typically, the Reynolds number R_e is used. It can be evaluated from the following equation:

$$R_\mathrm{e} = \frac{UL}{\nu}, \tag{2.26}$$

where U is the free-stream velocity, L is the characteristic linear dimension, and ν is the kinematic viscosity of the fluid [41]. Laminar flow occurs at low Reynolds numbers, and turbulent flow occurs at high Reynolds numbers. The value of the critical Reynolds number for transition from laminar to turbulent flow depends on the character (free jet, non-free jet, etc.) of fluid or the symmetry and geometry of the flow too.

2.5 Supersonic flow

When the speed of the plasma flow is higher than the speed of the sound inside the plasma, the flow is supersonic. The ratio of these two speeds is termed the Mach number, and in the case of the supersonic flow it is greater than unity. In the supersonic plasma jet, there are typical expansion and compression zones separated by shock waves.

In the case that the pressure at the exit nozzle is higher than the ambient pressure, the supersonic plasma jet is underexpanded, and the first zone immediately behind the exit nozzle is the compression zone that has rather a conical shape. In the downstream direction from the exit nozzle, the compression zone is followed by an expansion zone that is followed by another compression zone and so on. The expansion zones are areas where the plasma is expanding. Therefore, the plasma temperature, static plasma pressure, plasma density, and brightness inside the expansion zones are noticeably lower than those in the bright compression zones (Fig. 2.13).

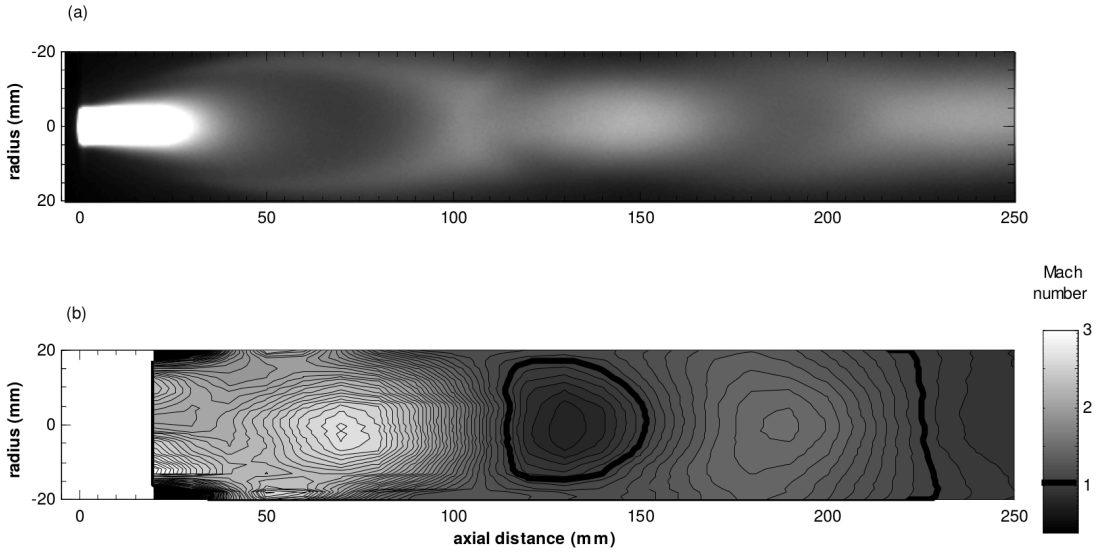

Figure 2.13: (a) Total light emission of the supersonic underexpanded jet created by a Sulzer Metco F4-VB gun with argon plasma and a conical nozzle. (b) The corresponding Mach number iso-contours. p = 0.2 kPa, I = 400 A, 40 slm of Ar [42]

2.6 Schlieren photography

The schlieren technique is a non-invasive technique to visualize density-discontinuities in fluids. It is based on the deflection of a collimated light beam crossing refractive index gradients in a transparent medium. Its basic principle is shown in Fig. 2.14, where L is a light source of homogeneous brightness, O is an objective lens, which should be spherical and with achromatic correction, and L' is the image of L. The schlieren edge K (for example a knife-edge) is located at the position of L', and L' is partially covered by K. a is the distance between the optical axis of the setup and the sharp edge of K, and a' is the distance between the optical axis and a deflected light-beam on the schlieren edge. S is a schliere or density non-uniformity, which causes the deflection of the light-beam.

The name "schliere" comes from August Toepler (1836-1912), who has named the technique after optical inhomogeneities in glass, which were known in German as "Schlieren". Light-beams from L are deflected by S, and they can be refracted either in the direction of the schlieren edge or away from it. The light beams bend toward the region of higher refractive index (for gases it also means toward the region of higher density). The second small lens in Fig. 2.14 (behind L') is an optic that displays a sharp image of S on a screen F.

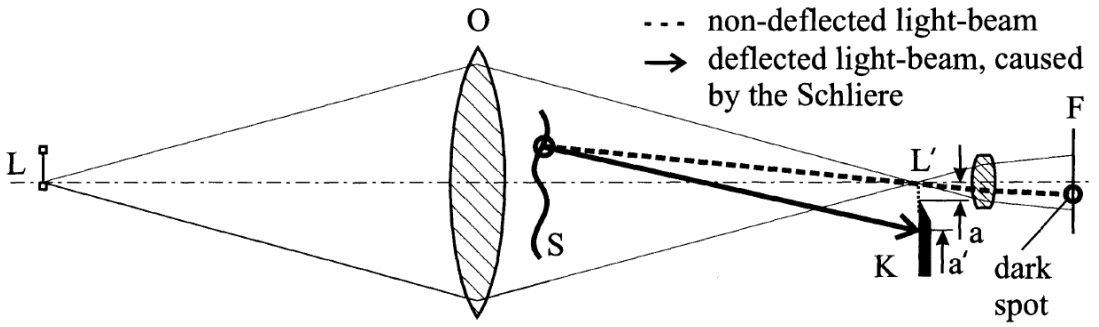

Figure 2.14: Toepler's single-field-lens schlieren arrangement [43]

In the absence of S, F is uniformly illuminated. With density non-uniformities S, the closer the edge of K is to the optical axis, the more light will be covered by K, and the darker is the undisturbed image on F. Therefore, the brightness of the image on F depends on the distance a. When refraction on S is in the direction of K, the spot of the image on F, which corresponds to S, will be darker in contrast to the spot of the image on F, which corresponds to uniform density in the measurement volume.

Conversely, when refraction on S is away from K, the spot on F corresponding to S will be brighter in contrast to the spot on F, representing uniform density in the measurement volume. The typical images on F, with a candle in the position of S look like those in Fig. 2.15 and Fig. 2.16. The schlieren method translates phase difference into amplitude, and it can also record shock-waves (Fig. 2.15, schlieren photo of a bullet).

In Fig. 2.14, there is one optical component - one convex lens. The set up with only one optical component (either convex lens or concave mirror) can only

Figure 2.15: Schlieren photo of a bullet and a candle flame [44]

Figure 2.16: Schlieren image of a candle flame. The rich turbulent structure in the left part arose from the breath (from the right side) interacting with the flame. The corresponding video [45] can be seen in the Supplement to this thesis (VIDEO 2)

be applied if the measurement volume (containing S) is close to that component. When using two optical components (two convex lenses or two concave mirrors), the measurement volume can be placed at any axial position of the parallel light beam (between the two optical components). In general, there is no difference when using either lenses or mirrors. However, it is easier and less expensive to obtain mirrors of high quality as opposed to merely adequate lenses for applications with large measurement volumes, to avoid deflection mistakes or schlieren from the lens glass.

The astigmatic errors and coma [44] which appear when using one concave mirror are compensated if we use two concave mirrors with the same focal length f, the equal angles 2θ between incoming as well as outcoming light (in relation to the measured volume) and when the light source is on the opposite side of the measurement volume from the schlieren edge. Such as arrangement, shown in Fig. 2.17, is called a Z-type schlieren arrangement.

As compared to a set-up with two convex lenses, it is a good compromise between high flexibility and compactness of setup. The advantage of the mirrors in place of lenses is also in a larger field-of-view (for a given cost). The distance between the two mirrors, in Fig. 2.17, should be at least $2f$.

The light beam deviated at S with an angle of ϵ to the optical axis (Fig. 2.17) causes a deviation a' at the schlieren edge (Fig. 2.14) as follows: $a' = \epsilon f$.

The *light source* has to have homogeneous brightness and a finite extent. It does not have to be coherent. When a coherent light source is used, both bright- and dark-field images are susceptible to spurious imaging [44]. In general, the smaller the wavelength of the light source, the higher the sensitivity of the schlieren set-up. Generally, arc-lights (for example discharge lamps) are adequate

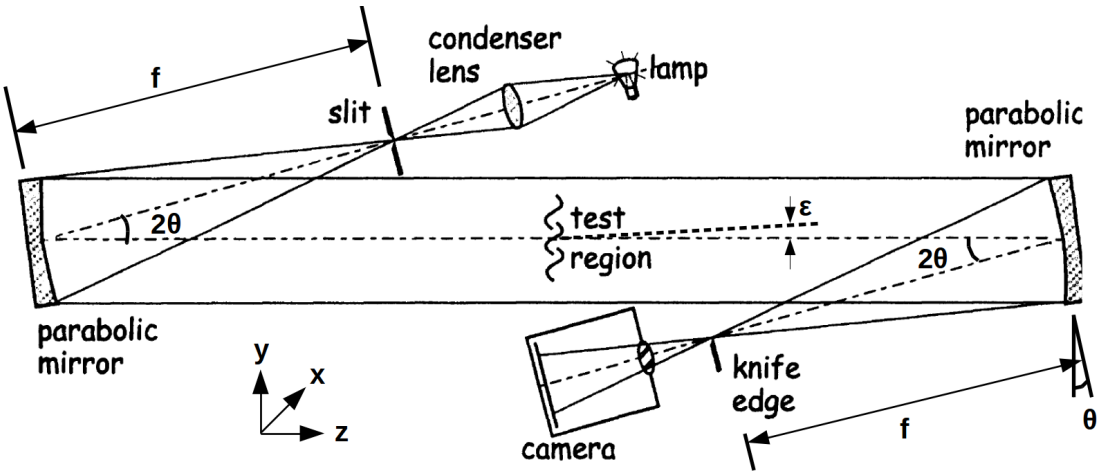

Figure 2.17: Z-type schlieren arrangement [44] (modified)

light sources. Much less optical sensitivity is needed to see refractions in solids or liquids than in air. If we want to observe very weak disturbances, infrared light will detect them better than visible light.

The light source at the front focus of the first schlieren lens should have sharp boundaries (at least one sharply limited edge). Often a condenser lens together with a slit is used to ensure this (Fig. 2.17): The condenser lens focuses the light from the light source to the front focus of the first schlieren lens. The slit is located at that front focus and it creates sharp boundaries of the light. A narrow-band color filter at the light source is often used to eliminate a residual chromatic aberration that happens even with achromatic lenses, because the knife-edge cuts off a part of the light spectrum.

The *schlieren edge* has to be located in the focal point of the optical element (mirror or lens). Its exact position is found when the image on screen gets homogeneously darker during the movement of the schlieren edge from a side into the light beam. The schlieren edge should be a round aperture (small opening) for a circular light source and a knife-edge for a rectangular light source. A round aperture visualizes gradients of all directions within the measurement volume, without distinguishing the direction; however a knife-edge visualizes gradients only in one direction.

For example with a horizontal knife-edge (Fig. 2.17, the plane (x,z)), only a vertical refractive index gradient ($\partial n/\partial y$) is detected. When we use a knife-edge, we can observe schlieren images on a bright screen/field or a dark screen/field. In the first case, the focal point of the light source should be just above the knife-edge, and in the second case, the focal point of the light source should be just blocked by the knife-edge.

If we want to observe schlieren with two refractive index gradients, we should use a round aperture, and the two gradients should be oriented in x and y direction for best visibility. This means that in Fig. 2.17, the gradients should be $\partial n/\partial x$ and $\partial n/\partial y$.

A color schlieren system can be created by replacing the schlieren edge with

a transparent color-filter. In such a case, the light source should have a homogeneous spectral distribution in order not to be limited in assigning a specific color to a particular class of gradients.

The plasma is more refractive than other states of matter; therefore, schlieren methods can be used even for low-density plasma.

2.7 Langmuir probe theory

A Langmuir probe is usually a tungsten rod or wire 0.1 - 1 mm in diameter. It must be a high-temperature material. "The rod is threaded into a thin ceramic tube, usually alumina, to insulate it from the plasma except for a short length of exposed tip, about 2-10 mm long" [46].

A general form of a Langmuir probe current versus bias voltage characteristic looks like that in Fig. 2.18(a), where Φ_{plasma} is the plasma electric potential with respect to the probe ground and Φ_{f} is the probe's potential Φ (bias voltage) with respect to the probe ground when the probe current $I = 0$ A. Φ_{f} is termed the floating potential.

When Φ with respect to Φ_{plasma} is very negative, the electric field around the probe will reduce the electron current to zero and the current I_{si} collected by the probe is then entirely due to positive ions. I_{si} is termed the ion-saturation current. When Φ is increased into positive values, the number of electrons which are able to overcome the repelling electric field around the probe increases exponentially, and therefore the probe current I also increases exponentially up to the limit that is termed the electron-saturation current I_{se}. Any further increase in Φ will only add energy to the electrons and not increase the probe current. The derivative of bias voltage Φ with respect to probe current I is termed the differential resistance $R_{\mathrm{differential}}$, also known as a dynamic resistance. $R_{\mathrm{differential}}$ has the meaning of a transition resistance between the probe and plasma.

A probe immersed in a plasma strongly perturbs the electric potential over a small region, called the sheath. In the distance from the probe, the sheath has a radius of several Debye lengths. The Debye length can be evaluated by the following formula:

$$\lambda_{\mathrm{D}} \approx \sqrt{\frac{\epsilon_0 T_{\mathrm{e}}}{n_{\mathrm{es}} e^2}}, \tag{2.27}$$

where ϵ_0 is the permittivity of free space, T_{e} is the electron temperature in the unperturbed plasma, n_{es} is the electron density at the sheath edge, and e is the proton charge.

The perturbation of the electric potential by a probe is depicted in Fig. 2.18(b). The unperturbed plasma is designated by $x = \infty$. The probe surface is designated by $x = x_{\mathrm{p}}$, and the sheath thickness is $x_{\mathrm{s}} - x_{\mathrm{p}}$. In Fig. 2.18(b), the electric potential of the unperturbed plasma (at $x = \infty$) is defined to be zero. Φ_{p} is the probe potential, and Φ_{s} is the electric potential at the sheath edge, both

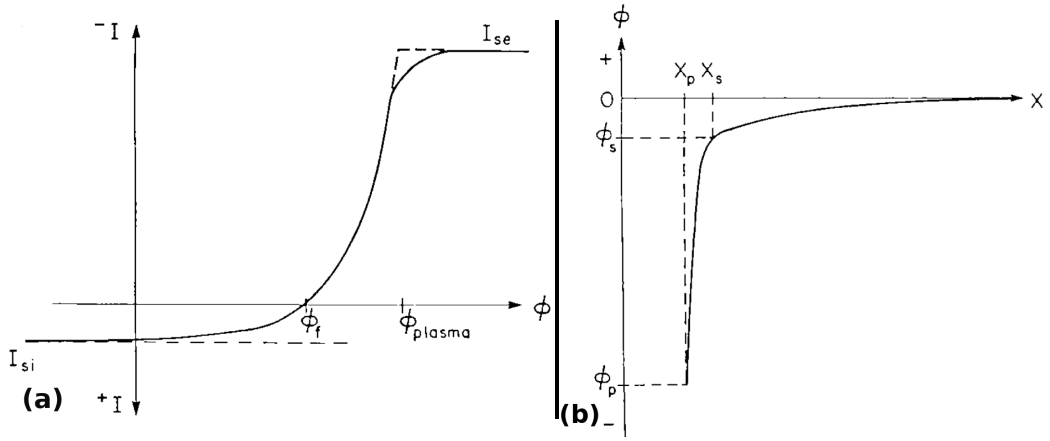

Figure 2.18: ***(a)*** *Standard Langmuir probe current versus bias voltage characteristic. Φ is the probe's potential (bias voltage) with respect to the probe ground, and I is the probe current.* ***(b)*** *Illustration of electric potential perturbation caused by a probe immersed in plasma [47]*

with respect to the zero potential of the unperturbed plasma.

There is a useful relation between the floating potential Φ_{f} of a Langmuir probe and the plasma potential Φ_{plasma}:

$$\Phi_{\mathrm{f}} = \Phi_{\mathrm{plasma}} - \frac{T_{\mathrm{e}}}{e} \cdot \ln \left| \frac{I_{\mathrm{se}}}{I_{\mathrm{si}}} \right|, \tag{2.28}$$

where T_{e} is the electron temperature of the unperturbed plasma in eV. When we substitute their functional relations for both saturation currents, we obtain the equation that is derived, for example, in [10].

Electric probe measurements in a DC argon welding arc are reported in [48], electric probe measurements in a near-wall region of a wall-stabilized, atmospheric-pressured argon DC arc are reported in [49], and a review of electrostatic probe plasma diagnostics can be found in [50]. The electric probes in plasmas are often used under floating conditions [49,51]. This thesis deals with measurements with electric probes under floating conditions in the water-argon stabilized DC arc.

3. Experimental setup

The experimental setup used for measurements at pressures lower than the atmospheric pressure, with the plasma torch WSP®-HR, is illustrated in Fig. 3.1. For measurements at atmospheric pressure, the low-pressure chamber was absent, and the plasma torch WSP®-H 2011 was instead used.

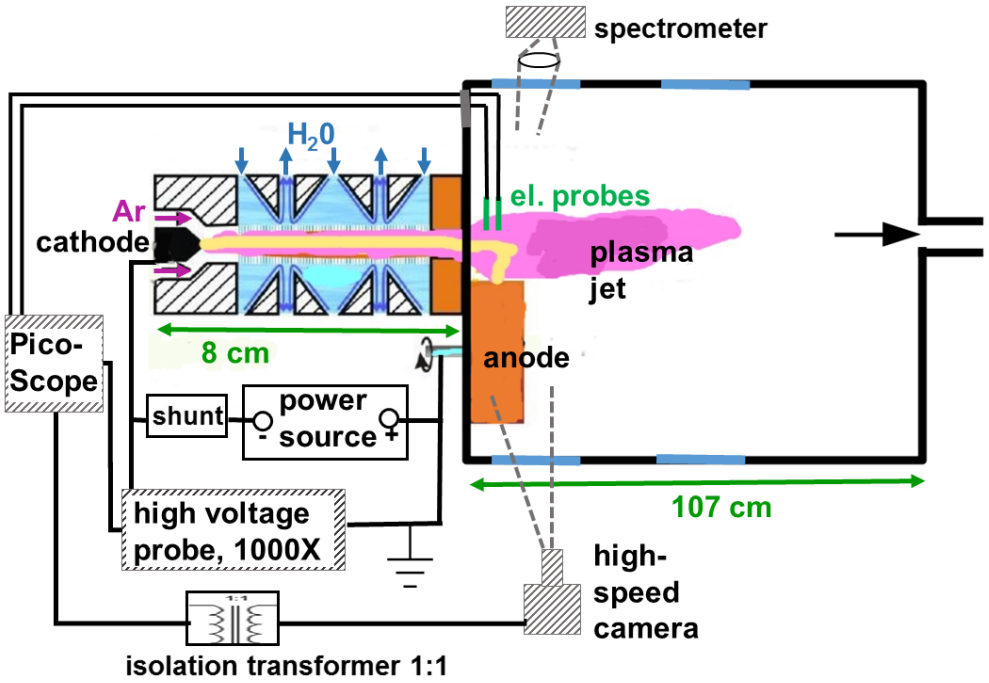

Figure 3.1: Experimental setup for measurements at pressures lower than the atmospheric pressure excluding the Schlieren imaging system and the array of photodiodes

3.1 Plasma torch

The hybrid water-argon plasma torch was used. This is described in Hybrid water-gas DC arc plasma torch section 2.2. In that plasma torch, the stabilizing component between the cathode and anode consists of several consecutive vortex chambers separated by partitions. The water for the stabilization of the arc is pumped inside the torch chamber under pressures of 400-600 kPa through tangential openings placed equidistantly along a circumference at angles of 120°. Typical flow rates of this stabilizing water are in the range of 10-16 l/min. Suction plots are placed between the intake openings, and the water then flows in a closed circuit. Inside the torch chamber, the water is evaporated with the rate in the range of about 6-22 g/min [6]. This very small amount of water consumption, due to evaporation, has not been measured directly up to now. It is challenging to measure such a small amount of evaporated water when there are such high flow rates occurring in the water circuit.

During the anode rotation, its surface moves perpendicularly to the main plasma

flow at the speed of 9.6 ± 0.5 m/s (it is valid for the conventional value of the anode rotational frequency of 28 Hz) in the case of the WSP®-HR plasma torch and at the speed of 27 ± 1 m/s (for the anode rotational frequency of 47 ± 1 Hz) in the case of the WSP®-H 2011 plasma torch. The copper anode and 2 % thoriated tungsten cathode are cooled down by two additional water circuits that are separate from the one used to stabilize the electric arc. In the case of the WSP®-H 2011 plasma torch, all three water circuits are connected through one water container. The water inside all water circuits is the same water that is obtained from tap water by using reverse osmosis and some additional filters.

3.2 Measuring instruments

The instruments used were:

1) A monochromatic high-speed camera, a Photron FASTCAM SA-X2.

This has a maximum frame rate of 1,080,000 fps. We used almost exclusively a frame rate of 300,000 fps with an exposure time of 0.29 μs, and a pixel resolution of 256x80. The frame rate of 1,080,000 fps requires very low pixel resolution, 128x8, which causes, among other things, very great uncertainties in the camera measurements.

2) A Canon 70-300 mm camera lens, together with 1000x, 64x, and 8x gray optical filters.

We used a focal length of 300 mm because the distance between the lens and the observed plasma jet was about 1.5 m.

3) A Canon EOS 450D camera.

This was used for making color images of the visible part of the plasma jet with the exposure time in the range of ms.

4) A low-pressure chamber with a double wall with cooling water.

This grounded chamber had a cylindrical shape with a length of about 107 cm and a diameter of about 95 cm. When it was used, the plasma torch was placed in the middle of its vertical base. The cameras filmed through one of its four ordinary silicate glass vertical windows.

5) Two rotary vane pumps.

6) A CMR 361 ceramic capacitance gauge for measuring the pressure inside the low-pressure chamber.

7) A high voltage probe, a Tektronix P6015 (1000:1, 100 $M\Omega$, 3pF).

This measured voltage with a sampling rate of 80 MHz (at ambient pressure $p =$ 101 kPa) or 20 MHz (at ambient pressure $p <$ 101 kPa).

8) A PC Oscilloscope (PicoScope 4424).

This had four channels, but sometimes we used two PicoScopes together, to have 8 channels.

9) An oscilloscope probe, a T5100 (100MHz/6MHz, 10X:600Vpk, 1X:200Vpk).

This measured the voltage between the electric probes and the anode.

10) AQ Sartorius E 2000 D balance scale.

These were used to measure anode weight loss.

11) A Carl Zeiss system for Schlieren imaging, with a knife-edge and a 500 W mercury lamp.

This system was borrowed from the Institute of Thermomechanics AS CR and is shown in Fig. 3.2. During the schlieren imaging, we placed a 560-600 nm bandpass color optical filter in front of the camera. An additional four mirrors were used to create a quasi periscope because the low-pressure chamber was wider than the space between the two arms of the Schlieren system. In the future, it is planned to build a simple Z-type schlieren arrangement with two parabolic mirrors that are already available in the Plasma Chemical Technology department.

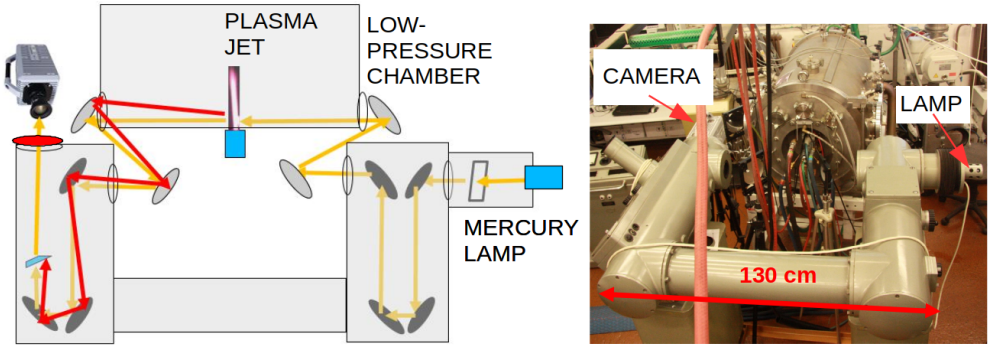

Figure 3.2: The Carl Zeiss system for schlieren imaging on the right, with light paths depicted on the left

12) Movable system of two electric wire probes.

Electric probes together with the corresponding technical components (those that were inside the low-pressure chamber) are depicted in Fig. 3.3. Each probe had a graphite cylindrical pin with corundum electrical isolation. The diameter, as well as the length of the pins, was equal to 1 ± 0.1 mm. When used together, they were separated from each other by 1.7-2.0 mm. These probes moved through the plasma jet along a circular trajectory with a 218 ± 1 mm radius in the direction $\boldsymbol{x} \times \boldsymbol{y}$ or $\boldsymbol{y} \times \boldsymbol{x}$ (Fig. 3.5), that is to say, perpendicularly to the plane (x,y). The radial speed of these probes in the visible part of the plasma jet was about 2.3 ± 0.2 m/s. Their movement was controlled by hand, filmed by the high-speed camera (see VIDEO 3 in the Supplement to this thesis), and monitored by a potentiometer with a rotating contact. The value of 2.2 m/s was calculated from the potentiometer data and verified by processing the high-speed camera video footage.

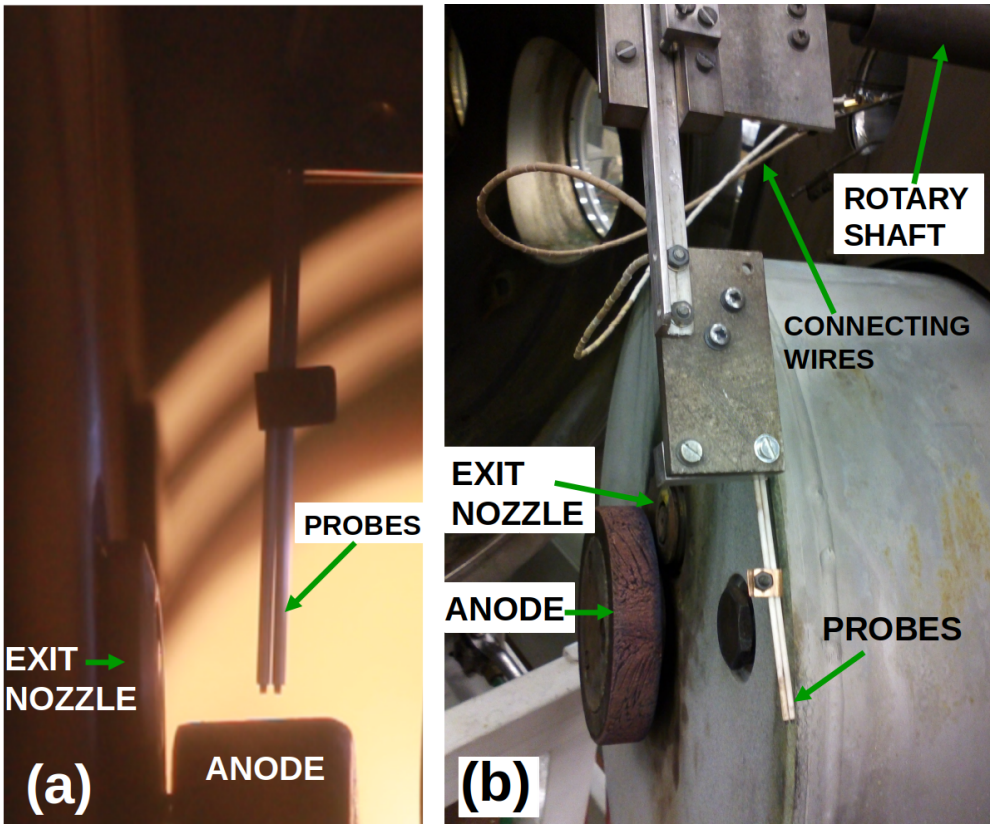

Figure 3.3: Details of the setup used for probe measurements. Only components inside the closed low-pressure chamber are visible. ***(a)*** *Two electric probes in the position where they were inside the visible part of the plasma jet during the operation of the plasma torch.* ***(b)*** *Two electric probes together with other technical components. The door of the low-pressure chamber, where the anode and nozzle were located, is shown here as open*

13) Two DC regulated power supplies, AX-12001 DBL, 0-120 V, 1 A.

These were used in the measurements of the electric probe $I - \Phi$ characteristic.

13) A MATLAB 2016a computer program was used to process the data, and a Photron FASTCAM Viewer Ver.3610 program was used to both create videos and control the high-speed camera from a laptop.

14) An enthalpy probe system by Tekna Plasma Systems Inc.

This was used without a quadrupole mass spectrometer. The inlet diameter of the enthalpy probe used was 1.27 ± 0.05 mm.

15) Isolation transformers.

These were connected in the electric circuits to reduce electrical noise, which represented about 0.2 % of the measured waveforms (typically $\pm$ 0.4 V) at the ambient pressure of $p = 101$ kPa. An isolation transformer 220V/4A was used to electrically isolate the Tekna enthalpy probe system from the power socket.

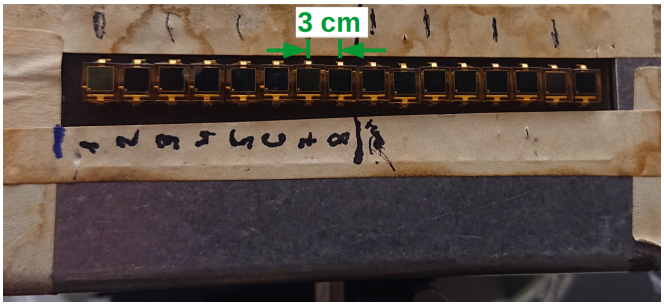

Figure 3.4: The array of photodiodes used to measure the plasma speed above the anode. The photo was taken in 2019

The values of plasma electron temperature T_e were measured with a spectrometer, a Jobin-Yvon Triax 552. The plasma speed above the anode was measured by using the array of 16 photodiodes, from which we used only five photodiodes from the eight photodiodes labeled by the numbers 1-8 in Fig. 3.4.

3.3 Working conditions

The conditions of the experiments set before the plasma torch operation are summarized in Table 3.1. In the three pairs of values in the last three columns, the first value was applied at atmospheric ambient pressure and the second value was applied at low ambient pressures inside a low-pressure chamber. In plasma spraying applications (using the hybrid plasma torch WSP®-H 2011), the arc current generally used is 300-500 A, (which corresponds to the arc voltage 270-320 V), and the typical argon flow rate used is 12-25 slm. Regarding the organic waste gasification, pyrolysis, or hydrocarbon reforming, the arc current generally used is 400 A.

Arc current I [± 3 A]	Argon consumption Ar [± 0.5 slm]	Ambient pressure p [± 0.5 kPa]	Exit gap diameter D [± 0.2 mm]	Anode width [± 0.2 mm]	Anode diameter [± 1 mm]
40 - 600	8 - 32	0.8 -101	6, 5	16, 20	181, 109

Table 3.1: The working conditions of the two hybrid plasma torches used. In the three pairs of values in the last three columns, the first value corresponds to the WSP®-H 2011 and the second value corresponds to the WSP®-HR

The anode can be moved vertically and, except when using the WSP®-HR torch in the low-pressure chamber, also horizontally. The position of the anode determines the properties of the entire plasma jet; and the anode configurations used are summarized in Table 3.2. The first five configurations (C1-C5, together with the inclined configuration $C2_{INC}$) were applied at atmospheric ambient pressure; and the rest of them were applied at low ambient pressures. x_A is the horizontal distance between the anode and the exit nozzle, and y_E is the vertical distance between the upper part of the anode surface and the bottom edge of the exit gap (Fig. 3.5).

The anode surface often has a small inclination of 1-2° because the part of the anode closer to the exit nozzle is usually more eroded than that farther from the exit nozzle. The distance y_E was always measured from the edge of the anode

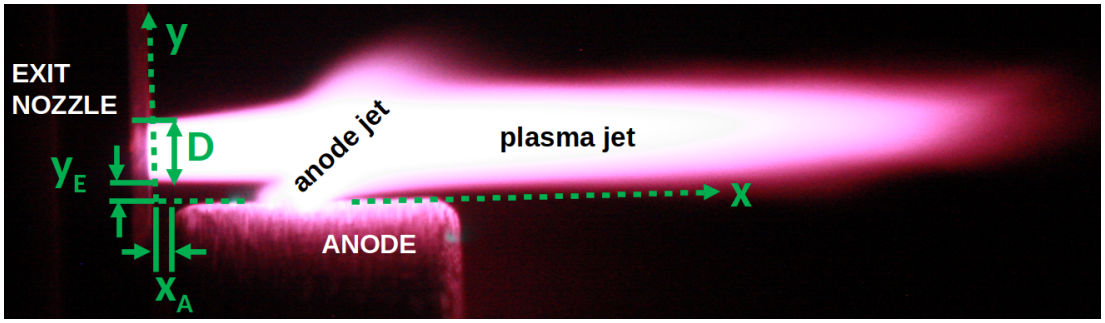

Figure 3.5: Camera image of the anode area in the C5 anode configuration together with the coordinate system used. Gray optical filter 1000x, I = 200 A, p = 80 kPa, 22 slm of Ar

that is closer to the exit nozzle. The difference of x_A in configurations C1-C4 (at atmospheric pressure) was caused by the horizontal movement of the anode with respect to the exit nozzle. However, in configurations C5-C8 (at low ambient pressure) the two values of x_A are only the result of using two different exit nozzles: thick (in C5, C7, C8) and narrow (in C6). Therefore, in all configurations C5-C8 the distance between the anode and the cathode was the same. In plasma spraying applications of the hybrid plasma torch, the C1 configuration is mainly used.

The coordinate system that we used is depicted in Fig. 3.5. In $C2_{INC}$, the anode surface was inclined upward at an angle of 10° to the horizontal position, and the corresponding value of y_E is valid for the center of the anode surface. The arc electric power depends mainly on the arc current value, and it was in the range of 6 - 230 kW.

Anode configuration	C1	C2, $C2_{INC}$	C3	C4	C5	C6	C7	C8
Horizontal distance x_A [± 0.2 mm]	3.8	10.8	3.8	0.9	1.4	3.4	1.4	1.4
Vertical distance y_E [± 0.2 mm]	0.9	1.4	5.2	(-1.3; -0.4)	0.9	0.9	3.3	4.7

Table 3.2: The positions of the anode used

4. Methods

4.1 Determination of attachment movement characteristics

The average speeds of the anode arc attachment, the average restrike periods, the average distances traveled by the constricted anode arc attachment, and the average axial positions of the attachment creation and decay were computed by using the MATLAB script shown in the MATLAB script for attachment movement investigation.

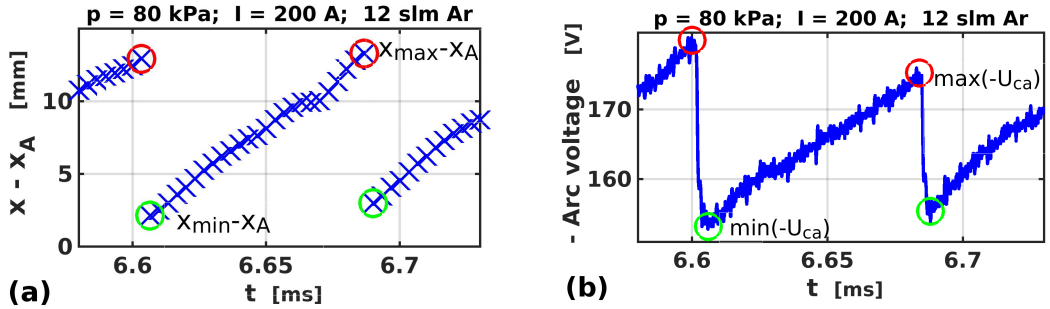

Figure 4.1: ***(a)*** *The time dependence of the axial attachment position on the anode surface in C6, according to the coordinate system in Fig. 3.5.* ***(b)*** *The corresponding negative cathode-anode voltage waveform* $-U_{ca}$

The basic time dependence of the horizontal attachment position projected onto the axial direction during the restrike mode is shown in Fig. 4.1(a). This was used to compute the characteristics of the attachment movement, and the x-component of the attachment speed was computed as follows:

$$v_{\text{attachment,x}} = \frac{(x_{max} - x_A) - (x_{min} - x_A)}{t(x_{max} - x_A) - t(x_{min} - x_A)}. \tag{4.1}$$

Unless otherwise stated, the "attachment speed" recorded in Figures in chapter 6 is an average value of $v_{\text{attachment,x}}$ that was computed from the time interval of 100 ms.

The attachment movement recorded in the camera footage was projected a little onto the camera image plane due to a distance component in the direction of the anode rotation. However, the real distance traveled by the attachment was almost the same as the distance traveled by the attachment seen in the camera footage. To explain further, let's say we have an average restrike period of 50 µs and an average distance of 6 mm traveled by the attachment on the anode surface. Then if the WSP®-H 2011 plasma torch is being used, in reality the attachment would travel during one restrike period no more than 0.2 mm longer distance than that distance seen in the camera footage. The distance increase of 0.2 mm corresponds to a voltage increase of about 0.3 V at the maximum. In the

case of the WSP®-HR plasma torch, the distance would even be ten times less, that is, no longer than 0.02 mm.

The horizontal position x of the attachment (Fig. 3.5), projected onto the axial direction, was defined as the position of its upstream edge and was found in the high-speed camera images as the first pixel in a select line of pixels where its brightness is greater than a specific chosen value. The line of pixels that was selected was as close to the anode surface as possible.

The conversion from pixels to millimeters was obtained by comparing the known length of 2 cm in a representative image with a corresponding number of pixels (around 200). The frame rate of 300,000 fps was used, and the frame rate of 1,080,000 fps (with a far worse pixel resolution) was used only once to confirm that the attachment movement was not, in reality, faster than it seemed to be in the camera footage with 300,000 fps. In other words, the frame rate of 1,080,000 fps was used only to confirm that we were not deceived by the wagon-wheel effect (alternatively, by the stroboscopic effect).

The "restrike period" means an average duration between two consecutive restrikes. In Figures in Chapter 6, this was computed as the average value from the two average values: the first average value was the average of differences of adjacent $t(x_{max} - x_A)$ values; and the second, the average value of differences of adjacent $t(x_{min} - x_A)$ values. Unless otherwise stated, this was computed in time intervals of 100 ms. Sometimes, the restrike period was computed from the arc voltage waveform, which appears to be almost the same as the attachment position time dependence (Fig. 4.1(b)). Arc voltage waveforms were synchronized with the camera footage. A video showing this synchronization is available in the Supplement to this thesis (VIDEO 4). When arc voltage waveforms were used, the restrike period was computed as an average of two averages: an average value of differences of adjacent $t(min(-U_{ca}))$ values and an average value of differences of adjacent $t(max(-U_{ca}))$ values.

The "distance traveled" by the attachment, in Figures in Chapter 6, was computed as the average value of distances traveled by the constricted attachment during individual restrike periods; that is to say, computed as

$$\frac{1}{N}\sum_{n=1}^{N}((x_{max} - x_A)_n - (x_{min} - x_A)_n), \tag{4.2}$$

where N is the number of restrikes in the time interval investigated. This was computed from 100 ms (at $p < 101$ kPa) and 9.5 ms (at $p = 101$ kPa) of the attachment position time dependence.

The average position of the attachment creation and the average postion of the attachment decay were computed as the average of $(x_{min} - x_A)_n, n = 1, .., N$ and $(x_{max} - x_A)_n, n = 1, .., N$, respectively, from time intervals of 100 ms.

4.2 Determination of plasma speed and wave speed

The "plasma speed" in the anode area (that is, above the anode), in Figures in Chapter 6, was computed according to the method reported in [22]. The idea of the method is depicted in Fig. 4.2.

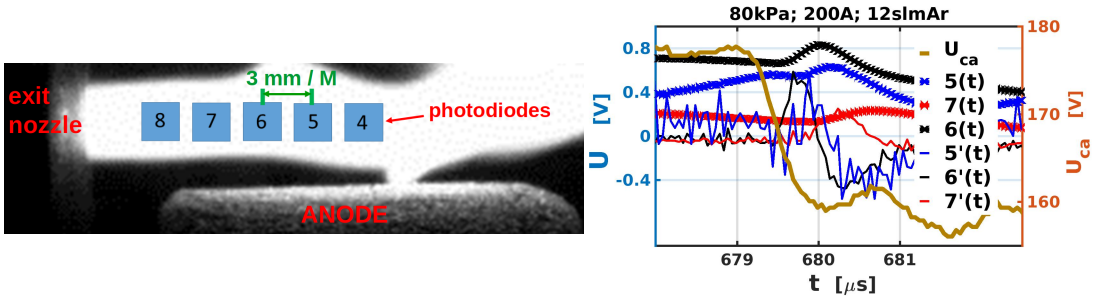

Figure 4.2: ***(left)*** *A 1.6-times magnified image of the plasma jet in the anode area projected onto five photodiodes that are numbered according to Fig. 3.4.* ***(right)*** *The corresponding arc voltage waveform ("U_{ca}") that is synchronized with the electric signals U from the photodiodes 5,6, and 7; together with the first time derivatives of these three signals ("5'(t)", "6'(t)", "7'(t)"). Anode configuration C6*

By using one convex lens, the image of the plasma jet was magnified M times and projected onto the array of photodiodes that were fixed in a stable position. The radiation emitted from the plasma oscillated coherently; therefore, the photodiodes' electric signals fluctuated. These oscillations were probably caused by a formation of turbulent vortices. In the position where a restrike suddenly happened, these fluctuations were disrupted and the perturbation propagated through the plasma in all directions at speed $v_{\text{perturbation}}$ with respect to the plasma. The disruption of the fluctuations in the photodiodes' signals can be seen in the Supplement to this thesis (VIDEO 5). The plasma moved at average speed $\bar{v}_{\text{plasma}}$ with respect to the photodiodes. The total speed of the perturbation with respect to the photodiodes, detected by individual photodiodes at different times, depends on the direction of its propagation; that is, we have its upstream speed v_{upstream} or its downstream speed $v_{\text{downstream}}$. The upstream and downstream speed of the perturbation, with respect to the photodiodes, can be determined from the delays of electric signals of photodiodes that are in various positions. For example, with the numbering of the photodiodes shown in Fig. 4.2, we can calculate the average plasma speed above the anode as follows:

$$v_{\text{upstream}} = v_{\text{perturbation}} - \bar{v}_{\text{plasma}} = \frac{2.5 \text{ mm}/M}{t_{max[7'(t)]} - t_{max[6'(t)}}, \tag{4.3}$$

$$v_{\text{downstream}} = v_{\text{perturbation}} + \bar{v}_{\text{plasma}} = \frac{2.5 \text{ mm}/M}{t_{max[5'(t)]} - t_{max[6'(t)}}, \tag{4.4}$$

$$\bar{v}_{\text{plasma}} = \frac{v_{\text{downstream}} - v_{\text{upstream}}}{2}, \tag{4.5}$$

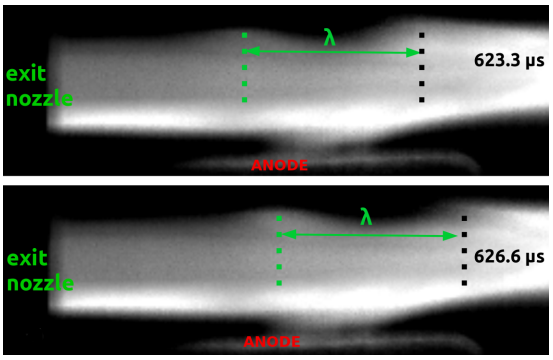

Figure 4.3: Two consecutive camera images with a hydrodynamic wave propagating in the plasma jet to the right (downstream). Because of the optical filter used, the visible radiation has a wavelength of (810 ± 12) nm. Exposure time 0.29 µs (adapted from [52])

where, for example, $5'(t)$ is the time derivative of the signal from the photodiode number 5, $t_{max[5'(t)]}$ is the time corresponding to the local maximum of the graph $5'(t)$; and 2.5 mm/M is the distance between the middle of one real photodiode (that is, not its image) and the edge of an adjacent real photodiode.

In [22], the time derivatives of signals from the photodiodes were not calculated. Instead, times when signals from the photodiodes suddenly rose up or fell down were found. At those times, the time derivatives of the signals reached their maxima.

To decrease the uncertainty of this method, a high enough magnification M of the plasma jet is required. For higher magnifications, the dimension of photodiodes in the image is smaller and the uncertainty in the detected distance propagated by perturbations is lower. In the case of higher magnifications M, we can exchange the distance 2.5 mm, in equations (4.3) and (4.4), with the distance between the middle of one real photodiode and the edge of a farther real photodiode (that is, not the adjacent one). The perturbations in the plasma jet are easily detectable typically within the real distance of 2 mm from the position of their creation, that is, from the restrike position.

The speed of the hydrodynamic waves, shown in Fig. 5.5, was calculated simply as the ratio of the distance traveled and the corresponding time (10/3 µs) between two following camera images. The position of the waves was defined as the horizontal position of their crest and their wavelength was calculated from these images as the distance between two consecutive crests (Fig. 4.3). The average values of the hydrodynamic wave speed and wavelength were obtained from only eight different waves.

4.3 Determination of proportion of all attachment's dwellings

The dwellings (the intermittent and sudden decreases in speed) of the constricted anode arc attachment within the length l on the anode surface for the time interval t were found in the time dependence of the axial attachment position and/or in the arc voltage waveform (Fig. 4.4). To find all dwellings, we

linearly interpolated the time dependence of the attachment position with the time step of 13 ns, which is equal to the time resolution of the measured arc voltage waveforms. The MATLAB script that we used can be downloaded here: MATLAB script for finding attachment's dwellings.

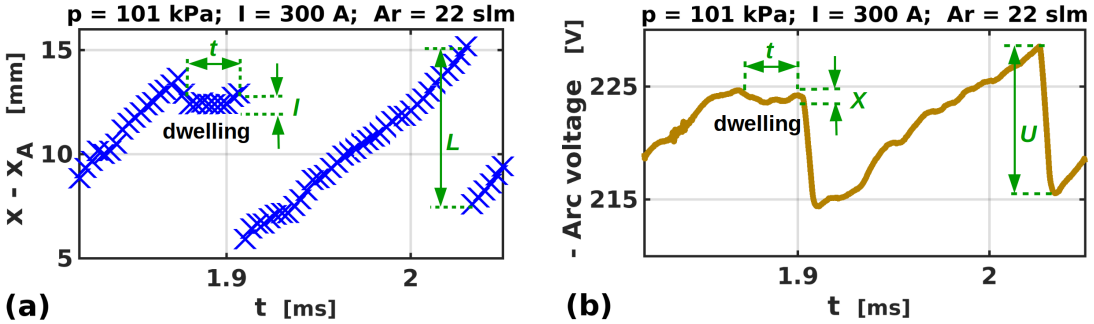

Figure 4.4: ***(a)*** *The time dependence of the axial attachment position on the anode and* ***(b)*** *the corresponding negative arc voltage waveform after removing frequencies higher than 1 MHz and smoothing with a span of about 5 µs (399 values) of the moving average. Time t is the duration of one attachment's dwelling, l and X represent the maximum extent of the position and voltage value during the dwelling (adopted from [53])*

In arc voltage waveforms at $p = 101$ kPa, there were numerous interfering outer electric signals; therefore, frequencies higher than 1 MHz were removed by using a Fourier transform. The voltage data were then further smoothed with a span of about 5 µs (399 values) of the moving average. Fig. 4.4(b) shows only the smoothed data with frequencies lower or equal to 1 MHz. The voltage range X in Fig. 4.4(b) is equivalent to the length l in Fig. 4.4(a). The physical meaning of the length l is depicted in Fig. 4.5(a),(c).

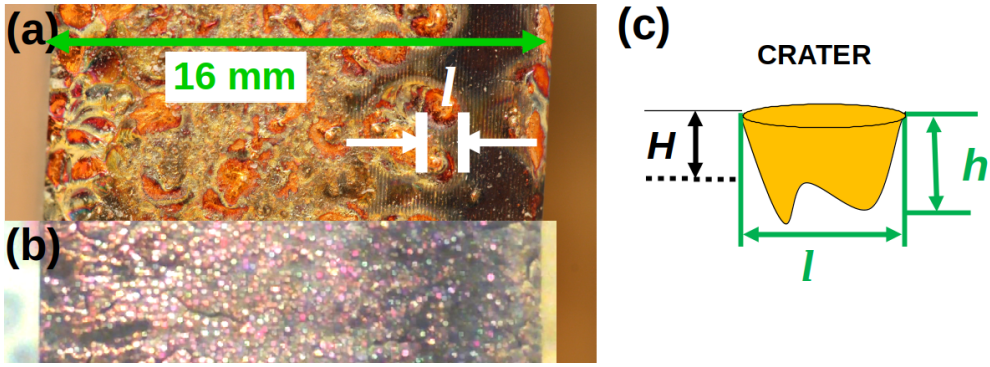

Figure 4.5: ***(a)*** *Detail of a new anode surface after 23 min of a plasma torch operation with a constricted attachment. The length l of the chosen marked big crater is about 1.3 mm, which is almost the width of the constricted attachment near the anode surface.* ***(b)*** *Detail of a worn anode surface after about 50 hours of a plasma torch operation, mostly with a constricted anode arc attachment.* ***(c)*** *Schematic picture of a crater on the anode surface with length l, real depth h, and a reference depth H (adopted from [53])*

We can say that we found all attachment's dwellings during which craters with a fixed length l were created.

The inequality $t > T =$ constant represents the total time to make the crater. This is because the heat transfer from the arc to a unit area of the anode surface is the greatest during the attachment's dwelling, which causes strong anode evaporation under the constricted anode attachment and, therefore creation of craters. If we assume that t and a final depth h of the craters investigated are directly proportional then we can say that craters with the fixed length l and a depth h that is greater than the certain fixed depth H were investigated. The reference fixed depth H corresponds to the constant T. At $p = 101$ kPa, the following formula was used:

$$t > T = \tau \left(\frac{l}{l_{\mathrm{ref}}} \right) \left(\frac{U_{\mathrm{ref}} I_{\mathrm{ref}}}{\bar{U}_{\mathrm{ca}} I} \right), \tag{4.6}$$

where $l_{\mathrm{ref}} = 0.5$ mm and $U_{\mathrm{ref}} I_{\mathrm{ref}} = U_{300\mathrm{A}} \cdot 300$ A are the reference length of craters and the reference arc electric power, respectively. τ is a time constant to change the fixed value of T. At $p \leq 101$ kPa the formula was simplified to:

$$t > \tau = \text{constant}, \tag{4.7}$$

because in this case $l = l_{\mathrm{ref}} = 0.5$ mm and $\bar{U}_{ca} I = U_{\mathrm{ref}} I_{\mathrm{ref}} = 50.6 \pm 0.5$ kW. The reference values l_{ref}, $U_{\mathrm{ref}} I_{\mathrm{ref}}$ were chosen arbitrarily, and they can be chosen in many different ways, according to the range of crater lengths or possible arc powers. Their purpose is only to relate/scale attachment's dwellings at different investigated lengths l and different used powers $\bar{U}_{ca} I$. The scaling by l_{ref} is needed because for a given depth h and power $\bar{U}_{ca} I$, the longer length l, the longer the time t the attachment needs to make a crater with that given depth h. And the scaling by $U_{\mathrm{ref}} I_{\mathrm{ref}}$ is needed because for a given depth h and length l, the higher the arc power, the shorter the time t the attachment needs to make a crater with that given depth and length. In other words, for investigation of, for example, longer craters, we need to find dwellings with a greater constant T than in the case of shorter craters.

The arc voltage waveform can be used for finding the attachment's dwelling under the assumption that the change of the arc voltage is caused only by the attachment movement. This assumption is not obvious, however. Sometimes the length of the electric arc and consequently the arc voltage can change even if the attachment does not move at all, because of plasma fluctuations in the electric arc. However, those fluctuations of the electric arc are usually fluctuations caused by Kelvin-Helmholtz instability that are mostly periodic [54]. If they are periodic, they will not be a cause of the almost horizontal parts of the arc voltage waveform that represents the attachment's dwelling.

Arc voltage waveforms, in the case of the attachment's dwelling, are useful when we need a better time resolution (in our case it was 13 ns) and better statistics resulting from low computer memory requirements, compared with the videos taken by a high-speed camera. In the case of using arc voltage waveforms instead of time dependence of the attachment position, the voltage range X must be converted to the lengths l by multiplying the average ratio $\overline{U/L}$ (Fig. 4.4) of

the voltage drop U and the corresponding distance L. This conversion, however, brings additional uncertainty into the results. Arc voltage waveforms are also useful when the attachment's movement cannot be directly observed by a high-speed camera, for example in the case of gas plasma torches. In the case of gas plasma torches, sometimes it is possible to observe the attachment's movement, but not in such detail as in the case of a hybrid or water plasma torch with an external anode. Additionally, the anode arc attachment in gas plasma torches often moves in spirals or other circular trajectories, which makes observation of the anode attachment even more difficult.

It is evident that for a given electric arc power, the anode erosion is higher at a lower average attachment speed because, in that case, a smaller part of the anode receives the total thermal energy from the arc. The limit case is when the anode is not rotating, then only a narrow part of the anode under the plasma jet is exposed to the entire heat flux from the arc. Szente [[55]] also reported that cathode erosion rates are higher for lower arc velocities.

And it is during this attachment's dwelling that the attachment speed is low. Therefore the sum of all dwell times in a certain time interval can be proportional to the total anode erosion during this time interval. In the case that it is proportional to the anode erosion we can use it to quantitatively compare the anode erosion at different experimental conditions. And to not be dependent on the time interval we need to divide the sum of all dwell times by this time interval. The sum of all dwell times t (equations 4.6, 4.7) divided by the time interval of 0.1 s (at $p < 101$ kPa) gives us the variable called the "Proportion of all dwellings". For $p = 101$ kPa, the time interval by which the sum of all dwell times was divided was either 12.6 ms or 40 ms. This variable describes the portion of the investigated time interval during which the attachment's dwellings were present.

4.4 Determination of electric field and electric conductivity

The mean magnitude of the electric field inside the arc column above the anode was estimated by the following equation:

$$E_{\mathrm{arc}} = \overline{\left(\frac{U}{L}\right)}, \tag{4.8}$$

where the distance L and the corresponding arc voltage drop U (large-scale voltage fluctuations) are depicted in Fig. 4.4. L was determined from the high-speed camera footage and U from the measured arc voltage waveforms. The assumption was that U was a consequence only of L.

The time interval from which the averages (4.8) were taken was either 50 ms ($p < 101$ kPa) or 12.7 ms ($p = 101$ kPa). The assumption was that during the restrike, the electric potential drops across the former and the new constricted

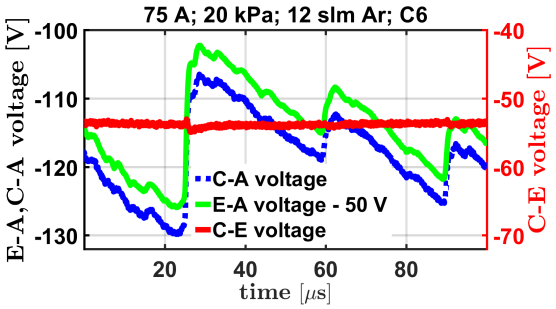

Figure 4.6: The arc voltage (lower saw-tooth dotted line, C-A voltage) vs. voltage between the exit nozzle and anode (upper saw-tooth solid line, E-A voltage reduced by 50 V) vs. voltage between the cathode and exit nozzle (nearly horizontal solid line, C-E voltage) waveform (adopted from [56])

attachment are exactly the same, even if in reality they are not.

To decrease the total uncertainty, we took into consideration only arc voltage drops larger than one-fourth (for $p = 101$ kPa) or larger than one-sixth (for $p < 101$ kPa) of the maximum arc voltage drop. Since the arc voltage waveforms were smoothed (to more easily find maxima and minima) and that smoothing decreased drops U, finally the value of 2 V (for $p = 101$ kPa) or 1V (for $p < 101$ kPa) was added to U values, to compensate that decrease.

The change in arc voltage (cathode-anode voltage: C-A voltage) is caused by the change in voltage between the exit nozzle and anode (E-A voltage) because the difference of C-A and E-A voltage, that is to say, the voltage between the cathode and exit nozzle (C-E voltage), is almost a constant (Fig. 4.6). And the change in E-A voltage is caused by the movement of the anode arc attachment. Therefore the assumption that U is a consequence of L (Fig. 4.4) is justified.

According to the numerical model of Jenista [57], the electric field inside the torch chamber close to the exit nozzle (there are not data outside the torch chamber) is almost constant, that is to say, it does not change significantly along the arc diameter, in the radial direction.

The electric field in the plasma measured by the pair of electric probes was calculated using the following equation:

$$E_{\text{probe}} = \frac{\Phi_{\text{probe1}} - \Phi_{\text{probe2}}}{1.7 \text{ mm}}, \tag{4.9}$$

where 1.7 mm is the distance between the centers of pins of the two electric probes used.

The mean electrical conductivity of the arc column in the anode area was estimated using the following equation:

$$\sigma_{arc} = \frac{1}{\pi R^2}\int_0^R 2\pi r\sigma(r)dr = \frac{J}{E} = \frac{E_{\text{arc}}}{\pi R^2}\int_0^R 2\pi r\sigma(r)dr \cdot \frac{1}{E_{\text{arc}}} = \left(\frac{I}{S}\right)\cdot\overline{\left(\frac{L}{U}\right)}, \tag{4.10}$$

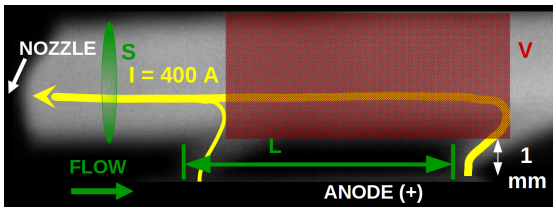

Figure 4.7: Camera image of the anode area, in C1, with the illustration of variables used in equation (4.10). The yellow curve with the arrow represents the arc current path during the restrike (adopted from [53])

where $J = I/S$ is the average magnitude of the arc current density in the anode area, S is the cross section of the arc current with radius R, and r is the radial coordinate. The dependence of the electrical conductivity on the axial position is neglected.

The variables used are illustrated in Fig. 4.7 and the MATLAB script that we used can be downloaded here: MATLAB script to calculate electrical conductivity.

S was estimated as the cross section of the bright part of the plasma jet visible on the high-speed camera footage through a gray optical filter. Because the position of the attachment creation and the attachment decay, as well the distance L between them, change in each restrike, the average value of σ_{arc} in equation (4.10) is taken over the set of all cylindrical volumes V depicted in Fig. 4.7. The change in the length L is less than 9 mm, and the change in the position of the attachment creation or decay is less than 5 mm. The upstream base of volumes V corresponds to the attachment creation position, and the downstream base corresponds to the attachment decay position. The cross section of volumes V is S. The bottom of the volumes V corresponds to the bottom of the bright main plasma flow and is approximately in the distance y_{E} from the anode surface (Table 3.2).

σ_{arc} average values were taken from the same time interval as E_{arc} average values.

4.5 Uncertainties of measurements

The vertical and horizontal error bars in all figures in this thesis represent the total combined standard uncertainties multiplied by the coverage factor 2, and thus provide a level of confidence of approximately 95 %. The total combined uncertainties consist of systematic and random uncertainties, and they were calculated according to the procedure in [58]. For example, the total combined uncertainty of a general variable $X = \prod_{k=1}^{N} X_{\mathrm{k}}$ was calculated as the following:

$$u(X) = 2\sqrt{(u(X)_{\mathrm{random}})^2 + (u(X)_{\mathrm{systematic}})^2}, \tag{4.11}$$

where $u(X)_{\mathrm{random}}$ is the estimated standard uncertainty of the mean of the variable X, and

$$u(X)_{\mathrm{systematic}} = \bar{X}\sqrt{\sum_{k=1}^{N}\left(\frac{u(X_k)_{\mathrm{systematic}}}{\bar{X}_k}\right)^2}. \tag{4.12}$$

The example is $X = \sigma_{arc}$, $X_1 = I$, $X_2 = 1/S$, $X_3 = \bar{L}$, $X_4 = 1/\bar{U}$, in equation (4.10).

The random/statistical uncertainties depend on the used time interval of the corresponding waveforms or time dependence, and their source is mainly the fluctuations in the plasma. The fluctuations were caused mostly either by turbulence or by slow stabilization of the plasma flow after changing working conditions. When we changed arc current I it was enough to wait for about 10 s while it stabilized itself. A change in the argon flow rate Ar required us to wait at least 30 s, and a change in the ambient pressure p required us to wait at least 2 min to be sure that the pressure value on the gauge's display was the same as the pressure around the plasma.

The systematic/non-statistical uncertainties should be the same for any investigated time interval; therefore they are listed in Table 4.1. When the probability distribution is rectangular, the partial systematic uncertainties are obtained by using a divisor of $\sqrt{3}$; in other cases the probability distribution is normal, with the divisor of 1.

Systematic standard uncertainty	**Partial standard uncertainties**	**Source of uncertainty**
$u(I)_{\text{systematic}} =$ $= \sqrt{\sum_{i=1}^{2} \left(u(I_{\text{i}})\right)^2} =$ $= 2$ A	$u(I_1) = 2$ A	Calibration of voltmeter
	$u(I_2) = \frac{1}{\sqrt{3}}$ A	Display resolution
$u(L)_{\text{systematic}} =$ $= \sqrt{\sum_{i=1}^{2} \left(2 \cdot u(L_{\text{i}})\right)^2} \approx$ $\approx \langle 0.0 \text{ mm}; 0.3 \text{ mm} \rangle$	$u(L_1) = \frac{0.5}{200\sqrt{3}}$ mm	Pixels $\rightarrow$ length conversion
	$u(L_2) =$ $= \frac{(10/6) \text{ µs} \cdot v_{\text{attachment}}}{5\sqrt{3}}$	Frame rate of 300,000 fps
$u(U)_{\text{systematic}} =$ $= \sqrt{\sum_{i=1}^{2} \left(u(U_{\text{i}})\right)^2} =$ $= 2$ V, 1 V	$u(U_1) = 2$ V, 1 V	PicoScope resolution
	$u(U_2) = \frac{2}{8\sqrt{3}}$ V, $\frac{1}{8\sqrt{3}}$ V	Smoothing of $U_{\text{ca}}(t)$
$u(\Phi)_{\text{systematic}} =$ $= \langle \frac{0.2}{\sqrt{3}} \text{ V}; \frac{1}{\sqrt{3}} \text{ V} \rangle$		PicoScope resolution
$u(d)_{\text{systematic}} = \frac{0.5}{\sqrt{3}}$ mm		Estimation of S
$u(\Delta t)_{\text{systematic}} = 2\frac{0.29}{\sqrt{3}}$ µs		Exposure time of 0.29 µs
$u(\Delta t)_{\text{U,systematic}} =$ $= \sqrt{\sum_{i=1}^{2} \left(2 \cdot u(t_{\text{i}})\right)^2} =$ $= 0.2$ µs	$u(t_1) = \frac{13}{\sqrt{3}}$ ns	Time resolution in U_{ca}(t)
	$u(t_2) = \frac{0.2}{\sqrt{3}}$ µs	Smoothing of $U_{\text{ca}}(t)$

Table 4.1: List of systematic / non-statistical uncertainties in used variables and their sources. The divisor of $\sqrt{3}$ was used in the case of rectangular probability distribution, and the divisor of 1 was used in the case of normal probability distribution

$\boldsymbol{u(I)_{\text{systematic}}}$:
The arc current I was measured with a panel digital voltmeter, a"WPB5135-DV

199.9 mV", which, according to its datasheet, has a measurement accuracy of ±0.2 % of full-scale ±2 digits.

The $\boldsymbol{u(I_1)}$ corresponds to the ±0.2 % of full-scale and was calculated as follows: (0.002·199.9mV)·(600A/60mV) = 4A. The calculation follows from the fact that the voltmeter measured the electric current through a "$U_{out} = 60\text{mV}; U_{in} = 150\text{mV}$" voltage divider connected to a "150 mV / 600 A" shunt/resistor. The current in the shunt was equaled to the arc current I. Uncertainties in the resistance of the shunt and voltage divider were neglected and the uncertainty 4 A was interpreted to be a double standard uncertainty. The $\boldsymbol{u(I_2)}$ corresponds to ±2 digits = 2 A because the last digit represented amperes (the display had 3 digits), and was interpreted as the double standard uncertainty too.

In equation (4.10), the value of I should not be precisely the value of the whole arc current, because a part of the arc current indeed flows to the anode through the less electrically conductive plasma around the attachment. According to the results published in [59], the part of the arc current that flows to the anode around the attachment could be about 1 %. In such a case, in equation (4.10), there would be "0.99 I" instead of "I". This additional uncertainty is probably partially obtained in the random standard uncertainty of the arc current, caused by the arc current fluctuations. This random standard uncertainty of the arc current was 2 A/$\sqrt{3}$.

$\boldsymbol{u(L)_{\text{systematic}}}$:
The sum in $u(L)_{\text{systematic}}$ contains the coefficient 2 because the uncertainties $u(L_1)$ and $u(L_2)$ play a role at both ends of the distance L. As mentioned above, the conversion from pixels to millimeters was obtained by the comparison of the known length of 2.0 ± 0.5 cm in a representative image with the corresponding number of pixels of about 200. This conversion represents $\boldsymbol{u(L_1)}$.

The uncertainty $\boldsymbol{u(L_2)}$ is there to fit L to U in the computation of σ_{arc}. The value of 10/6 µs in $u(L_2)$ points to the fact that the average duration of restrike (found in arc voltage waveforms that have time resolution of 13 ns) is 3 ± 1 µs and the time between two consecutive high-speed camera frames was 10/3 µs. Therefore a new attachment could be created anytime between two following camera frames. The position of the attachment was detected in all camera frames. To explain $u(L_2)$, let us consider a special case when two consecutive restrikes last 10/3 µs or more (each of them). The first restrike happens for example in the time interval of $\langle 0\ \mu\text{s}; 10/3\ \mu\text{s}\rangle$ and the second restrike happens for instance in the time interval of $\langle 10\ \mu\text{s}; 10 + 10/3\ \mu\text{s}\rangle$. The beginning of these time intervals represents a maximum in the corresponding arc voltage waveform and the end of these time intervals represents a minimum in the same arc voltage waveform. A limit case is when the camera takes the attachment position at the time of 10/6 µs, the attachment position is interpreted as the position of creation, and then the camera takes the attachment position also at the time of $10 + 10/6$ µs, and the corresponding attachment position is interpreted as the position of decay. In such a case, there is a distance of 10/6 µs·$v_{\text{attachment}}$ at both ends of the restrike period that has been traveled by the attachment, but it is not visible in the time dependence of the axial attachment position.

This means that the value of L obtained from high-speed camera frames is,

in our example, about $2 \cdot (10/6)$ µs $\cdot\, v_{\text{attachment}}$ lower than its real value. However, if one L is lower than its actual value, the adjacent L must be greater than its actual value. Therefore, to some extent the uncertainty $u(L_2)$ cancels itself, and that extent is estimated by the empirical coefficient of 1/5.

The total standard uncertainty in the position of the electric probes was at least 0.5 mm because the probes' diameter was 1 ± 0.1 mm.

$\boldsymbol{u(U)_{\text{systematic}}}$:
The PicoScope resolution uncertainty was 1 % of full-scale on the used input voltage range for one single voltage value, and it was interpreted as the double standard uncertainty. By using a high-voltage probe 1000x, the input voltage range for $p = 101$ kPa was ± 500 mV and the input voltage range for $p < 101$ kPa was ± 200 mV. The value of U is not a single measured value, but the comparison of two closely spaced values; therefore the uncertainty $\boldsymbol{u(U_1)}$ is lower than 1 % of full-scale on the used input voltage. This is a Non-linearity error and Differential Non-Linearity error of the Analog-to-Digital Converter in the PicoScope, and the noise level error. The first value of $u(U_1)$ in Table 4.1 concerns $p = 101$ kPa and the second value of $u(U_1)$ concerns $p < 101$ kPa.

The uncertainty $\boldsymbol{u(U_2)}$ follows from the fact that the smoothing of the arc voltage waveform in MATLAB program decreased U values about 2 V (for $p =$ 101 kPa) or 1V (for $p < 101$ kPa). However, the estimated decrease of 2 V or 1 V was finally added back to U values; therefore, there is an estimated empirical factor of 1/8, in $u(U_2)$.

The systematic uncertainty in the single voltage values U_{ca} in equation (4.6) was 0.5 ·(1 % of 500 mV) * 1000 = 3 V because the uncertainty 1 % of full-scale was interpreted as the double standard uncertainty.

$\boldsymbol{u(\Phi)_{\text{systematic}}}$:
The probe potential Φ_{probe} was measured by using PicoScope, a T5100 oscilloscope probe, and a voltage divider 2:1. The value of $u(\Phi)_{\text{systematic}}$ depends on the 1 % of the used input voltage range in the PicoScope that was ± 20 V, ± 50 V, or ± 100 V.

$\boldsymbol{u(d)_{\text{systematic}}}$:
The cross section $S = \pi d^2/4$ of the arc current, in equation (4.10), was only estimated as the cross section of the bright plasma jet visible on the high-speed camera footage through a gray optical filter. The using of the gray optical filter 1000x gave the same estimation as the using of the gray optical filter 8x.

$\boldsymbol{u(\Delta t)_{\text{systematic}}}$:
The attachment movement during the exposure time of 0.29 µs could not be distinguished because it is the time during which a high-speed camera image was created. The coefficient 2 is there because Δt is a difference of two time values. This uncertainty was used in the computations of restrike periods from the time dependence of the axial attachment position.

$\boldsymbol{u(\Delta t)_{\mathrm{U,systematic}}}$:
This uncertainty was used in the computations of uncertainties of restrike periods from arc voltage waveforms where the time resolution was 13 ns ($\boldsymbol{u(t)_1}$) and where the maxima and minima were shifted (to the left and the right, respectively) about 2 µs because of the smoothing in the MATLAB program. The value of 0.2 µs in $\boldsymbol{u(t)_2}$ was estimated by observing that all maxima or minima were shifted almost equally, and the greatest difference between the shifts of two following maxima or two following minima seemed to be about 0.2 µs.

In the case of ambient pressure p and argon flow rate Ar, the total combined standard uncertainties multiplied by the coverage factor 2 were estimated from the observation of changes in the measured values during the experiment: $\boldsymbol{u(p)} =$ 0.5 kPa,
$\boldsymbol{u(Ar)} = 0.5$ slm.

5. Results and Discussion

This section uses results mainly from the three publications: [56], [53], and [52].

5.1 Properties of the plasma jet

The pressure inside the plasma torch chamber, where the electric arc is stabilized (Fig. 2.4), is typically about 101 kPa [60] higher than the pressure outside the plasma torch. The pressure outside the torch is 101 kPa (atmospheric pressure) or less (when it is inside a low-pressure chamber). The result is that the plasma in the stabilized part of the torch, created from water and gas (typically argon), flows outside the torch at a speed that is typically in the range of 1-5 km/s [61], depending on the conditions. The plasma jet is the whole plasma flow outside the torch chamber, but in high-speed camera images it is often only the brightest part that is visible, with a diameter approximately equal to the diameter of the exit gap. For the purposes of this thesis, this brightest part of the plasma jet is called the bright plasma jet. With decreases in the pressure outside the torch or with increases in arc power, the average speed of the plasma flow increases. Increases in arc power cause greater water evaporation and consequently higher pressure inside the torch chamber.

For a better idea, Table 5.1 shows selected low and high values, not necessarily the lowest and greatest possible ones, of some plasma parameters, depending on I, p, Ar, D, and x_A. The value of x_A is not mentioned in the cited publications; however, according to our experience we guess that $x_A = 3.8$ mm, because the configuration C1 is the most used configuration at atmospheric pressure. The plasma densities of (4.3 ± 0.2) g/m^3 and (13 ± 2) g/m^3 correspond to the electron number densities of $(3.3 \pm 0.1) \times 10^{23}$ m^{-3} and $(5.2 \pm 0.2) \times 10^{23}$ m^{-3} respectively.

The plasma temperature was measured in the center of the plasma jet, 2 mm downstream from the exit nozzle, utilizing emission spectroscopy. The plasma speed was determined at the nozzle exit from the measured plasma temperature and from the calculated net power dissipated inside the torch chamber (through calculated plasma gas composition), assuming LTE. According to Jensita's model [62], the mean free path of electrons for $I = 120$ A, $p = 101$ kPa, 12 slm of Ar, $x = 12.2$ mm is $(1.8 \pm 0.4) \cdot 10^{-6}$ m in the center of the plasma jet.

We estimated the speed uncertainty as a minimal uncertainty according to the publication [22], and the temperature uncertainty as a minimal uncertainty according to a conversation with Dr. Sember and Dr. Maslani, who measured the plasma temperature of the hybrid plasma torch. The amount of evaporated water from the stabilizing water vortex in the plasma for different working conditions has not been precisely measured up to now. It has only been estimated, years ago, by measuring the inflow and outflow of water into the stabilizing water vortex during a period of a few hours.

Often, the value of 18 g/min is used, which is about 1 mol of evaporated water per minute. The evaporation rate of the water is driven by energy losses from the

I / Ar	Plasma speed [± 500 m/s]	Plasma temperature [± 500 K]	Plasma density [g/m^3]	Kinematic viscosity [m^2/s]	Debye length [m]
150 A / 22 slm	800	14,000	13 ± 2	$(8.3 \pm 0.8) \cdot 10^{-3}$	$(1.6 \pm 0.1) \cdot 10^{-8}$
600 A / 40 slm	7,500	22,000	4.3 ± 0.2	$(4.6 \pm 0.1) \cdot 10^{-3}$	$(1.80 \pm 0.04) \cdot 10^{-8}$

Table 5.1: Selected plasma parameters for the hybrid plasma torch [9], [63], [35]. $D = 6$ mm, $p = 101$ kPa

arc by radiation and radial conduction; therefore, it depends mostly on the arc current I and only a little on the argon flow rate Ar. In [6], it is mentioned that for the range of I = 300-500 A (and p = 101 kPa), the water evaporation rate is between 6 and 18 g/min. A significant amount of water is released into the jet in the form of water droplets, but we assumed that this amount is separated from the plasma. These water droplets, visible even in high-speed camera video footage, fly mostly around the bright plasma jet as they are released from the water vortex in the place immediately behind the exit nozzle.

According to [6], 22 slm of Ar represents about 70 molar % of Ar (the molar % are equal to the volume %) for I = 300 A (there is no value for I = 150 A), and 40 slm of Ar represent about 55 molar % of Ar for I = 500 A (there is no value for I = 600 A). These values are needed to obtain the calculated values of steam-argon plasma properties from [35], listed in the last three columns of Table 5.1. In the hybrid plasma torch, the majority of the argon that is used is sucked away with the water that stabilizes the electric arc, and less than half of it flows outside into the anode area.

The plasma speed in Table 5.1 was measured by using five photodiodes according to the method described in Section 4.2. There is, however, also another way to measure the plasma speed in the anode area of the hybrid plasma torch. We have found that we can use enthalpy probes to measure it, if the arc power is low enough. The enthalpy probe inside the bright plasma jet is shown in Fig. 5.1.

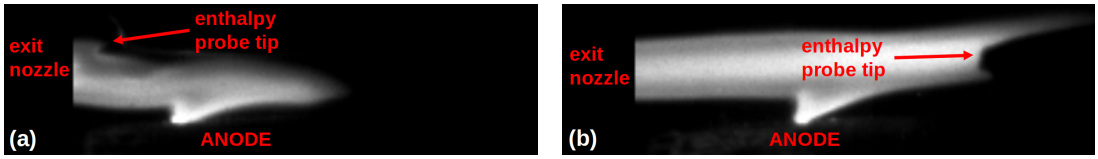

Figure 5.1: ***(a)*** *Camera image of the anode area with the tip of the enthalpy probe about* 3 mm *from the exit nozzle (only half of the probe tip is immersed in the bright plasma jet) and* ***(b)*** *about* 22 mm *from the exit nozzle (in this case the probe tip is between the bright plasma jet and the camera, in a position very close to the bright plasma jet).* I = 40 A, 12 slm *of Ar,* p = 20 kPa, *C6*

While the probe tip was inside the bright plasma jet above the anode (Fig. 5.1(a), the Tekna enthalpy probe system reported the heat power at the probe

tip as being equal to about 500 W, which is below the safety limit of the probe. Fig. 5.1(b) is here to show rather the dimensions of the probe tip, which had an inlet diameter of 1.3 mm and an outlet diameter of 4.60 ± 0.05 mm, in comparison with the bright plasma jet at $I = 40$ A. Fig. 5.1(a) proves that the heat flux from the plasma jet to the probe was not too high for the enthalpy probe even in the hottest part of the plasma jet, close to the exit nozzle. According to the high-speed camera video footage, which shows the radiation emitted from the probe, and according to the corresponding software report, the probe tip was not overheated at $I = 40$ A. The tip of the enthalpy probe was cooled down by a water circuit inside the probe; the details about this enthalpy probe can be found, for example, in [9]. We were not able to place the probe precisely into the middle of the bright plasma jet because it was necessary to hold the whole probe, together with its shield, with both hands. Before the experiment, the probe was electrically isolated from the power socket by using a 220 V / 4 A isolation transformer; thus, during the experiment, the work gloves of the experimenter touched the metal shield of the probe with an electric potential equal to the electric potential of the plasma (which was, according to the electric probe measurements, about -35 V). In the future, we plan to use a positioning system controlled by a computer for the enthalpy probe.

The Reynolds number (equation 2.26) in our experiments was greater than 300 for all working conditions (Table 3.1, Table 5.1). Regarding equation (2.26), U corresponds to the plasma speed and L corresponds to the diameter D of the exit nozzle. For axisymmetric free-jet flow, the critical Reynolds number for the transition from laminar to turbulent flow is about 10-30 [41]. The plasma jet of the hybrid plasma torch is not free and not perfectly axisymmetric; therefore, in this case we do not know the exact value of the critical Reynolds number. However, we suppose that the critical Reynolds number for the real hybrid plasma torch is not higher than 300, and therefore the bright plasma jet of the hybrid plasma torch is fully turbulent throughout its whole length for all working conditions. The turbulent vortices and eddies can be seen in Fig. 5.2 and Fig. 5.3; they are generated by Kelvin-Helmholtz instability and propagate downstream. The schlieren edge in the case of Fig. 5.2 was a disk screen with a diameter of 1.05 mm that was symmetrically inside a circle with a diameter of 9 mm (it is depicted below the blue arrow). In the case of Fig. 5.3, a knife-edge was used. The image in Fig. 5.2 was obtained by a schlieren arrangement that was similar to the Z-type (Fig. 2.17), and the image in Fig. 5.3 was obtained by the Carl Zeiss system for schlieren imaging (Fig. 3.2).

In thermal plasma jets, there is usually a laminar core region close to the exit nozzle [64]; however, this is because of a lower Reynolds number in such cases. Pfender *et al.* [64] estimated their Reynolds number at the exit of their gas plasma torch to be approximately 100. In gas plasma torches, the plasma temperature is not so high as in the case of the hybrid plasma torch. Therefore the kinematic viscosity of the plasma in gas plasma torches is highest in the center of the plasma jet. This means that in the case of gas plasma torches, the core of the jet (at least close to the exit nozzle) has the smallest Reynolds number and is, therefore, usually laminar. In the case of the hybrid plasma torch, the situation

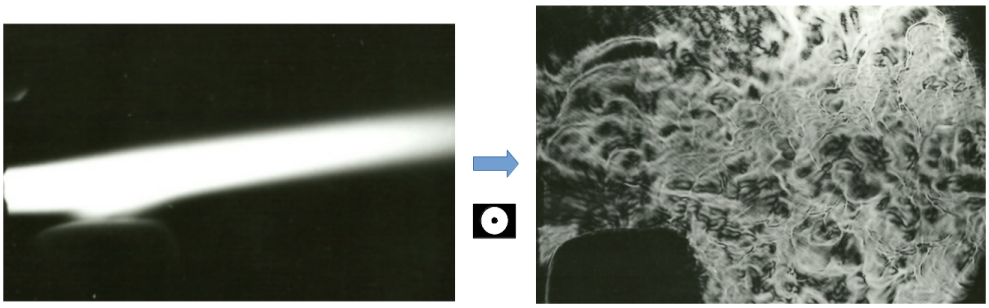

Figure 5.2: A camera image (left) and the corresponding schlieren image (right) of the plasma jet created by the water stabilized plasma torch, taken in 1995. I = 300 A, p = 101 kPa. Under the blue arrow, the schlieren edge that was used is depicted: a disk screen inside a circle

is different. The plasma temperature increases toward the center of the jet so significantly that the kinematic viscosity can reach its maximum somewhere around the center of the jet and start to decrease farther toward the center. The graph of the theoretical temperature dependence of dynamic viscosity, which is similar to the graph of the temperature dependence of kinematic viscosity, for the hybrid plasma torch is shown in [35]. Therefore, the Reynolds number does not have to be the smallest in the core of the plasma jet created by the hybrid plasma torch.

The diameter of turbulent vortices propagating downstream (visible in Fig. 5.3) increases with decreases in the arc current and argon flow. The values of the diameter in Fig. 5.4 were obtained from visual observation of the schlieren videos, and their uncertainty was estimated at 0.2 mm.

The Kelvin-Helmholtz instability generated not only turbulent vortices but also hydrodynamic waves in the plasma jet that can be directly observed by a high-speed camera [52]. The speed (Fig. 5.5) and wavelength of these hydrodynamic waves in the anode area were directly calculated from consecutive high-speed camera images. The hydrodynamic waves started to be clearly visible just above the anode as they propagated downstream. In particular, they were strongly amplified when they propagated just above the anode attachment. For $p = 101$ kPa, $x_A = 4.5$ mm, and $y_E = 0.9$ mm, their average wavelength was 7 ± 1 mm, and this seemed to be independent of the arc current ($I = 300$ A, 400 A, 500 A) and argon flow rate ($Ar = 12$ slm, 22 slm); it only increased slightly with the distance x from the exit nozzle.

5.2 Transitions for plasma flow and anode attachment

Regarding the hybrid plasma torch, there are two basic transitions:

1) The transition from subsonic to supersonic flow.

In the working conditions used in most experiments and plasma spraying applications, the hybrid plasma torch has a subsonic plasma jet. The easiest way

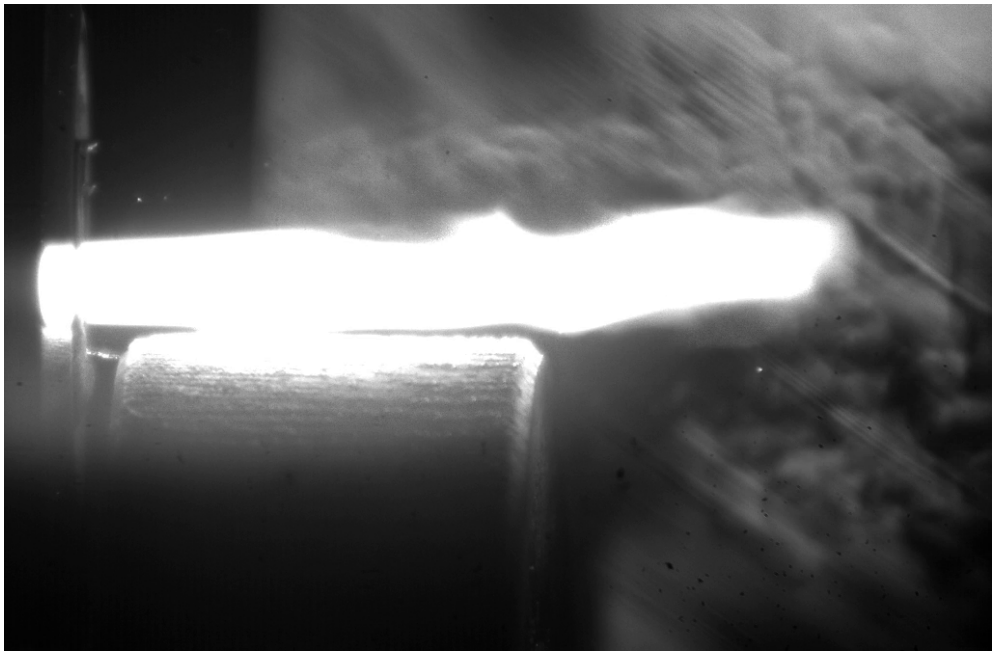

Figure 5.3: A schlieren image of the plasma jet created by a WSP®-HR hybrid plasma torch, taken in 2018. $I = 171$ A, $p = 62$ kPa, $Ar = 22$ slm, C6. Here, the turbulent vortices are visible only around the bright/white part of the plasma jet. The corresponding video can be seen in the Supplement to this thesis (VIDEO 6)

to have a supersonic plasma jet is to reduce the ambient pressure. In [61] the transition from subsonic to supersonic flow was found, according to the Mach number, at an ambient pressure of about $p = 30$ kPa, for $I = 200$ A. The anode configuration used in [61] was probably C3, but it is not mentioned in the article. We found the pressure for the transition from a subsonic to supersonic plasma jet directly from visual observations of the most visible expansion zone in the supersonic plasma jet. The expansion zone has a low brightness and is located between two compression zones with higher brightness. The most visible expansion zone is usually the one that is closest to the exit nozzle. In most cases, only one expansion zone was visible in the high-speed camera footage; however, in rare cases more expansion zones were visible (Fig. 5.6). The second (in the downstream direction) expansion zone appears mainly when the constricted anode arc attachment is far enough from the exit nozzle (Fig. 5.6(a),(b)); this is because the anode jet interacts strongly with the main plasma flow and breaks the supersonic structure of the jet. However, when the constricted attachment is small and the anode jet weak, the second expansion zone can appear even inside the anode jet (Fig. 5.6(c)). In Fig. 5.6(c), there was accidentally a metal cover between the camera and the bright plasma jet; therefore, the first compression zone was not visible.

The visually found values of the transition pressure are summarized in the upper part of Table 5.2. The transition was accompanied by a sudden increase in the slope of the E-A voltage pressure dependence (Fig. 5.7). The average values for the E-A voltage in Fig. 5.7 were calculated within a time interval of 50 ms.

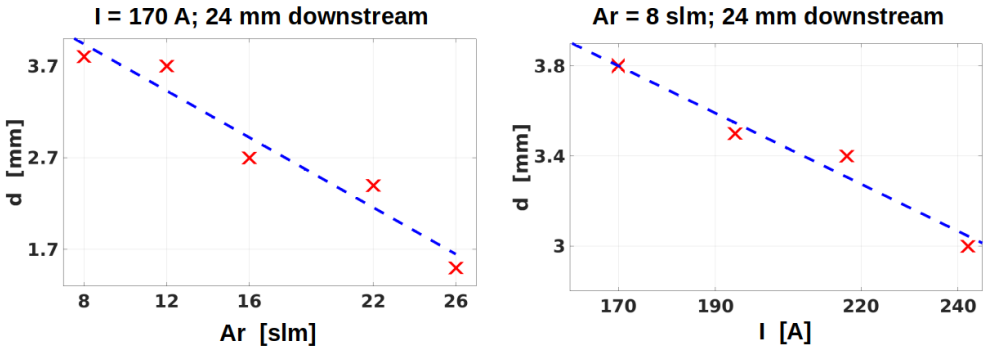

Figure 5.4: Argon flow dependence (left) and arc current dependence (right) of the diameter d of the turbulent vortices in the place immediately behind the anode (24 mm downstream from the exit nozzle). p =62 kPa, C6

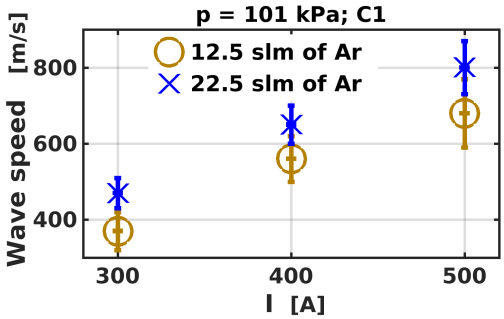

Figure 5.5: Arc current dependence of the average hydrodynamic wave speed in the anode area (data adopted from [52])

Another way to obtain a supersonic plasma jet is to increase the plasma flow speed significantly (by increasing the arc current and argon flow rate), even at atmospheric pressure. This was done by Kavka *et al.* [63], who experimentally obtained a supersonic plasma jet at $I = 600$ A; however, the supersonic structure of the jet was not visible, probably because of the corresponding intense plasma jet radiation. Jenista *et al.* [65] confirmed the existence of a supersonic plasma jet at $p = 101$ kPa, $I = 600$ A by using a numerical model of a hybrid-stabilized argon-water arc.

2) The transition from a constricted to a diffuse anode arc attachment.

The constricted and diffuse anode arc attachment, with the corresponding arc voltage waveform, is shown in Fig. 5.8.

In the restrike mode, the constricted attachment in the hybrid plasma torch almost always moves downstream along the anode surface and only very occasionally moves a little (less than 1 mm) upstream and then it continues to move downstream. Up to now, only the restrike mode with the constricted anode arc attachment has been used in practical applications of the hybrid plasma torch. When using a high-speed camera, we have never observed takeover mode in the case of the hybrid plasma torch; even if the arc voltage waveform sometimes seemed to be sinusoidal. We obtained the steady mode with the constricted anode arc attachment, but only in the direction of the plasma flow. It is not possible to obtain it in all directions because of the anode, which rotates and carries the attachment in the direction of its rotation.

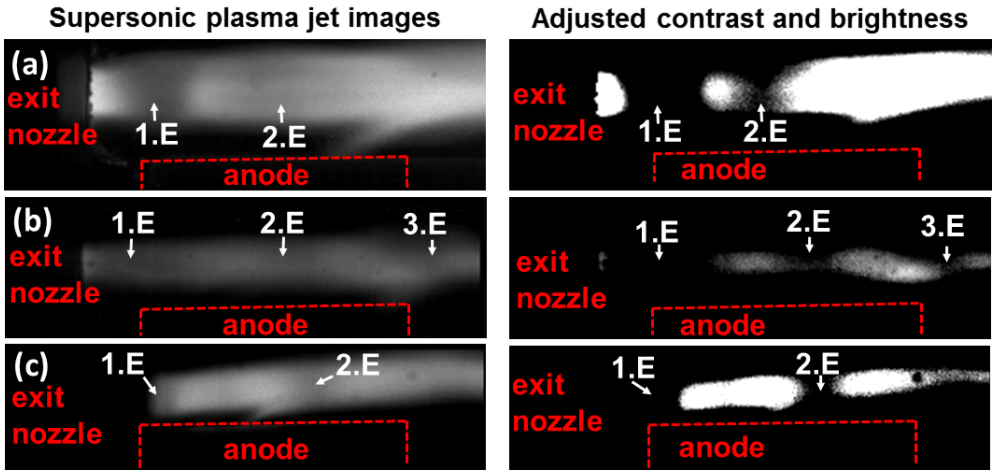

Figure 5.6: Camera images showing expansion zones (1.E, 2.E, 3.E) alternating with compression zones (brighter areas of the plasma). ***(a)***,***(c)*** $p = 35$ kPa, $I = 300$ A, 12 slm *of Ar, C6;* ***(b)*** $p = 50$ kPa, $I = 200$ A, 22 slm *of Ar, C6 (adopted from [56])*

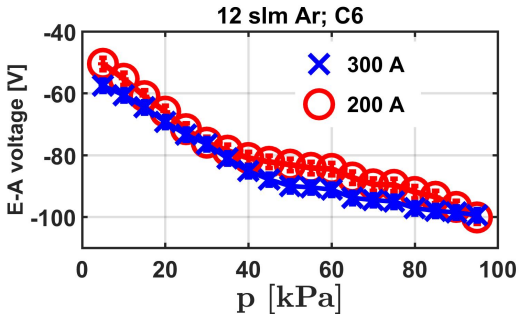

Figure 5.7: The average (in time) voltage between the exit nozzle and anode at different ambient pressures for two values of the arc current (adopted from [56])

One way to obtain the steady mode, in the axial direction, is to reduce the argon flow and arc current (and consequently the plasma flow speed) under certain transition values that depend on the anode configuration and ambient pressure. For $C2_{INC}$, the steady mode already happened at $I = 200$ A and 8 slm of Ar (VIDEO 7 in the Supplement to this thesis). The second way is to increase the distance y_E (Fig. 5.9), again to a certain transition value that depends on the distance x_A, arc current, argon flow rate, and ambient pressure. In both ways, the steady mode is the result of the decrease in the drag force $\boldsymbol{F_D}$ acting on the constricted attachment in the downstream direction.

In Fig. 5.9, the two images were taken at different times, as the pixel resolution was not enough for such a large image showing the whole attachment together with the plasma flow. An electrical breakdown close to the exit nozzle did not happen, and so the restrike in the direction of the plasma flow stopped. However, because of the rotation of the anode, the attachment was moving slowly with a restrike in the direction perpendicular to the images, that is to say in the direction of the rotation of the anode. The rotating anode carried the attachment down to about 4.4 mm, and the corresponding average restrike period in that perpendicular movement was about 1 ms, with large voltage drops of about 150 V.

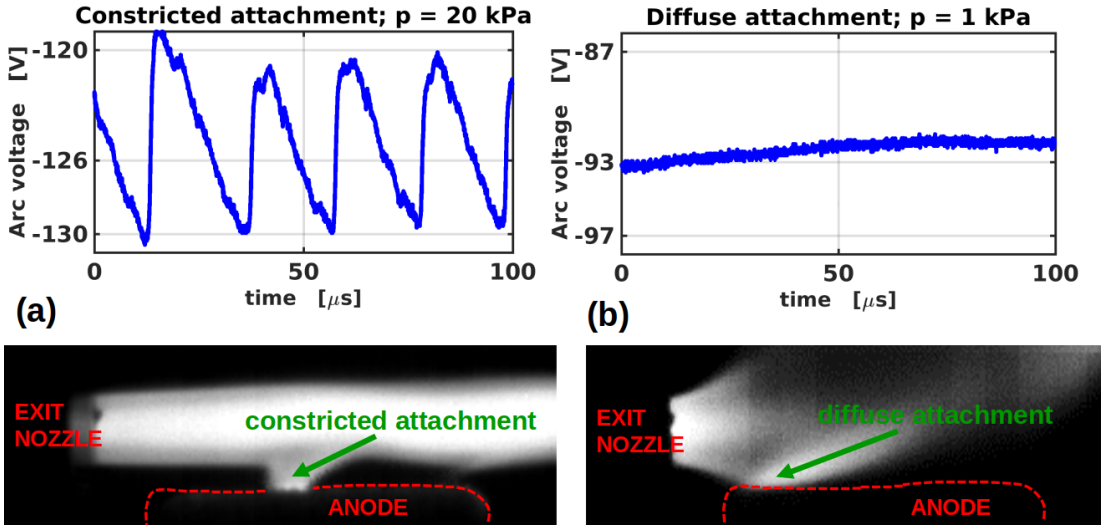

Figure 5.8: Camera image and arc voltage waveform for a subsonic plasma jet with a constricted anode arc attachment ***(a)*** *and for a supersonic plasma jet with a diffuse anode arc attachment* ***(b)****. $I = 75$ A, 12 slm of Ar, C6*

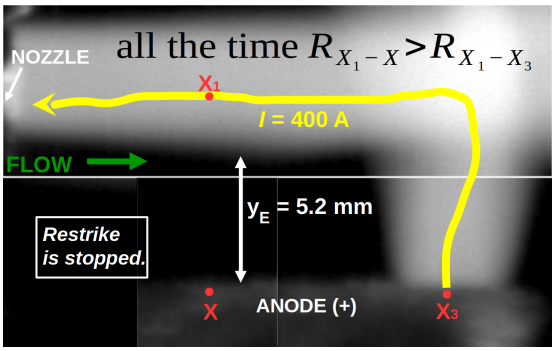

Figure 5.9: Two combined camera images (separated by the horizontal white line) showing the arc in the steady mode regarding the direction of the plasma flow. The electrical resistivity R *between* x_1 *and* x *is greater than that between* x_1 *and* x_3*. $p = 101$ kPa, $I = 400$ A, 12 slm of Ar, C3 (adopted from [53])*

Despite all the previous studies, the attachment movement, as well as the restrike mode itself, are not yet well-understood phenomena. The way the one-way steady mode was obtained (by increasing the distance y_E) offers the following interpretation of the restrike mode [53]: electrical breakdown between the anode and the main plasma flow probably happens in random places where turbulence in the main plasma flow causes a decrease in the distance y_E between the main plasma flow and the anode surface to such an extent that an electrical breakdown can happen.

These random locations of a new breakdown are always closer to the exit nozzle than the former position of the attachment, and this is because of at least two reasons. First, the voltage between these random upstream locations and the anode is higher than between the downstream locations and the anode, as the negative electric potential increases from the cathode towards the anode. Second, the distance y_E is smaller in these random upstream locations than in the downstream locations because the anode jet raises the main plasma flow and therefore causes its inclination upward.

Then the electrical breakdown creates a new current path where the plasma temperature and electric current increase and the electrical resistivity of the

plasma decreases. For a 2-4 μs, there are two anode arc attachments, the former and the new one. After a moment, the electric current in the new current path is higher than that in the former current path, and the electrical resistivity of the new path is suddenly lower than that of the former path. Therefore the former attachment ceases to exist, and only the new attachment remains. The process repeats.

The shape of the arc voltage waveform is a good indicator of the type of the anode arc attachment when a camera is not available. When the waveform is sawtooth-shaped (Fig. 5.8(a)), it means the attachment is constricted and moves in a restrike mode.

When the arc voltage waveform is nearly a constant (Fig. 5.8(b)), it means that the attachment is almost not moving. And if we do not have such an atypical anode configuration as C3 (Fig. 5.9), we can say that the attachment must be diffuse when the arc voltage waveform is nearly a constant. As mentioned in the next section, 5.3, this constant is not a long-term one, and it increases slowly with time.

The easiest way to obtain a diffuse anode arc attachment is to reduce the ambient pressure (as in the case of the transition to the supersonic plasma jet). The decrease in the ambient pressure causes an expansion of the plasma jet, and this expansion causes the cold gas boundary layer between the anode and the main plasma flow to be narrower. At very low ambient pressures, the bright plasma jet is so expanded (enlarged in its diameter) that it touches the anode surface and the anode arc attachment is diffuse. As we can see from Table 5.2, with common anode configurations such as C6, the plasma jet must be supersonic to have a diffuse anode arc attachment.

Subsonic-supersonic flow transition		
Anode configuration	$I = 200$ A	$I = 300$ A
C6	40 ± 5 kPa	40 ± 5 kPa
C5	32 ± 2 kPa	33 ± 2 kPa
Constricted-diffuse attachment transition		
Anode configuration	$I = 200$ A	$I = 300$ A
C6	17 ± 2 kPa	25 ± 2 kPa

Table 5.2: Ambient pressures for the subsonic-supersonic plasma flow transition and the constricted-diffuse anode arc attachment transition, at 12 slm *of Ar (adapted from [56])*

The expansion of the plasma jet and the connection of its bright part with the anode surface through a diffuse attachment can also be obtained in another way, not only by reducing the ambient pressure. We made the transition from a constricted to a diffuse anode arc attachment at atmospheric pressure by reducing y_{E} to slightly negative values (that correspond to the anode surface slightly above the level of the bottom edge of the nozzle gap) and placing the anode closer to the exit nozzle (reducing the horizontal distance x_{A} between the anode and the exit nozzle). The high value of the arc current, $I = 500$A, helped to expand the

plasma jet, because the higher the arc power is, the greater the diameter of the bright plasma jet is. A camera image of this diffuse attachment is shown in Fig. 5.10(b). It is an image taken a little from the right side, for $y_E = -0.8$ mm, so that the left edge of the anode seems to be closer to the exit nozzle than it really was.

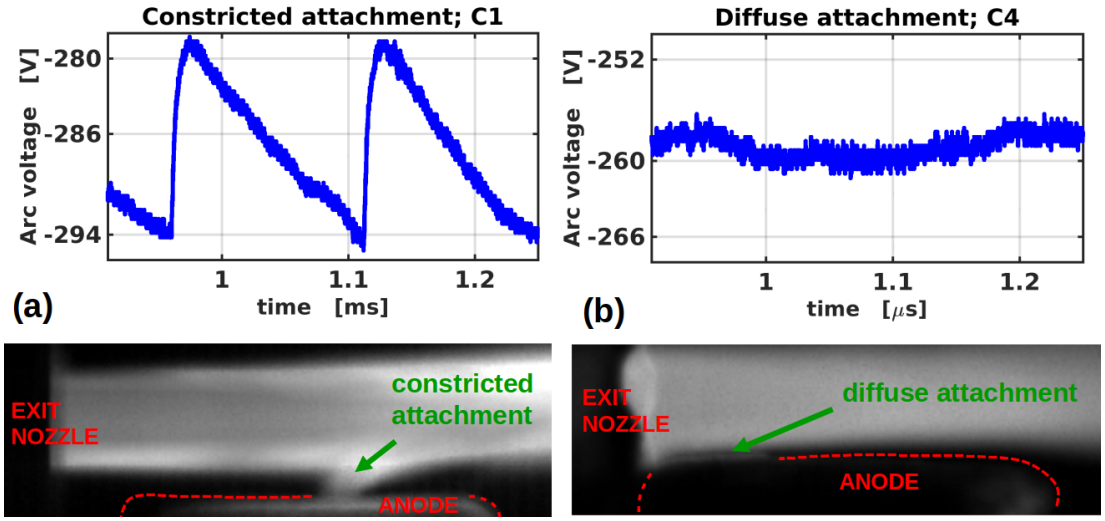

Figure 5.10: Camera image and arc voltage waveform for ***(a)*** *a constricted anode arc attachment and for* ***(b)*** *a diffuse anode arc attachment.* $I = 500$ A, $p = 101$ kPa, 12 slm *of Ar*

This diffuse anode arc attachment at atmospheric pressure will be discussed further in Section 5.4.

The transitions from the constricted to the diffuse anode arc attachment were accompanied by the occurrence of multiple anode attachments that were a combination of diffuse and weakly constricted attachments. The same was observed during the transition in other kinds of plasma torches [66, 67].

5.3 Anode arc attachment movement

In this section, the movement of the constricted anode arc attachment will be described, because the diffuse anode arc attachment does not move significantly along the anode surface. The movement of the attachment influences the stability of the plasma jet and the heat flow from the arc to the anode. The dynamic drag force $\boldsymbol{F_D}$ and magnetic Lorentz force $\boldsymbol{F_L}$ acting on the constricted attachment are depicted in Fig. 5.11.

The upper curvature of the attachment is caused by the inclination of the attachment downstream, and it is very visible. The lower curvature of the attachment is not visible [52, 53]; however, it should exist because the electric current flowing through the attachment into the anode must enter the anode (an equipotential surface) normally, that is to say by the shortest path.

This thesis describes the movement of the attachment projected into the axial direction x. The small component of the movement of the attachment in the

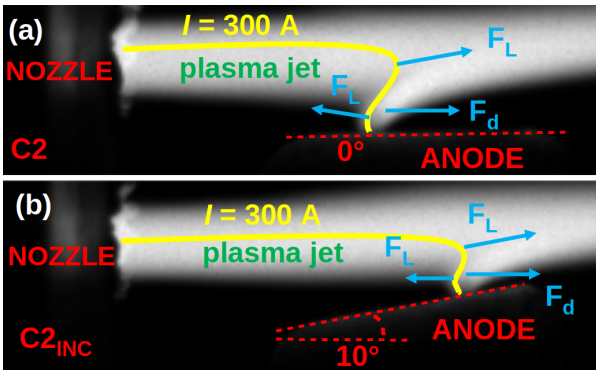

Figure 5.11: Camera images of the anode area in ***(a)*** *C2 and* ***(b)*** *$C2_{\mathrm{INC}}$ anode configuration. The gas drag force* $\boldsymbol{F_D}$ *acts on the attachment in the downstream direction, and the magnetic Lorentz force* $\boldsymbol{F_L}$ *acts on the attachment out of the current curvatures (in the radial direction of the curvatures). Grey optical filter 1000x, 12 slm of Ar,* $p = 101$ kPa *(adapted from [53])*

direction of the rotation of the anode represents no more than 2 % of the axial component. Fig. 5.12 shows the minor effect of the rotation of the anode on the bright plasma jet when viewed from above. At high arc currents ($I \geq 500$ A) the inclination of the bright plasma jet in the direction of the rotation of the anode is visible. The brightest part of the bright plasma jet above the anode is caused by the anode jet.

The greater $\boldsymbol{F_D}$ is, the faster the constricted attachment moves downstream. We can increase $\boldsymbol{F_D}$ and, consequently, the speed of the attachment by increasing the pressure gradient along the arc. This pressure gradient can be increased by lowering the ambient pressure (Fig. 5.13) or by increasing the electric power of the arc (Fig. 5.14, Fig. 5.15). The arc power increases with an increase in the arc current. $\boldsymbol{F_D}$ also increases as a result of the expansion of the plasma jet, because this expansion narrows the cold gas boundary layer between the anode and the bright plasma jet that decelerates the anode attachment. And the narrower this layer is, the less the attachment is decelerated by this layer. The plasma jet expands when the ambient pressure is reduced or when the arc current is increased.

We can also put the anode vertically closer to the exit nozzle to obtain faster movement of the attachment. This follows from the results in Fig. 5.13(a). After increasing y_{E} (C5 $\rightarrow$ C7 and C5 $\rightarrow$ C8), the average attachment speed decreased because the cold gas boundary layer between the anode and the bright plasma jet that decelerates the anode attachment became wider. In Fig. 5.13(a), this is shown only for $p = 80$ kPa, but it was also true for other values of the ambient pressure. $P = 50.6$ kW corresponded to $I = 254 \pm 4$ A, and the dependence for $I = 300$ A looks almost the same as that in Fig. 5.13(a). The same conclusion follows from the comparison of the graph "WORN; 12.5 slm" in Fig. 5.14(a) and the graph "WORN; 12.5 slm; C2" in Fig. 5.15. The first graph is for C1 ($y_{\mathrm{E}} = 0.9$ mm) and the second graph for C2 ($y_{\mathrm{E}} = 1.4$ mm).

The attachment speed also increases with decreases in the horizontal distance

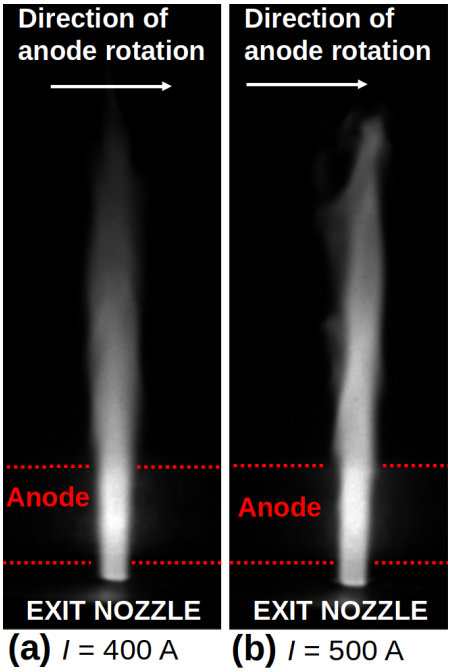

Figure 5.12: Two camera images of the bright plasma jet when viewed from above, obtained by the reflection of light on two mirrors. The anode was rotating to the right and is not visible in the images. Anode configuration C1, $D = 6$ mm, $Ar = 12$ slm, $p = 101$ kPa, exposure time of 0.29 µs

x from the exit nozzle. This is because the plasma flow speed decreases rapidly in the downstream direction (with increases in the x-coordinate) [36] as a result of the surrounding atmosphere. The relations in Fig. 5.13(b) for C6 revealed the same conclusion as those for C5, except that the decrease in the average attachment speed with the increase in ambient pressure was less rapid (it was in the range of 70-330 m/s even for $p = 75$-95 kPa) because of higher x_A in the case of C6.

To compare the attachment speed on the anode surface itself, the value of 14 mm was chosen, and the average attachment speed along the entire anode surface (0-20 mm ↔ "whole movement") was compared with that along the upstream part of the anode surface, from $x - x_A = 0$ mm to 14 mm ("0-14 mm"). As we can see in Fig. 5.13(a), at ambient pressures $p > 60$ kPa, the average speed along 0-14 mm of the anode surface was higher than that along 0-20 mm. It means that the anode arc attachment slows down a little during its movement downstream along the anode surface. The difference is not visible for $p < 60$ kPa, which indicates that for those lower ambient pressures, the attachment moves only within the upstream part of the anode, 14 mm long.

If we compare the movement of the attachment in a shorter upstream part of the anode surface, let us say 0-12 mm, with the whole movement of the attachment, the pressure boundary when the average attachment speed values start to differ will be less than 60 kPa. This is because both the average position on the anode where the attachment is created and the one where it decays shift downstream along the anode surface with an increase in the ambient pressure (Fig. 5.16).

The average position of the creation of the attachment shifts upstream with decreases in p because the anode jet causes an inclination of the bright plasma jet upward and because a reduction of p causes an expansion of the cold boundary layer between the anode and the bright plasma jet. Therefore, at low p the cold boundary layer is narrowest close to the exit nozzle, and the probability of an electrical breakdown is smallest close to the exit nozzle. The narrow boundary

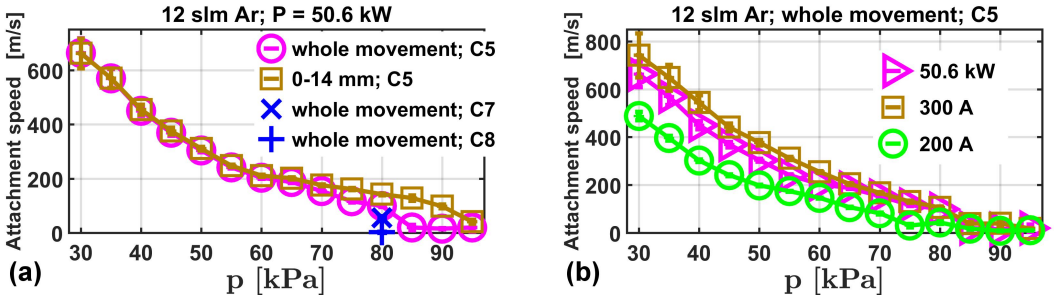

Figure 5.13: ***(a)*** *The ambient pressure dependence of the axial attachment speed averaged from the movement over the entire* 20 mm *long anode surface ("whole movement") and averaged from the movement only between* 0 mm *and* 14 mm *("0-14 mm") of the anode. The position of* 0 mm *represents the edge of the anode closer to the exit nozzle.* ***(b)*** *The ambient pressure dependence of the average axial attachment speed in C5 calculated from its entire movement for two constant arc current values and one constant arc power value (adopted from [56])*

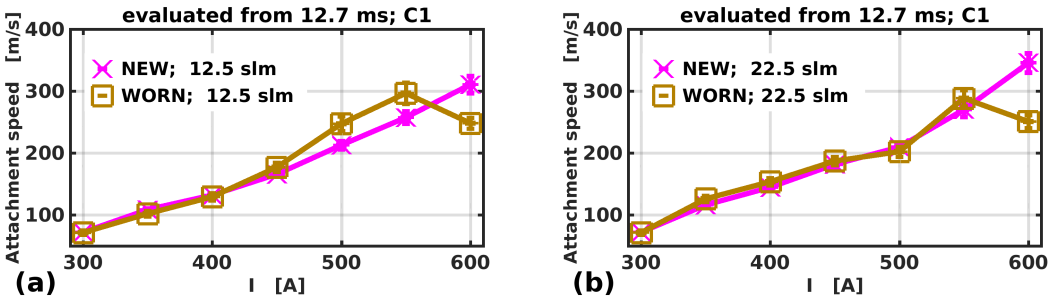

Figure 5.14: The arc current dependence of the axial attachment speed averaged within the time interval of 12.7 ms *in C1,* $p = 101$ kPa*, for a new anode ("NEW"), with a larger value at* $I = 600$ A*) and for a worn anode ("WORN");* ***(a)*** 12.5 slm *of Ar,* ***(b)*** 22.5 slm *of Ar (adopted from [53])*

layer also causes a short restrike period, that is to say, a short time between the creation of the attachment and the following decay of the attachment. Therefore, with decreases in p, the average position of the decay of the attachment also tends to move upstream, together with the average position of the creation of the attachment.

The decrease in the attachment speed with increases in the horizontal distance x is evident even in individual restrike periods; it is evident from the change in the slopes of the time dependence of the axial attachment position. For example, the slope of the graph in Fig. 4.4(a) between $t = 1.91$ ms and $t = 1.97$ ms is about 10 m/s lower than the slope of that graph between $t = 1.97$ ms and $t = 2.03$ ms.

In Fig. 5.13(a), the very low values of the average attachment speed for $p >$ 85 kPa in the graph "whole movement; C5" are the result of the attachment's dwelling on the end of the anode further from the exit nozzle (at $x = x_A$+20 mm). We can say that at $p > 85$ kPa the attachment would repeatedly like to move beyond the position $x = x_A + 20$ mm but it could not because it reached

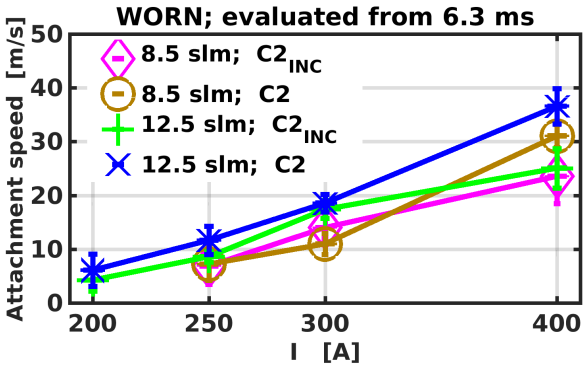

Figure 5.15: The arc current dependence of axial attachment speed averaged within the time interval of 6.3 ms *in* $C2_{\mathrm{INC}}$ *(*8.5 slm*: the lowest value at* 400 A*,* 12 slm*: the second lowest value at* 400 A*) and* $C2$ *(*8.5 slm*: the greatest value at* 400 A*,* 12 slm*: the second greatest value at* 400 A*). A worn anode was used,* $p = 101$ kPa *(adopted from [53])*

the end of the anode and therefore it rather moved a little along the vertical edge of the anode (at $x = x_{\mathrm{A}}+20$ mm), while a breakdown caused its decay.

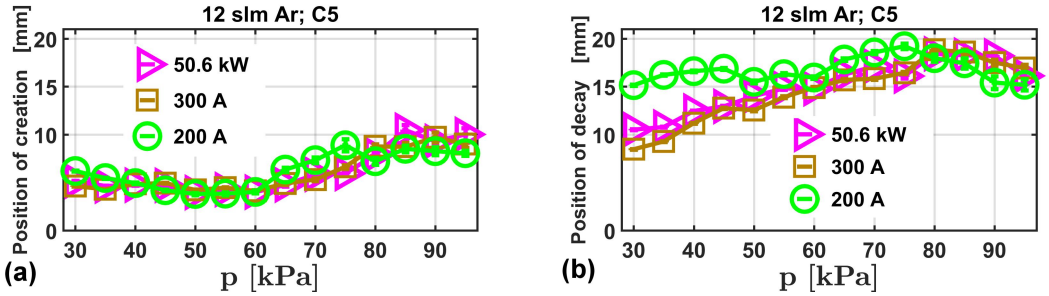

Figure 5.16: The ambient pressure dependence of the average axial position $x - x_{\mathrm{A}}$ *on the anode surface where* ***(a)*** *a new constricted attachment is created and* ***(b)*** *a previous attachment ceases to exist during a restrike.* $C5$*,* 12 slm *of Ar (adopted from [56])*

The average axial positions of the creation of the constricted attachment and its decay in Fig. 5.16 shift downstream in time, even when p and I are constant. The same is true for the average position of the diffuse anode arc attachment. This slow shift can be observed over a long time (a few hours) as an increase in the average arc voltage, because an increase in the long-term average arc voltage represents a downstream shift of the average location where the anode attachment moves along the anode or dwells on the anode (dwells in the case of a diffuse attachment). For $p = 80$ kPa and $p = 5$ kPa, we measured that the average arc voltage increased by 30 ± 4 V and 11 ± 4 V, respectively, over the course of four hours at $I = 250$ A.

Fig. 5.15 reveals that the inclination of the anode of about 10° (Fig. 5.11(b)) does not change the average attachment speed along the anode significantly, at least not for $p = 101$ kPa, $I \leq 400$ A and argon flow rates less than or equal to 12 slm. However, greater inclination could slow the attachment down significantly for at least two reasons. First, near the anode the projection of the magnitude of

the drag force $\boldsymbol{F_D}$ on the anode surface (the projection of $\boldsymbol{F_D}$ on the attachment movement direction) decreases with increases in the inclination angle. Second, the lower curvature of the attachment, near the anode surface, together with the $\boldsymbol{F_L}$ acting upstream (according to [15,19]), increases with increases in the inclination angle. Therefore the net force acting on the attachment in the downstream direction should decrease with increases in the inclination angle.

When $I \geq 400$ A, an inclination angle of 10° caused the attachment to dwell for a long time on the downstream edge of the anode, farther from the exit nozzle. Therefore, in Fig. 5.15, there are no data for $I > 400$ A. When $I \leq 200$ A, the restrike mode was changing to a steady mode as a result of a small net force acting on the attachment in the downstream direction and, therefore, in Fig. 5.15, there are no data for 8.5 slm of Ar and $I = 200$ A.

The effect of the argon flow rate and of the state of the anode surface ("NEW" vs "WORN" anode surface) on the average axial attachment speed is not significant (Fig. 5.14). The low dependence of the average attachment speed on the argon flow rate Ar has at least two reasons: first, the magnetic Lorentz force $\boldsymbol{F_L}$ acting downstream in the upper curvature of the attachment does not depend on Ar [15], and second, the plasma flow speed (directly proportional to $\boldsymbol{F_D}$) does not depend significantly on Ar [9]. However, from our measurements it is evident that the average attachment speed nevertheless increases somewhat with increases in the argon flow rate.

We fitted various relations of the measured average axial attachment speed, generalized them, and found that the measured magnitude of the average axial speed of the constricted attachment during the restrike can be expressed as the following function of the magnitudes of ambient pressure p, arc voltage I, argon flow rate Ar, exit nozzle diameter D, and the distance between the exit nozzle and anode x_A:

$$\bar{v}_{\mathrm{attachment,x}}[\mathrm{m/s}] = 2(D[\mathrm{mm}])^2 - \frac{I}{2} + \frac{20(x_\mathrm{A}[\mathrm{mm}])^{1/4}}{(D[\mathrm{mm}])^5}\frac{(I[\mathrm{A}])^2(Ar[\mathrm{slm}])^{3/2}}{p[\mathrm{kPa}]}, \quad (5.1)$$

where for example D[mm] means the magnitude of D in mm (without the unit), p = 30-101 kPa, I = 150-600 A, Ar = 12-32 slm, D = 5 or 6 mm, x_A = 1.4, 3.4, or 3.8 mm. This equation, therefore, applies only to the magnitudes of the corresponding physical quantities.

For that fitting purpose, the average attachment speed was computed along the 17.5 mm long upstream part of the anode surface, from $x - x_\mathrm{A} = 0$ mm to 17.5 mm. This part of the anode surface was chosen to avoid the possible lessening of the average speed value by the attachment's dwelling on the downstream edge of the anode (it happened at high I, p, Ar, and anode surface inclination degrees, or small distances x_A). The accuracy with which function (5.1) fits the data is shown in Fig. 5.17, Fig. 5.18, and Fig. 5.19. The fitting function is represented by the blue dashed line.

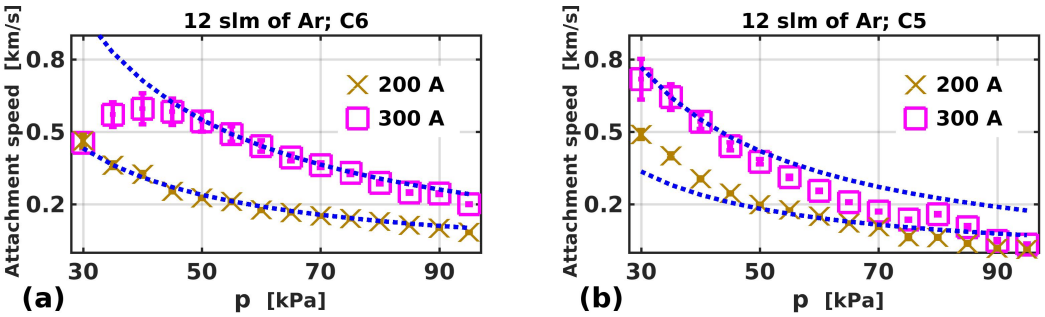

Figure 5.17: The ambient pressure dependence of the average axial attachment speed (data points) vs. the fitting function (blue dashed line) ***(a)*** *for C6 and* ***(b)*** *C5. D= 5 mm*

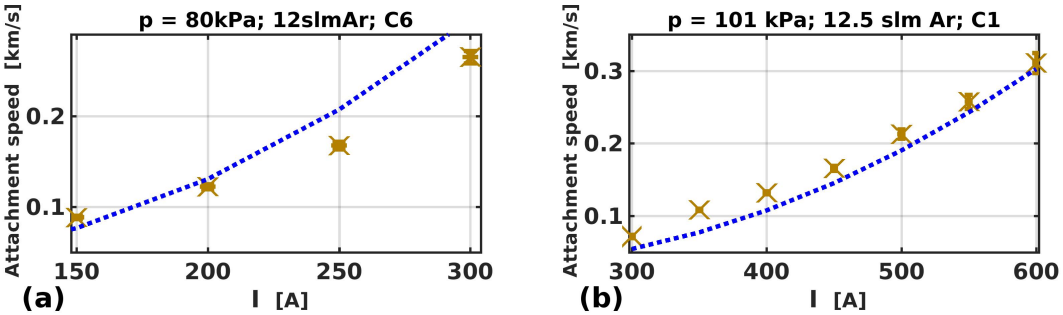

Figure 5.18: The arc current dependence of the average axial attachment speed (data points) vs. the fitting function (blue dashed line) ***(a)*** *for C6, p = 80 kPa, D= 5 mm and* ***(b)*** *for C1, p = 101 kPa, D= 6 mm*

We also found the following function for the average axial plasma speed above the anode, which fits previously measured values of the plasma flow speed [8, 54, 61]:

$$\bar{v}_{\mathrm{plasma,x}}[\mathrm{m/s}] = 1000 + I[\mathrm{A}] + 8\bar{v}_{\mathrm{attachment}}[\mathrm{m/s}], \tag{5.2}$$

where again, as in the case of equation (5.1), for example I[A] means the magnitude of I in A (without the unit), p = 30-101 kPa, I = 200-400 A, Ar = 12-22 slm, D = 5 or 6 mm, x_{A} = 3.4 or 3.8 mm.

The accuracy with which function (5.2) fits the data is shown in Fig. 5.21 and Fig. 5.20. The fitting function is represented by the red dashed line.

The values of all five variables, p, I, Ar, D, and x_{A}, are set before the experiment by an experimenter. Therefore, if the second function (equation 5.2) for $\bar{v}_{\mathrm{plasma,x}}$ is satisfactorily true, we do not have to measure the axial plasma speed above the anode because we can just calculate it from the much more easily and much more precisely measured average axial attachment speed. If the first function (equation 5.1) for $\bar{v}_{\mathrm{attachment,x}}$ is also satisfactorily true, we do not have to measure even the average axial attachment speed because, in such a case, we just need to calculate both average speeds from the five preset working conditions of the plasma torch. However, we think the two functions apply only to the limited range of the values of p, I, Ar, D, and x_{A}, that was used, and that they are not

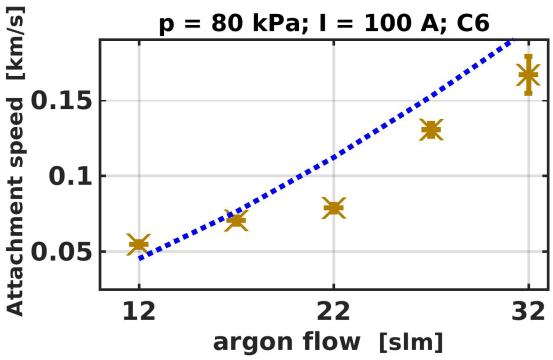

Figure 5.19: The argon flow dependence of the average axial attachment speed (data points) vs. the fitting function (blue dashed line) for C6, at p = 80 kPa, D= 5 mm

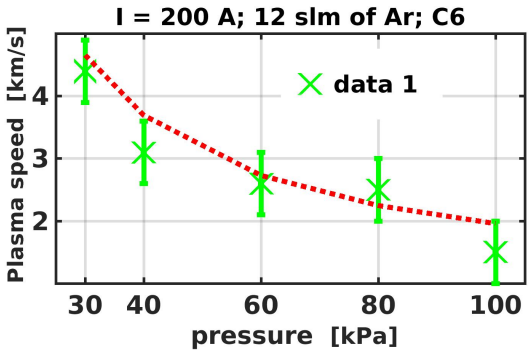

Figure 5.20: The ambient pressure dependence of the average axial plasma speed above the anode (data points) vs. the fitting function (red dashed line). D= 5 mm, C6. "Data 1" are from [61]

in their final state yet, that is to say, they are not satisfactorily true yet. The two functions need to be further compared with more (future) measured data and improved if necessary. This opinion follows from the way we obtained them. At first, from our graphs with the average axial anode arc attachment speed, we noticed that the average axial attachment speed depends quadratically on the arc current and hyperbolically on the ambient pressure. Then we tried different coefficients for the quadratic and the hyperbolic term, different exponents for Ar, D, and x_{A}, and different additional terms to fit the function $\bar{v}_{\mathrm{attachment,x}}$ with the data as well as possible while keeping all coefficients as integers. In equation (5.1), the most questionable is the dependence of $\bar{v}_{\mathrm{attachment,x}}$ on D and x_{A}.

Regarding the time characteristics of the axial movement of the constricted attachment, the restrike period (the average time between two consecutive restrikes) was investigated. With decreases in the ambient pressure (Fig. 5.22(a)) or with increases in the arc current (Fig. 5.22(a),(b)), the average period of the restrike process decreases. It does not depend significantly on the argon flow (Fig. 5.22(b)). One reason is the expansion of the plasma jet and the subsequent reduction in the thickness of the cold gas boundary layer between the anode and the bright plasma jet with decreases in p or with increases in I. The reduction in the boundary layer thickness leads to a reduction in the breakdown threshold voltage and therefore increases the likelihood of a restrike. Another reason is that an increase in the attachment speed decreases the restrike period because the distance traveled by the attachment does not depend significantly on p or I. The distance traveled by the attachment is, with uncertainty, equal to the difference between the average attachment creation position and the average attachment decay position (Fig. 5.16).

Except for the graph "12.5 slm; C1; pos(t); 12.7 ms", the restrike period in Fig. 5.22(b) was computed from the arc voltage waveform. We can see that the

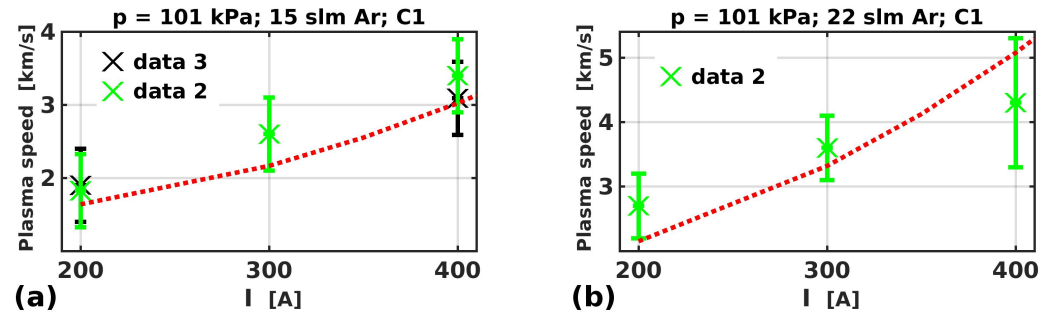

Figure 5.21: The arc current dependence of the average axial plasma speed above the anode (data points) vs. the fitting function (red dashed line) ***(a)*** *for* 15 slm *of Ar and* ***(b)*** *for* 22 slm *of Ar. D*= 6 mm*, C1. "Data 3" are from [54] and "Data 2" are from [8]*

results in the graph "12.5 slm; C1", obtained from the arc voltage waveform, are, within the uncertainty, the same as those in the graph "12.5 slm; C1; pos(t); 12.7 ms", obtained from the time dependence of the attachment position. Therefore, we can compute the restrike period from the attachment position time dependence as well as from the arc voltage waveform.

The very long restrike periods at high ambient pressures were a result of the attaching/dwelling of the constricted anode attachment on the downstream edge of the anode, where it tried to move down along the vertical downstream surface of the anode. For "200 A; C5" and "300 A; C5", for p > 70 kPa and p > 80 kPa, respectively, the restrike periods were approximately 1 ms and 0.5 ms, respectively.

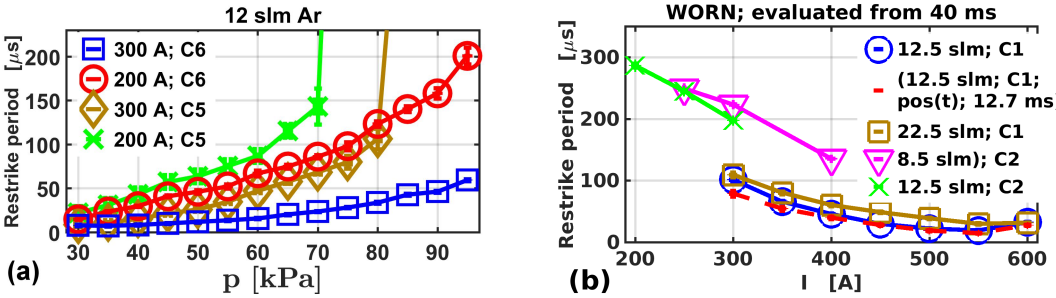

Figure 5.22: ***(a)*** *The ambient pressure dependence of the average restrike period computed from* 100 ms *of the attachment position time dependence. The values of "300 A; C5" increased to approximately* 0.5 ms*, and the values of "200 A; C5" increased to approximately* 1 ms *at p > 80 kPa and p > 70 kPa, respectively (adapted from [56]).* ***(b)*** *The arc current dependence of the average restrike period computed from the arc voltage waveform. A worn anode was used. In one case ("12.5 slm; C1; pos(t); 12.7 ms") it was computed from* 12.7 ms *of the attachment position time dependence (adopted from [53])*

5.4 Anode erosion phenomena

The anode erosion happens mainly under the anode arc attachment. Color Fig. 5.23(a) proves this because the green fumes under the remains of a former attachment (that drifted in the direction of the anode rotation $\boldsymbol{x} \times \boldsymbol{y}$) indicate copper fumes from the copper anode. Fig. 5.23(a) also shows a double anode arc attachment, that is to say, two anode arc attachments at the same time. These two attachments are not a transition from a former to a new anode attachment that is visible in the high-speed camera images with an exposure time of about 0.29 µs. The duration of a typical restrike (transition from a former to a new anode attachment) is about 2-4 µs and the exposure time of the camera image in Fig. 5.23(a) was in the range of ms because it was taken with the Canon EOS 450D camera.

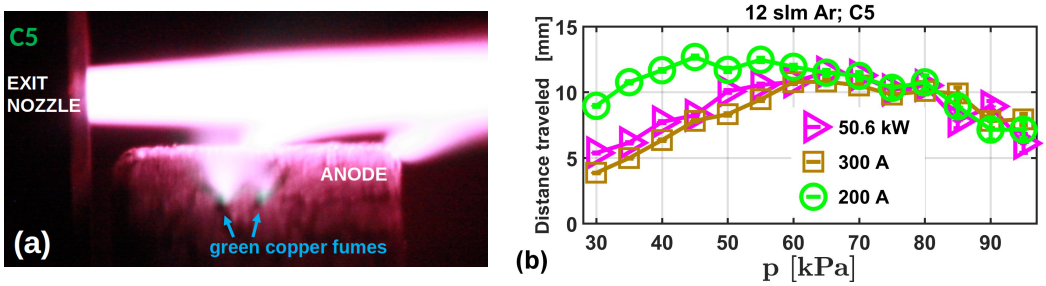

Figure 5.23: ***(a)*** *A camera (Canon EOS 450D) image of the anode area in C5, with two green copper fumes under the remains of a former attachment drifting in the direction of the anode rotation. Gray optical filter 1000x, I = 200 A, p = 80 kPa, 22 slm of Ar.* ***(b)*** *The pressure dependence of the average axial component of the distance traveled by the constricted anode attachment along the anode surface. The average values were computed from the time interval of* 100 ms *(adopted from [56])*

The axial component of the average distance traveled by the attachment along the anode surface (Fig. 5.23(b)) determines how wide the part of the anode surface that is eroded by the attachment is. The part of the anode that, under given working conditions, is not touched by the constricted attachment erodes much less than that where the anode attachment moves. The axial component of the average distance traveled by the attachment along the anode is within the uncertainty equal to the difference between the average attachment decay position and the average attachment creation position (Fig. 5.16).

It seems that the average distance traveled by the attachment decreases with increases in the arc current (Fig. 5.24) and depends significantly on the actual state of the anode surface. In Fig. 5.24, "NEW", "WORN", and "WORN2" represent a new anode, an anode with an eroded/worn surface, and another anode with a differently eroded/worn surface. When we changed the investigated time interval from 9.5 ms to 12.7 ms (for the "WORN2" data, only 9.5 ms of high-speed camera video footage was available), the shape of the "NEW", "WORN", and "WORN2" graphs in Fig. 5.24 did not change; only the absolute values changed by less than about 0.5 mm.

The slight decrease in the average distance traveled by the attachment along the anode with increases in the arc current means that a greater electric power is transferred into an even smaller part of the anode and that the anode erosion increases with increases in the arc power, as Szente *et al.* [34] found for tip electrodes.

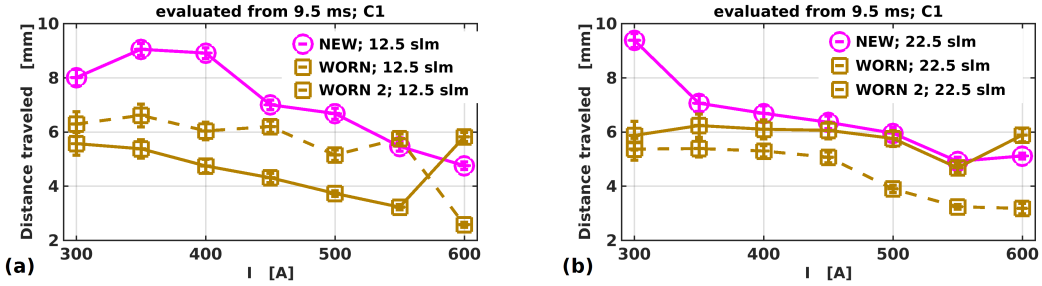

Figure 5.24: The arc current dependence of the average axial component of the distance traveled by the constricted anode attachment along the anode surface, computed from a time interval of 9.5 ms. *"NEW", "WORN", and "WORN2" mean a new anode, worn anode, and another worn anode, respectively.* $p =$ 101 kPa, *the argon flow rate was* ***(a)*** 12.5 slm *or* ***(b)*** 22.5 slm *(adopted from [53])*

An eroded anode surface has typical channels formed by craters when operating with a constricted anode arc attachment (Fig. 5.25(c)). This fact, together with the fact that the anode rotates, indicates that the constricted anode attachment moves along those channels and during the restrike, a new attachment is created not in a random place but in a channel that is adjacent to the previous one.

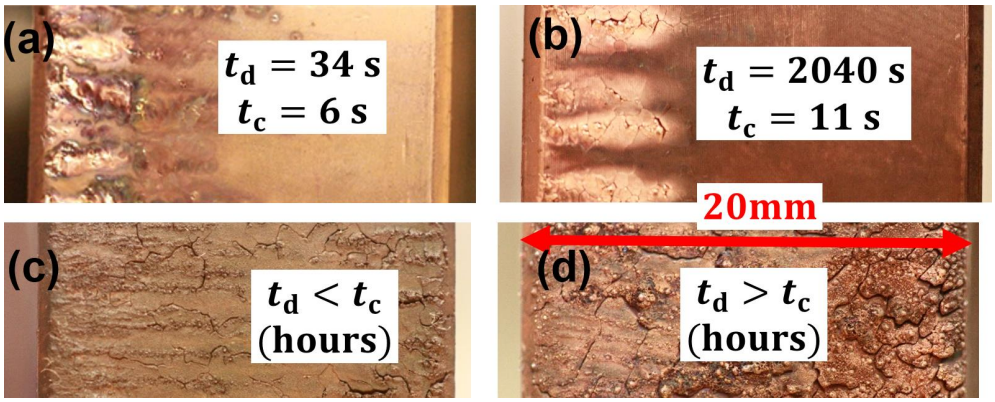

Figure 5.25: A detailed view of the anode surfaces ***(a)***, ***(b)*** *after a short time, and* ***(c)***, ***(d)*** *after a long time (hours). The anode was used for a total time of* $t_d + t_c$, *where* t_c *indicates the time when the anode arc attachment was constricted, and* t_d *indicates the time when the anode arc attachment was diffuse (adopted from [56])*

A crater (Fig. 4.5(a),(c)) on the anode surface is created by rapid evaporation of the anode material (usually a copper) when the constricted anode attachment suddenly slows down. The position where the attachment suddenly slows down could be an inhomogeneity of the anode surface with sharp edges and/or maybe

places with a higher local electrical conductivity of the anode material. In the case of a worn anode surface, the position where the attachment suddenly slows down is probably a crater created previously. The often sudden slowing down of the constricted attachment is visible in high-speed camera video footage, and it is accompanied by falling of the attachment slope (with respect to the anode surface), that is to say, by decreasing of its inclination.

This fact suggests the possibility that the attachment may also suddenly slow down because of a sudden decrease in the instantaneous plasma flow speed as a result of, for example, turbulence in the water vortex [68] or turbulence in the ambient pressure. Those intermittent and sudden decreases in the instantaneous speed of the attachment are called the dwellings of the attachment.

On a new anode surface, the frequency of the attachment dwelling is in the order of hundreds of Hz, which is in the same order as the frequency of the fluctuations induced by the rotation of water in the chamber of the plasma torch [68]. The frequency of the attachment dwelling on a worn anode surface is about ten times higher than that on a new anode surface, so in this case reasons other than those connected with the torch chamber must play a role, for example, inhomogeneities of the anode surface or previously created craters.

When the constricted attachment dwells, its width (which is usually about 1 mm in the x direction) increases. This is probably because of the increase in the amount of evaporated anode material under the attachment during the dwelling. After a dwelling, the slope of the attachment rises again, and the attachment accelerates and moves downstream again. Because of this dwelling, in the rares case of multiple anode arc attachments, the individual attachments sometimes interact with each other as one overtakes another. We observed the interaction of the attachments in the high-speed camera video footage.

Individual craters are only visible on an anode surface that has not been used for very a long time (Fig. 4.5(a)); later, the craters overlap with each other and are no longer visible as individual craters (Fig. 4.5(b)). However, we can still see channels created from the overlapping craters when we use mostly a constricted anode attachment. The channels are smoothed out by a diffuse anode arc attachment (Fig. 5.25(a) $\rightarrow$ Fig. 5.25(b)). Fig. 5.25(a),(b) show the surface of one anode, Fig. 5.25(c) shows the surface of a second anode and Fig. 5.25(d) shows the surface of a third anode.

It was not possible to investigate the anode surface after using only a diffuse attachment ($t_c = 0$ s) because, within the first few seconds of the operation of the plasma torch, the attachment is always constricted. This is because the plasma torch WSP®-HR inside the low-pressure chamber/reactor must be switched on at approximately $p \geq 70$ kPa (because the water in the stabilizing water vortex is sucked by using pressure of about 50 kPa). This means that it is not possible to switch on the hybrid plasma torch at such a low ambient pressure that the attachment would be diffuse from the very beginning. After a long time, the diffuse anode attachment creates cracks on the anode surface that are, however, usually smaller than those in Fig. 5.25(d).

In the case of the anode erosion shown in Fig. 5.25, the rotational frequency

Figure 5.26: Image of the 20 cm *wide anode surface after* 4 s *of operation of the plasma torch when the anode was not rotating. The anode was only cooled down by an internal water circuit.* $p = 80$ kPa, $I = 200$ A, $Ar = 12$ slm

of the anode had a standard value of 28 ± 2 Hz. At this value of the rotational frequency of the anode, the anode erosion is not directly measurable because the anode loses only a small amount of weight in comparison to its total weight. If we want to directly measure the anode weight loss resulting from its erosion with a common balance scale (which has a limited accuracy), we must increase the ratio of the anode weight loss to the total mass of the anode.

Using a balance scale that is much more accurate (and expensive) than our AQ Sartorius E 2000 D balance scale would not necessarily solve the problem, because before the anode weight loss measurements, it is necessary to remove residues of water and deposits from the internal channels of the anode (where the cooling water is circulating during the operation of the plasma torch). It is not possible to remove these residues totally, and thus the measured anode weight loss must be greater than the mass of the residues that were not removed from the inside of the anode. The WSP®-H 2011 has a very large and massive anode (Table 3.1); therefore, the ratio that is mentioned is too small in its case. In the case of the WSP®-HR, which has a smaller anode, the ratio of the anode weight loss to the total mass of the anode is greater but still not great enough.

Therefore we came up with the idea of reducing the rotational frequency of the anode of the WSP®-HR from 28 Hz to 15 Hz to increase the anode erosion proportionally. For practical purposes, we want to know the anode erosion at the standard value of 28 Hz, but, provided that the decrease of the rotational frequency of the anode increases the anode erosion proportionally, we can at least compare the anode erosion under different working conditions in this way. With a rotational frequency smaller than 15 Hz, there is a risk that the anode will stop during the operation of the plasma torch as a result of friction forces. What happened when the anode was not rotating during the operation of the torch can be seen in Fig. 5.26.

The measured anode weight loss is summarized in Table 5.3. We used an anode 20 cm wide with its total mass in the range of 683-685 g (depending on the eroded state). From a similar measurement with a bigger WSP®-H 2011 torch anode, it only followed that after one hour of the operation of the plasma torch (at $I = 600$ A, $p = 101$ kPa, anode rotational frequency of 47 ± 1 Hz), the anode weight loss was less than 1 g. The total mass of this bigger anode was between 2.5 and 3.5 kg.

Let us go back to the diffuse anode arc attachment at atmospheric pressure (Fig. 5.10(b)). The erosion of the anode surface and the exit nozzle by using

p [± 0.5 kPa]	Average el. power [± 0.5 kW]	Type of attachment	Anode rotational frequency [± 2 Hz]	Anode weight loss [± 0.02 g]
80	50.6	constricted	15	1.03
45	50.6	constricted	15	0.09
2	50.3	diffuse	15	0.11

Table 5.3: Anode weight loss after four hours (± 20 s) of operation of the WSP®-HR. The total mass of the anode was in the range of 683-685 g. Ar = 12 slm*, C5 (adopted from [56])*

that diffuse attachment can be seen in Fig. 5.27. The anode erosion could not be measured quantitatively in that case because of the large and massive anode. Regarding the weight loss of the whole exit nozzle, its quantitative measurement is not important as only the gap of the exit nozzle plays a significant role in the operation of the plasma torch, not its edges. After exposure to that diffuse attachment only the edge of the anode closer to the exit nozzle (in Fig. 5.27, it is the right edge) seems to be more eroded than it is in the case of usual constricted attachment. The total anode erosion, however, seems to be lower in the case of that diffuse attachment than in the case of a constricted attachment.

The exit nozzle is more damaged in the case of the diffuse attachment. The almost horizontal groove in the left part of the exit nozzle (in the third column of Fig. 5.27) was caused by a temporary attachment of the arc to the nozzle. The arc became attached to the nozzle for a while because the nozzle was very close to the anode. The damage to the exit nozzle in the case of that diffuse attachment could be resolved by cooling down the inside of the exit nozzle in a similar way to how it is done in the case of the anode. Then, maybe, at atmospheric ambient pressure, it would be beneficial to use the diffuse anode arc attachment rather than the conventional constricted anode arc attachment. The main advantages would be less anode erosion and a more stable plasma jet.

We found that the anode erosion can be compared under different working conditions, not only after operation of the plasma torch with very low anode rotational frequency by weighting the anode but even during the operationof the plasma torch. It can also be compared in the case of the WSP®-H 2011, with a very large and massive anode. This is because the variable called the proportion of all (the attachment's) dwellings (described in Section 4.3) is proportional to the measured anode weight loss (Fig. 5.28, Table 5.3). They are proportional, however, only under the assumption, even quite expected, that the measured ratio 1.03 g/0.11 g (Fig. 5.28(a), Table 5.3) remains greater than one also in the case that the rotational frequency of the anode equals 28 Hz.

The finding that the proportion of all the attachment's dwellings is proportional to the measured anode weight loss means that the more often a constricted anode attachment dwells on the anode, the more the anode is eroded. The anode erosion is therefore influenced by the movement of the constricted anode arc attachment, and, together with the proportion of all dwellings, decreases with decreases in the ambient pressure.

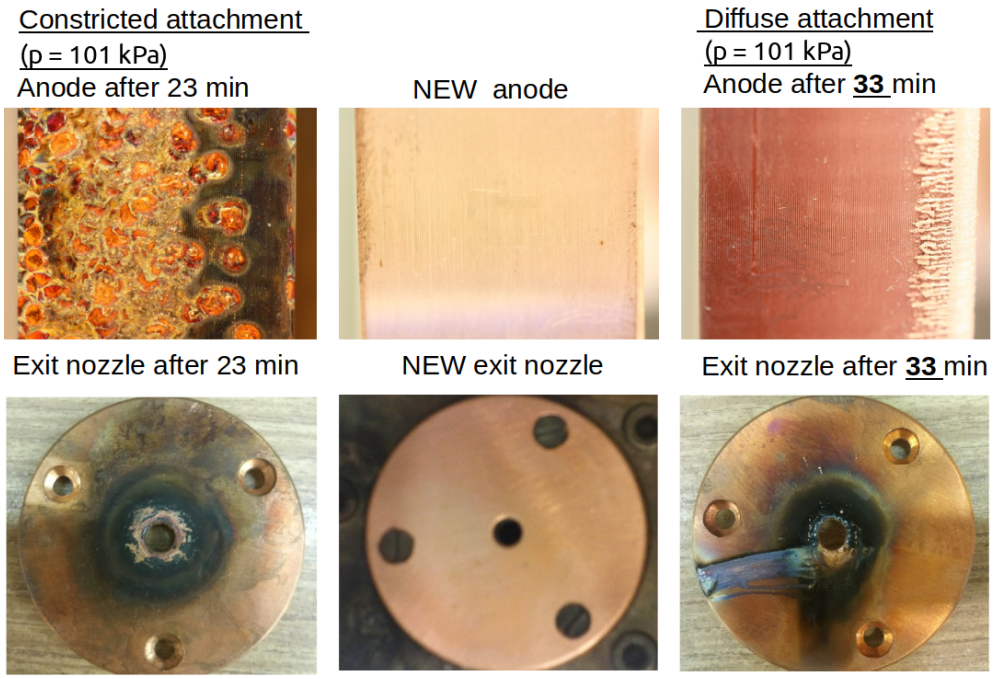

Figure 5.27: Images of the 16 cm *wide anode surface and the exit nozzle used at* $p = 101$ kPa. *The three states of the anode surface and exit nozzle are compared: after operation of the torch with a constricted anode attachment (left column), new ones (middle column), and after operation of the torch with a diffuse anode attachment (right column)*

The anode erosion is less extensive when a diffuse attachment is present (Table 5.3, $p = 2$ kPa) as opposed to a constricted attachment (Table 5.3, $p = 80$ kPa). However, when the constricted attachment is almost diffuse (Table 5.3, $p = 45$ kPa), the corresponding anode erosion is almost the same as in the case of a diffuse attachment. A diffuse anode attachment erodes the anode less than a constricted anode attachment, not only in the case of the hybrid plasma torch but also in the case of a double anode plasma torch [69].

This is probably because the heat transfer from the plasma jet to the anode is spread out less in a constricted anode attachment than in a diffuse anode attachment. This is in agreement with Terasaki *et al.* [70] who reported that the melting of the anode in a free-burning arc is determined by the heat input density rather than the total heat input.

The chronology of the measurements in all the graphs in Fig. 5.28 was from right to left, that is to say from higher p to lower p. Each point in the graphs was measured for the time interval of 0.1 s, and the time between the measurements at $p = 95$ kPa and $p = 30$ kPa was about 2.0 hours. There is a significant increase in the frequency of the attachment's dwelling with the vertical shift of the anode farther from the exit nozzle (C7 and C8 in comparison with C5 in Fig. 5.28). Therefore, anode configurations with a long distance y_E, like C7 and C8, are not suitable for hybrid plasma torch operation because of great anode erosion. The proportion of all dwellings for $t > \tau = 10$ µs is only a little greater than that for $t > \tau = 15$ µs.

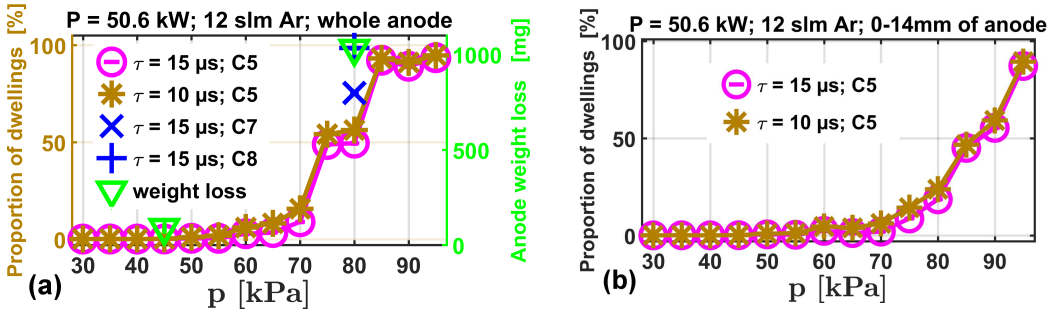

Figure 5.28: The ambient pressure dependence of the proportion of all the attachment's dwellings within the length of 1 mm *on the anode surface and for a time interval longer than* 10 μs *or* 15 μs. *The comparison is made for the attachment's movement* ***(a)*** *along the whole anode surface (0-20 mm) or* ***(b)*** *between 0 mm and 14 mm of the anode surface. Anode weight loss was measured at the lower anode rotational frequency of 15 Hz (adapted from [56])*

Popov *et al.* [71] reported that the anode evaporation must be high if the anode jet is very bright. In the case of the hybrid plasma torch, the anode jet is very bright at high p and high I, which agrees with the high anode erosion (and proportion of all dwellings) at $p > 70$ kPa (Fig. 5.28(a)).

The big difference between the proportion of all dwellings in Fig. 5.28(a) (0-20 mm of the anode surface) and Fig. 5.28(b) (0-14 mm of the anode surface) at $p > 70$ kPa means that at $p > 70$ kPa, in C5, the anode attachment dwells between 14 and 20 mm of the anode surface for a long time. According to the corresponding video footage, at $p > 80$ kPa it dwelled mostly on the downstream edge of the anode surface. For $p \leq 70$ kPa, the proportion of all dwellings in C5 seems to be almost the same in both Fig. 5.28 (a) and Fig. 5.28(b).

It means that at $p \leq 70$ kPa, $P = 50.6$ kW, $Ar = 12$ slm, the attachment almost did not dwell between 14 and 20 mm of the anode surface and dwelled almost solely between 0 and 14 mm of the anode surface. The dwelling of the attachment happens wherever the attachment moves, so if the attachment almost did not dwell between 14 and 20 mm of the anode surface it means that the attachment almost did not move between 14 and 20 mm of the anode surface. This is in agreement with the results in Fig. 5.16.

The attachment dwelled for a long time on the downstream edge of the worn anode (and moved down along the vertical surface) also at $I = 600$ A and $p = 101$ kPa, which caused the sudden lowering of the average attachment speed on the worn anode in Fig. 5.14 and the longer average restrike period in Fig. 5.22(b). It also caused the suddenly longer average distance traveled by the attachment in Fig. 5.24, in the case of one worn anode. During the dwelling of the constricted attachment on the downstream edge of the anode, the upper part of the attachment was sometimes carried farther in the downstream direction by the main plasma flow to such an extent that the bright part of the attachment was torn apart, and only then was a new attachment created closer to the exit nozzle.

Our MATLAB script sometimes evaluated the carrying of the upper part of the constricted attachment on the downstream edge of the anode as the contin-

uous movement of the attachment. This is also why in Fig. 5.24, in the case of one worn anode at $I = 600$ A, the average distance traveled by the constricted attachment was too large in comparison with a value expected from the slope of the graph. The above-mentioned results, for $I = 600$ A and $p = 101$ kPa, therefore, require modification.

The proportion of all dwellings is greater on a worn anode than on a new anode, as shown in Fig. 5.29. This is probably because a worn anode surface has more inhomogeneities and craters that force the constricted attachment to stop than a new anode surface has. In the parentheses in the legends in Fig. 5.29, there are values of the τ and l from equation (4.6) respectively.

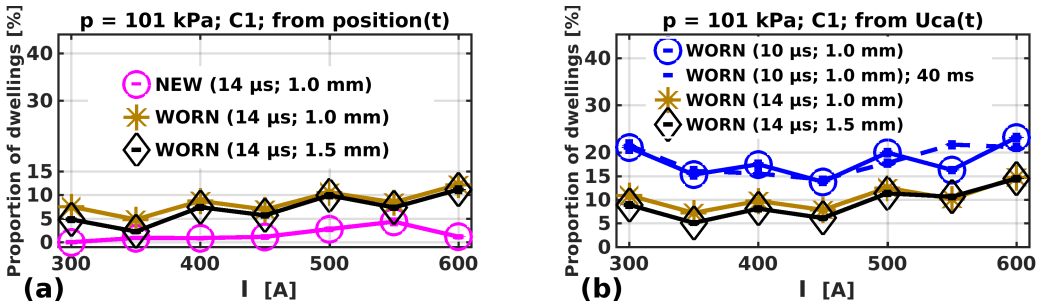

Figure 5.29: The arc current dependence of the proportion of all the attachment's dwellings. The dwellings were computed from 12.6 ms (in one case 40 ms - the dashed line) of the ***(a)*** *attachment's position time dependence and of the* ***(b)*** *arc voltage waveform. The two values in parentheses in the legends are the values of τ and l from equation (4.6) respectively (adapted from [53])*

Fig. 5.29 further shows that the dwelling on the worn anode surface within the length of 1.5 mm was a little less frequent than the dwelling within the length of 1.0 mm. Therefore, if we neglect a small change in the anode surface between the data measurements in the two graphs, we can say that the number of craters with a length of 1.5 mm made by the attachment is lower than the number of craters with a length of 1.0 mm. Each data point in the graphs in Fig. 5.29 represents one measurement (with a duration of 12.6 ms or 40 ms), and the chronology of those measurements was from a lower arc current to a higher arc current. The measurements in each graph lasted about 10 min in total; therefore, the time that elapsed between two consecutive measurements was about 1-2 min. This time of 1-2 min was needed to stabilize the working conditions.

The increase in the proportion of all dwellings with an increase in the arc current, in the case of the new anode surface (Fig. 5.29(a), except the value at $I = 600$ A), may be the result of the chronology of the measurements, because the new anode was monotonically eroded more and more over time. The surface of the worn anode changed obviously in a more complicated way than the surface of the new one.

By comparing the graphs "WORN (14 µs; 1.0 mm)" and the graphs "WORN (14 µs; 1.5 mm)" in Fig. 5.29(a) and Fig. 5.29(b), we can see that the proportion of all dwellings computed from the axial attachment's position time dependence ("position(t)") gives almost the same results as that computed from the arc voltage waveform ("$U_{ca}(t)$"). The graphs "WORN (10 µs; 1.0 mm)" and "WORN

(10 μs; 1.0 mm); 40 ms" compare the effect of statistics on the values of the proportion of all dwellings. The first graph was computed from an arc voltage waveform 12.6 ms long, and the second one from an arc voltage waveform 40 ms long.

Regarding the arc mode, it is obvious that the steady mode causes the greatest anode erosion. This is because, in this case, a small part of the anode under the anode attachment receives such much thermal energy per unit time from the arc that the cooling of the anode at that position is not sufficient. In contrast, when the attachment moves along the anode continuously, the cooling of the anode is used effectively. This is in agreement with Wutzke *et al.* [16], who reported that the restrike mode might "lead to a considerable lessening of the specific time-averaged heat flux to the anode".

5.5 Electric probe measurements

The electric probes were used under different working conditions and in different positions summarized in Table 5.4.

Figure	Anode conf.	Ar [slm]	I [A]	p [kPa]	Positions of the probes [mm; mm]
Fig. 5.30	C6	12	75	20, 40	[14.8; 4.3], [12.2; 4.0]
Fig. 5.31	C6	12	75	20	[11.2; 3.8]
Fig. 5.32(b)	C6	12	70	20	[4.0; 4.0]
Fig. 5.34	C6	12	75	40	[11.2; 3.9] + [12.9; 3.8]
Fig. 5.35	C5	22	171	62	[22.3; 9.5]+[24.0; 9.5], [18.8; 16.5]+[20.4; 16.5]
Fig. 5.37	C6	12	75	1	[3.2; 3.8] + [4.9; 3.8], [23.5; 4.4]+[25.2; 4.4]
Fig. 5.38	C6	12	75	1	[4.1; 0.9] + [5.7; 0.9], [7.6; 0.9]+[9.2; 0.9]
Fig. 5.39(a)	C6	12	75	40	[11.2; 3.9] + [12.9; 3.8]
Fig. 5.39(b)	C6	12	75	20	[11.1; 4.0] + [12.8; 3.9]

Table 5.4: Working conditions for the electric probe measurements (the positions [x; y] correspond to the coordinate system in Fig. 3.5) (adapted from [56])

The current-voltage characteristic of one probe in two positions at $p = 20$ kPa is shown in Fig. 5.30(a). Every value in the two graphs is an average value computed from one movement of one probe through the whole plasma jet (in the radial direction $\boldsymbol{x} \times \boldsymbol{y}$ or $\boldsymbol{y} \times \boldsymbol{x}$). In this case, the probe that was used was the part of the electrical circuit shown in Fig. 5.30(b). During the measurement of the probe $I - \Phi$ characteristic, the PicoScope measured two electric potentials (with respect to the anode ground): Φ_1 and Φ_2. The first one was equal to the probe potential $\Phi_{\text{probe}} = \Phi_1$, and the second one was used to calculate the probe current $I_{\text{probe}} = \Phi_2/1.0\ \Omega$.

A capacitor battery with a capacitance of 3.3 mF was charged by two DC voltage sources connected in series (one was not enough for such high bias voltages), with a constant overall voltage U, before each movement of the probe through the plasma. The capacitor battery was needed because the voltage sources that were used were not able to maintain their overall voltage sufficiently during the probe's movements through the plasma.

At $p = 40$ kPa and $\Phi_{\mathrm{probe}} > 100$ V, the volume of the probe pin was significantly reduced by high energetic electrons and negative ions; therefore, the corresponding measured probe $I - \Phi$ characteristic, at $p = 40$ kPa, is not shown here.

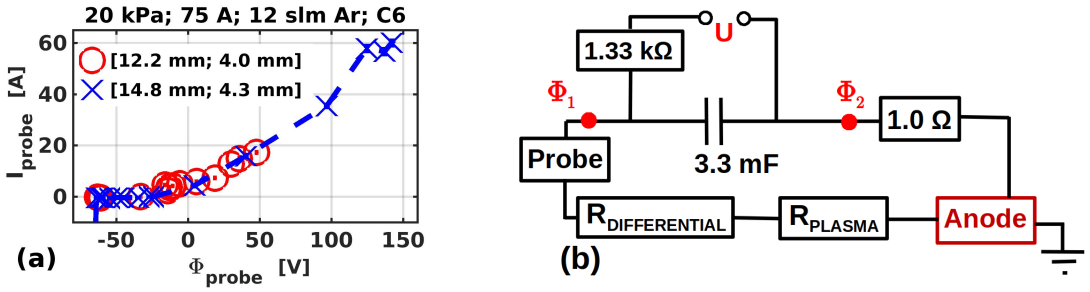

Figure 5.30: ***(a)*** *The $I - \Phi$ characteristic of the probe measured in two different positions of the anode area. The dashed line represents what is called piecewise linear interpolation in the MATLAB program, for the characteristic measured in the position [x; y] = [14.8 mm; 4.3 mm].* ***(b)*** *Electrical circuit for measurement of the probe $I - \Phi$ characteristic*

The differential resistance $R_{\mathrm{differential}} = \mathrm{d}\Phi_{\mathrm{probe}}/\mathrm{d}I_{\mathrm{probe}}$ of the probe $I - \Phi$ characteristic close to the floating potential ($\Phi_{\mathrm{probe}} \to \Phi_{\mathrm{f}}$) was measured by using two electrical circuits that are shown in Fig. 5.31. In both circuits, the plasma column between the probe tip and anode acts as a voltage source with an inner resistance R_{plasma} and a voltage equal to Φ_{p}. This voltage source is denoted by the dashed rectangle. The probe tip corresponds to the place between $R_{\mathrm{differential}}$ and R_{x} (in Fig. 5.31(a)) or between $R_{\mathrm{differential}}$ and 2 MΩ (in Fig. 5.31(b)).

The average potential Φ_{p} was measured (with respect to the anode ground) by using the circuit on the right (Fig. 5.31(b)), in which the electric current was almost zero; therefore, the measured potential between $R_{\mathrm{differential}}$ and 2 MΩ was practically equal to the potential Φ_{p} in the place between $R_{\mathrm{differential}}$ and R_{plasma}. The average potential Φ was measured by using the circuit on the left (Fig. 5.31(a)). After using Kirchhoff's voltage law in both circuits we can derive the formula for $R_{\mathrm{differential}}$ close to the floating potential as follows:

$$(R_{\mathrm{differential}})_{\Phi_{\mathrm{probe}} \to \Phi_{\mathrm{f}}} = \frac{R_{\mathrm{x}}\Phi_{\mathrm{p}}}{\Phi} - R_{\mathrm{x}}. \tag{5.3}$$

For $I = 75$ A, $p = 20$ kPa, $Ar = 12$ slm, in the position [11.2 mm; 3.8 mm], Φ_{p} was -27 V and Φ had values of 18 V for $R_{\mathrm{x}} = 5.6$ Ω and 19 V for $R_{\mathrm{x}} = 7.0$ Ω. Therefore, for these conditions $(R_{\mathrm{differential}})_{\Phi_{\mathrm{probe}} \to \Phi_{\mathrm{f}}} = 2.9$ Ω, which is in

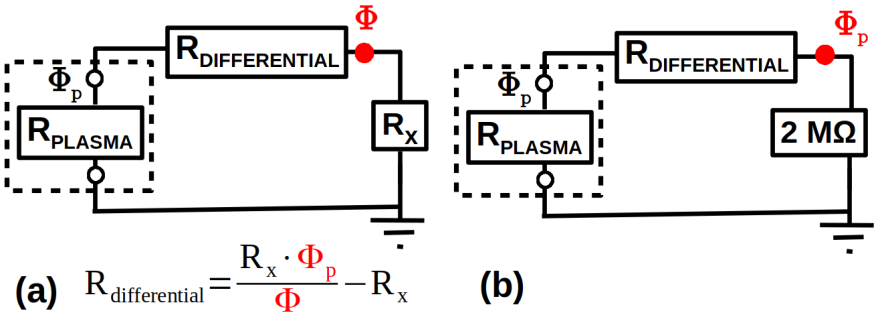

Figure 5.31: Two electrical circuits for measurement of the differential resistance $R_{\mathrm{differential}}$ of the probe $I - \Phi$ characteristic close to the floating potential. The potential Φ_p was measured by using the circuit ***(a)*** *and the potential Φ by using the circuit* ***(b)***

agreement with the inverted first derivative $1/(I'_{\mathrm{probe}}(\Phi_{\mathrm{f}}))$, in Fig. 5.30(a).

We did not know the values of the Debye length λ_{D} and the mean free path of plasma particles l in the plasma at $p < 101$ kPa, but from Table 5.1 it follows that under the working conditions summarized in Table 5.4 λ_{D} was probably in the order of 10^{-8} m and the mean free path of plasma particles was about 10^2 times larger. This is because $\lambda_{\mathrm{D}} \sim \sqrt{1/p}$ and $l \sim 1/p$ [12]. The probe radius (10^{-3} m) was about 10^5 times larger than λ_{D}. Therefore, the sheath around the probes was thin compared to the probe and almost without collisions. In this case, the conventional Langmuir theory cannot be applied to the measured probe $I - \Phi$ characteristic, and either a 'hybrid' theory or a continuum probe theory [11] must be used to process the measured probe $I - \Phi$ characteristic. We therefore cannot use equation (2.28) to find the plasma potential from the values of the probe potential measured under floating conditions.

But just out of curiosity, equation (2.28) gives the difference between the floating potential of the probe and the plasma potential equal to about 5 ± 1 V for I = 75 A and p = 20 kPa, as we can see in Table 5.5. In Table 5.5, T_{e} was measured spectroscopically, and $\Phi(I_{\mathrm{si}})$, Φ_{f}, $\Phi(I_{\mathrm{se}})$ were obtained from the measured probe $I - \Phi$ characteristic.

p [± 0.5 kPa]	$\Phi(I_{\mathrm{si}})$ [± 1 V]	Φ_{f} [± 1 V]	$\Phi(I_{\mathrm{se}})$ [± 5 V]	T_{e} [± 0.04 eV]	$\Phi_{\mathrm{plasma}} - \Phi_{\mathrm{probe}}$ [± 0.3 V]
20	-64	-24	125	0.97	4.7
40	-74	-27	125	1.58	8.1

Table 5.5: The difference between the plasma potential and the probe potential measured under floating conditions in the position [14.8 mm; 4.3 mm] in the case that we can apply Langmuir probe theory and use equation (2.28). $\Phi(I_{\mathrm{si}})$ is the probe potential at the probe current equal to the ion-saturation current, Φ_{f} is the floating potential, and $\Phi(I_{\mathrm{se}})$ is the probe potential at the probe current equal to the electron-saturation current. The values of $\Phi(I_{\mathrm{si}})$, Φ_{f}, $\Phi(I_{\mathrm{se}})$ at p = 20 kPa can be seen in Fig. 5.30(a) (adopted from [56])

In the continuum and 'hybrid' theories, there is no simple formula between

the floating potential and the plasma potential. The plasma potential could, however, be theoretically estimated as the probe potential value at which the probe $I - \Phi$ characteristic changes its convexity to a concavity. But this is not possible in the case of the probe $I - \Phi$ characteristic in Fig. 5.30(a) because of significant uncertainties in the measured values.

In all cases from here on, two electric probes formed part of the electrical circuit shown in Fig. 5.32(a) and were kept in a floating regime ($\Phi_{\text{probe}} \rightarrow \Phi_{\text{f}}$).

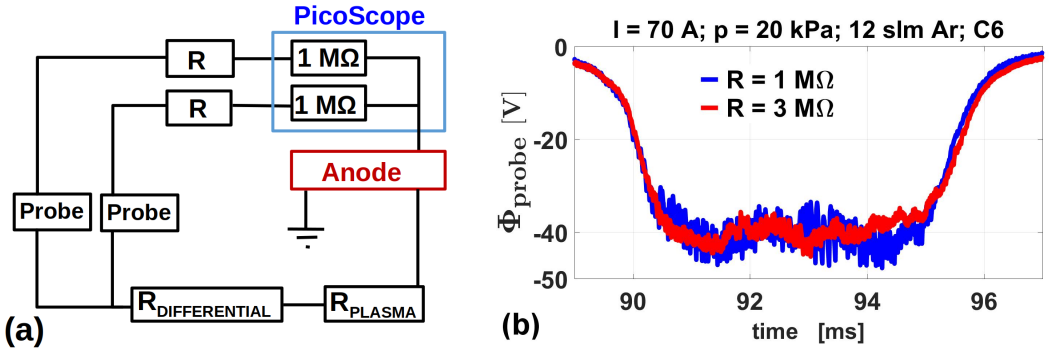

Figure 5.32: ***(a)****The electrical circuit used for measurements of the probe's potential under floating conditions.* $R_{\text{plasma}} < 1\ \Omega$, $R_{\text{differential}} = d\phi_{\text{probe}}/dI_{\text{probe}}$, $R + 1$ MΩ *was the biasing resistance.* ***(b)*** *The time dependence of the probe potential for two values of R in the position [4.0 mm; 4.0 mm]. The blue graph "R = 1 MΩ" is behind the red graph "R = 3 MΩ" (adopted from [56])*

The probe potential measured with a biasing resistance of 4 MΩ was, within the uncertainty, the same as that with a biasing resistance of 2 MΩ (Fig. 5.32(b)). Therefore, the biasing resistance of 2 MΩ (R = 1 MΩ) was sufficient to keep the probes in a floating regime.

In the high-speed camera video footage, it was visible that during the measurements, the probe was emissive. The electron density was about 10^{23} m^{-3} (it was estimated according to [35]). Therefore, it was assumed that the plasma potential in the anode area was approximately the same as the probe potential in the floating regime (Φ_{probe}) and averaged plasma potential values in the anode area, according to this assumption, for $p = 20$ kPa and $I = 75$ A are shown in Fig. 5.33.

The potential of -19 V inside the anode arc attachment was measured by using the pair of electric probes. The probes were not inside the attachment all the time, and therefore only the potential of one probe corresponding to the position of that probe inside the attachment was averaged, to get the value of -19 V. The two probes were separated by 1.6 mm and one probe moved exactly across the attachment (when it was in the position of the probe). The second probe was never totally inside the attachment and the difference in the probes' potential was 1 V. Therefore, it can be estimated that the voltage drop across the anode arc attachment, with a length of about 1 mm, was 1 V, and the copper anode voltage drop seems to be about -18 V at $I = 75$ A.

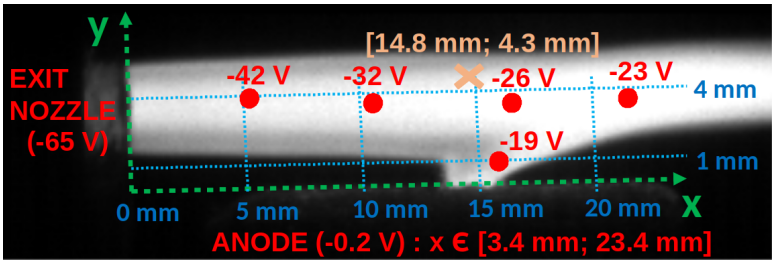

Figure 5.33: The camera image with average measured values of the probe potential, which is almost equal to the plasma potential. I = 75 A, p = 20 kPa, Ar = 12 slm, C6 (adopted from [56])

It appears that the anode voltage drop increases with increases in the arc current because of the following measurements: for I = 300 A and p = 95 kPa the average voltage between the exit nozzle and average attachment creation position (Fig. 5.16) was about 68 V. This corresponds to a distance of about 10 mm. And the average voltage drop U (Fig. 4.4) across the 11 mm long plasma column above the middle part of the anode, for the same conditions, was 3.6 times lower than 68 V. This difference in the voltage drop across the two plasma columns of almost the same length cannot be caused by the difference in the plasma resistivity because the plasma resistivity in the anode area certainly does not decrease with the distance from the exit nozzle. This difference in the voltage drop (68 V vs. 68 V / 3.6) can be explained by an anode voltage drop that is much greater (in its absolute value) than -18 V. At I = 200 A, the situation was similar, and the anode voltage drop came out much greater than -18 V too.

The electric potential of the anode with respect to the anode ground was -0.20 V for I = 50 A and -0.25 V for I = 100 A, and it was measured by using a bent conductive wire touching the rotating anode close to its axis of rotation and connected to the anode ground (0 V). During the rotation of the anode, the wire was sliding over the rotating anode surface, but the connection was fixed enough for it to be possible to measure the voltage between the anode ground and the anode itself.

In the probes' potential signals, there were two kinds of significant fluctuations when the probes moved through the plasma in the anode area. The first kind was high-frequency fluctuations with the same period as the restrike (Fig. 5.34). These are, therefore, almost certainly caused by the movement of the anode arc attachment.

The second kind of fluctuations happened in the time scale of milliseconds (Fig. 5.35).

The diameters of the turbulent vortices observed in schlieren high-speed camera videos (Fig. 5.35(a)) correspond to the width of the fluctuations of the second kind, which was in the order of milliseconds (Fig. 5.35(b),(c)) because according to the movement speed of the probes it follows that 1.1 ms $\Leftrightarrow$ 2.5 mm. Therefore the fluctuations in the probes' potential of the second kind are probably caused by the movement of plasma vortices and are very similar to what are called the

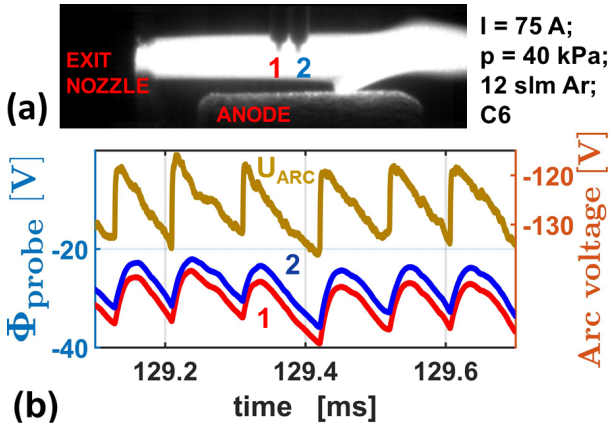

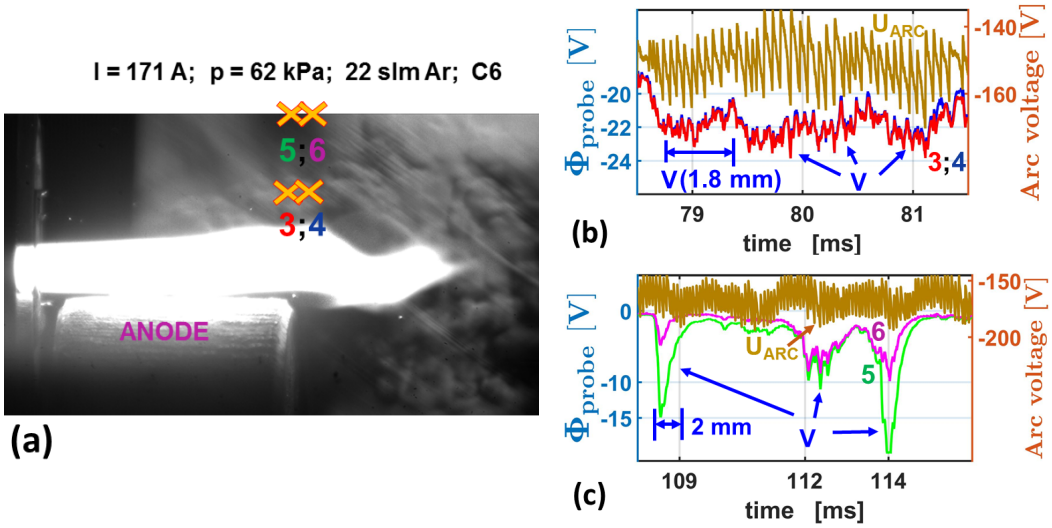

Figure 5.34: ***(a)*** *Camera image with two probes just immersing into the plasma where the fluctuations in the probe potential were measured.* ***(b)*** *The probe potential and arc voltage waveforms corresponding to the measurement in (a) (adopted from [56])*

Figure 5.35: ***(a)*** *A schlieren image with two positions of the pair of the probes where the vortices V were detected.* ***(b), (c)*** *The probe potential and arc voltage (U_{ARC}) waveforms corresponding to (a); waveforms 4 and 6 are above waveforms 3 and 5 (adopted from [56])*

conditionally averaged waveforms that are investigated in the turbulent plasma of tokamaks [10]. Those fluctuations are represented by a more negative probe potential than is in their surrounding (Fig. 5.35(b),(c)), which indicates that the plasma around the vortices is colder than inside the vortices. This is in agreement with the theory of the entrainment of cold gas into thermal plasma jets [64].

In Fig. 5.35(c), at two points in time the potential of probe 5 is significantly lower than the potential of probe 6 (at 108.5 ms and 114.0 ms). This is probably because probe 6 moved directly through a turbulent vortex, while probe 5 reached only its colder edge. The difference between the probe potential inside and around the plasma vortices is greater further from the bright plasma jet (Fig. 5.35(c)) than close to it (Fig. 5.35(b)) or even inside it (Fig. 5.32(b)). Therefore, detecting the turbulent plasma vortices is easiest a few millimeters away from the bright plasma jet.

The waves caused by the movement of the anode arc attachment, which cause the fluctuations in the probe potential of the first kind, propagate through the

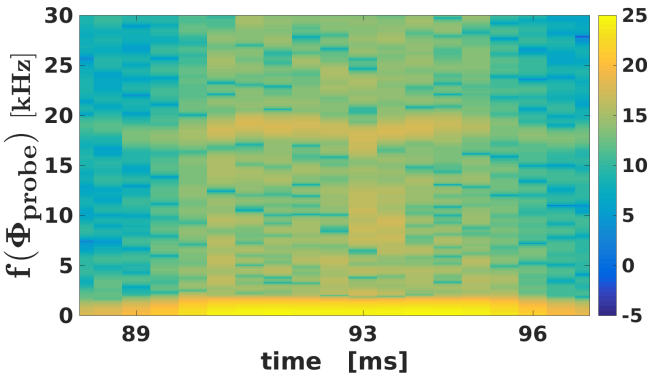

Figure 5.36: Frequency-time spectrogram of power spectral density of Φ_{probe}'s fluctuations shown in Fig. 5.32(b) ($R = 1$ MΩ). The color bar numbers have units of V^2/Hz

whole plasma. This is clear from the frequency-time spectrogram of Φ_{probe}'s fluctuations in Fig. 5.36 because the frequency of the anode arc attachment movement, which was 16-20 kHz, is visible within the whole time during which the probe was inside the plasma, that is to say, from 89 to 96 ms. The time during which the probe was inside the plasma can be seen in the corresponding Φ_{probe}(time), in Fig. 5.32(b).

The sudden small decrease in that frequency from 18.0 to 16.5 kHz around the point in time of 93 ms corresponds to the movement of the probe through the approximately 5 mm wide bright plasma jet visible in the high-speed camera images. According to the corresponding video footage, the probe was inside the 5 mm wide bright plasma jet between 92.2 ms and 94.4 ms.

The strong low-frequency 0-1.5 kHz spectrum of the spectrogram in Fig. 5.36 contains the frequency of fluctuations of the second kind, caused by turbulent vortices.

Fig. 5.37 shows probe potential waveforms measured in the supersonic plasma jet. It follows that it is also possible to detect compression and expansion zones inside a supersonic plasma jet by using electric probes, not only by using a camera. According to the corresponding video footage, whose images are shown in Fig. 5.37(b), probes 1 and 2 were moving through a compression zone that was inside a conical expansion zone.

Our interpretation of Fig. 5.37(a) is the following. The probes' potential decreased when they approached the plasma. Inside the expansion zone, it started to increase (to less negative values), and then inside the compression zone, it abruptly started to decrease (to more negative values). The probes moved through the compression zone very quickly, and in the opposite part of the expansion zone, their potential increased again. When they emerged from the expansion zone their potential decreased once more and again increased outside the plasma.

Probes 3 and 4 were not moving through a compression or expansion zone. Their potential remained almost constant, and the small negative peaks in waveforms 3 and 4 (Fig. 5.37(a)) correspond to the position of the pair in the center of the bright plasma jet. Even though they are displayed in the same figure, waveforms 3 and 4 were measured at a different time than waveforms 1 and 2.

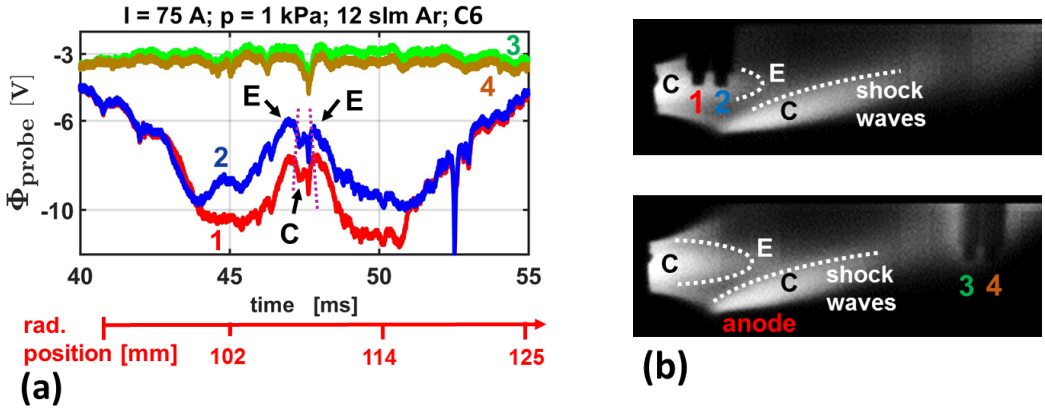

Figure 5.37: ***(a)*** *Probe potential waveforms obtained from the movement of the probes through the expansion (E) and compression (C) zones inside the supersonic plasma jet.* ***(b)*** *The high-speed camera images show the corresponding position of the moving pair of probes, where the signals in (a) were measured (adapted from [56])*

Schlieren images of the shock waves in the supersonic plasma jet were not obtained because the radiation of the bright plasma jet was too intense in comparison with the weak surrounding radiation and weak radiation of the plasma jet boundaries. This problem could be solved by using a disk screen instead of the knife-edge in the schlieren system used, as was the case in 1995 for $p = 101$ kPa (Fig. 5.2).

The probe potential inside the diffuse anode arc attachment is shown in Fig. 5.38. The electric potential inside the diffuse attachment decreases with increases in the distance x from the exit nozzle. From the corresponding high-speed camera video footage, it was seen that a slight bright area occasionally moved within the diffuse attachment and that the diffuse attachment was, on average, brighter closer to the exit nozzle than farther from it. This brightness could be proportional to the current density inside the attachment. The non-uniform brightness of the diffuse anode arc attachment was also observed in other non-transferred plasma torches [72].

5.6 Electric field and electric conductivity

Fig. 5.39 shows the electric field E_{probe} above the anode measured by the pair of electric probes (in the position mentioned in Table 5.4) compared with the corresponding estimated electric field inside the arc column (E_{arc}, Section 4.4). The good agreement suggests that it is not necessary to disturb the plasma by using probes if, under specific working conditions, we only want to know an approximate mean electric field inside the arc column, in the anode area.

When the pair of probes moved through the plasma jet, they alternated between being outside and inside the arc column, because of the periodic movement of the constricted attachment. The maxima of the E_{probe} waveform (the high

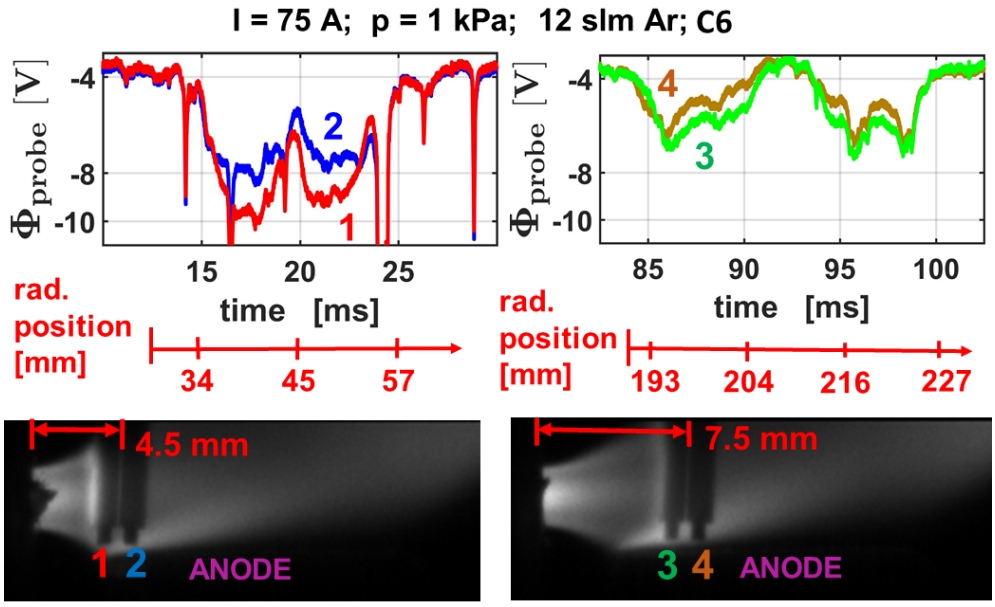

Figure 5.38: Probe potential waveforms measured by the pair of probes as they moved through the diffuse anode arc attachment shown in the corresponding high-speed camera images (adopted from [56])

peaks) correspond to the times when the probes were inside the arc column, and the minima of the E_{probe} waveform (the low peaks) correspond to the times when the probes were not inside the arc column.

The large peak in Fig. 5.39(a) at the time interval of approximately 132-133 ms was very probably the result of a probe shielding at one side of the plasma jet. During the probe shielding, the downstream probe was shielded from the main plasma flow by the upstream probe, that is to say, the downstream probe was in a shadow created by the upstream probe, which caused an additional increase (to less negative values) in the potential of the downstream probe. As we can see, the shielding of the probe in the case of $p = 20$ kPa (mainly the left peak in Fig. 5.39(b) at the point in time of approximately 94.5 ms) is comparable with that at $p = 40$ kPa. Inside the bright plasma jet, about 4.5 mm wide, the shielding of the probe was probably not significant because the plasma temperature is much higher there than around the bright plasma jet. But it could contribute to the fact that the E_{probe} values inside the bright plasma jet corresponding to the arc column were a little greater than the E_{arc} value.

The shielding of the probe in the positions around the bright plasma jet (causing the large peaks in the E_{probe} graphs) was present even when the two probes were shifted in the radial direction $\boldsymbol{x} \times \boldsymbol{y}$ (they were separated by a distance of 2 cm) so that the downstream probe was no longer in the shadow of the upstream probe, regarding the direction of the plasma flow. This is probably because the downstream probe was still in a semi-shadow created by the upstream probe.

Now that we know the electric field in the plasma, we can estimate the relative deviation from the kinetic equilibrium, expressed by equation (2.1), for $I =$

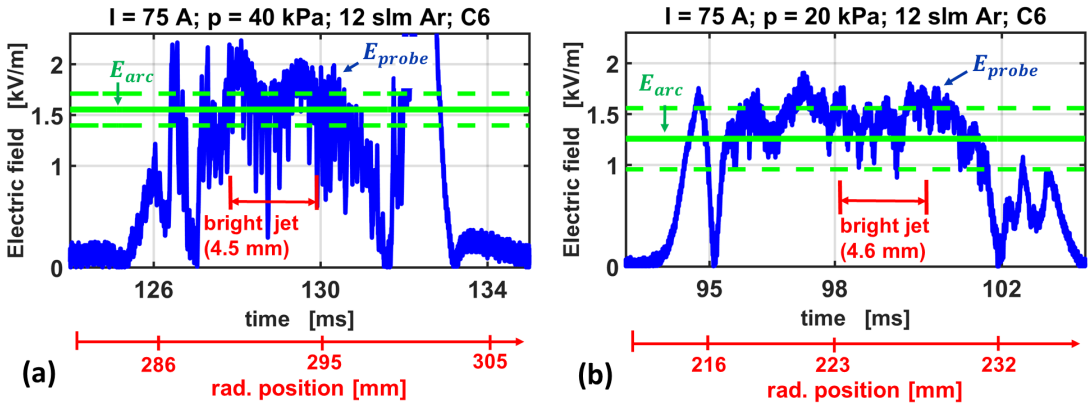

Figure 5.39: Comparison of the electric field E_{probe} waveform measured inside the plasma jet by the pair of electric probes and the estimated electric field E_{arc} inside the arc column at ***(a)*** *$p = 40$ kPa (adapted from [56]) and* ***(b)*** *$p = 20$ kPa. The two horizontal dashed lines express the uncertainty in the E_{arc} values*

75 A, $p = 20$ and 40 kPa, $Ar = 12$ slm, by using the measured electron temperature radial profiles (Fig. 5.40(a)) and computed radial profiles of the mean free path of electrons (Fig. 5.40(b)). The mean free path of electrons l_e was computed by Jenista from his numerical model, for $p = 101$ kPa and $D = 5.3$ mm. 67 and 76 molar % of Ar corresponds to about 22 slm of Ar [6]. If we make the assumption that $l_e \sim 1/p$ [12] and neglect the difference in the argon content (12 slm of Ar vs. 22 slm of Ar), then in the center of the plasma jet $T_e - T_h/T_e = 53 - 269$ % at $p = 20$ kPa and $T_e - T_h/T_e = 10 - 41$ % at $p = 40$ kPa.

This indicates that at $p < 40$ kPa, there is not a kinetic equilibrium inside the plasma of the hybrid plasma torch, and therefore the plasma ceases to be thermal. Jenista reported on relative deviation from the kinetic equilibrium for a water plasma torch and higher arc current values by using his numerical model [62]. The experimental results reported in [73] suggested a deviation from the kinetic equilibrium at very low ambient pressures of 1 and 10 kPa.

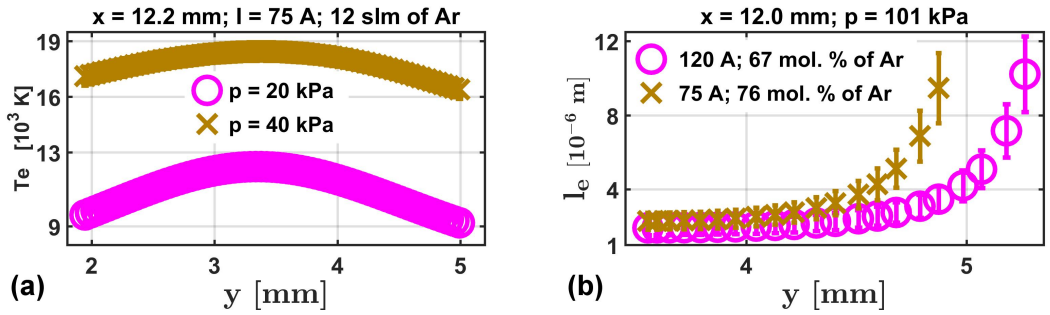

Figure 5.40: ***(a)*** *The radial profile of the electron temperature measured spectroscopically in C6 and* ***(b)*** *half of the symmetric radial profile of the mean free path of electrons computed numerically (the data were provided by courtesy of Jenista). In the numerical model, LTE was considered, the presence of the anode was neglected, and $D = 5.3$ mm*

The estimated electrical conductivity σ_{arc} of the arc column above the anode,

shown in Fig. 5.41, does not depend significantly on the ambient pressure. Its computation is described in Section 4.4.

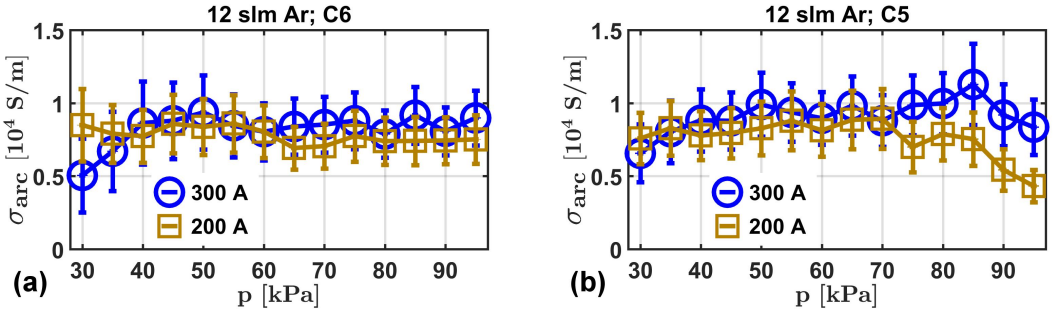

Figure 5.41: The ambient pressure dependence of the estimated electrical conductivity of the arc column above the anode for two arc current values and two anode configurations: ***(a)*** *C6 (adopted from [56]) and* ***(b)*** *C5*

For the purpose of possible future comparison of the experimental results in Fig. 5.41 with simulations or calculated plasma properties, the argon volume/-molar fraction in the plasma was about 30 % for $I = 300$ A and $Ar = 12$ slm [6]. The plasma in the anode area essentially consisted only of argon plasma and a steam plasma. The small fraction of copper vapors and air molecules can be neglected in the anode area because the entrainment of air into the bright plasma jet happens mostly downstream from the anode and the evaporation of the anode is not very significant (Table 5.3). For $I = 200$ A, the argon volume/molar fraction was higher than 30 % because the water evaporated from the stabilizing water vortex at a slower rate than in the case of $I = 300$ A.

The estimated electrical conductivity σ_{arc} increases slightly with increases in the arc current (Fig. 5.42(a), Fig. 5.41). This is because a higher arc current results in a higher plasma temperature. The exception for $p < 40$ kPa, in Fig. 5.41, is probably related to the existence of an expansion and compression zone in the plasma jet at these pressures (Table 5.2). In Fig. 5.42(a), σ_{arc} is compared with the model values "MODEL (22.5 slm)" of the average electrical conductivity of the plasma, which were obtained from the computations published in [65]. The values from the numerical model are still available only for $Ar = 22.5$ slm, not for $Ar = 12.5$ slm.

The model provided a three-dimensional matrix of plasma electric conductivity values. It did not take the presence of an anode into consideration and assumed a perfectly axisymmetric plasma flow. The model values in Fig. 5.42(a) are average values within the fixed cylindrical volume with its bases at distances of 9 and 15 mm from the exit nozzle. These two distances are an average position of the attachment's creation and decay obtained from the corresponding high-speed camera video footage at $p = 101$ kPa.

σ_{arc} does not depend significantly on the argon flow rate (Fig. 5.42(a)). This is probably because the argon flow rate does not significantly influence the plasma temperature [8].

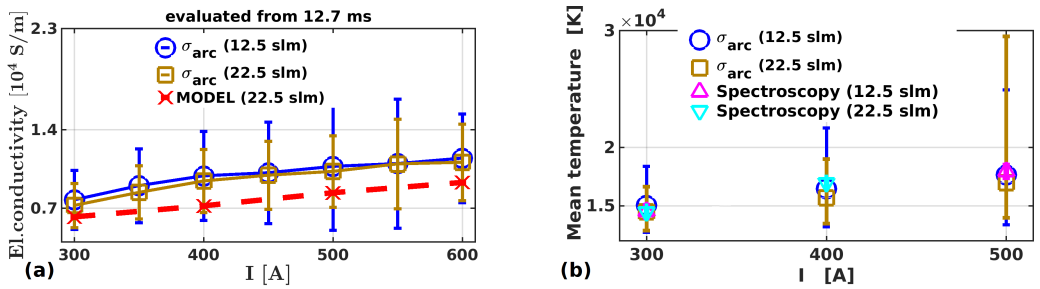

Figure 5.42: ***(a)*** *The arc dependence of the estimated electrical conductivity of the arc column above the anode for two argon flow rates (*12.5 slm *with the larger error bars and* 22.5 slm *with the smaller error bars) compared with average values of the plasma electrical conductivity computed in Jenista's numerical model (the dashed line).* p = 101 kPa, *C1 (adopted from [53]).* ***(b)*** *The mean plasma temperature above the anode corresponding to* σ_{arc} *values compared with the average plasma temperature measured spectroscopically at* x = 2 mm

Fig. 5.42(b) shows the mean plasma temperature above the anode corresponding to the values σ_{arc} in Fig. 5.42(a), according to the calculated properties of steam-argon plasma in thermodynamic equilibrium at p = 101 kPa [35]. The argon molar/volume fractions were obtained from the argon flow rates according to [6]. The average plasma temperature values from spectroscopy measurements, obtained from [8] and [74], are averages of the corresponding radial temperature profiles 2 mm downstream from the exit nozzle.

The great uncertainties in the plasma temperature values obtained from σ_{arc} (denoted in Fig. 5.42(b) as "σ_{arc}(... slm)") follow directly from the great uncertainties of σ_{arc} The uncertainties in the average temperatures measured spectroscopically are 500 K, and they are not shown in the graphs for the sake of clarity. The uncertainty in the "σ_{arc} (12.5 slm)" temperature at I = 500 A was limited to 29,500 K according to the results in [74]. As we can see in Fig. 5.42(b), the average plasma temperature above the anode corresponding to σ_{arc} is too high because it fits with the temperature measured in the hotter area, 2 mm downstream from the exit nozzle. This may indicate that the values of the cross section S used in equation (4.10), estimated from the corresponding high-speed camera video footage as the cross section of the bright plasma jet, were too low.

One possible way to solve the issue is to use cross sections S of the arc current calculated from Jenista's numerical model [65], which are larger than those estimated from the video footage.

The mean electrical conductivity σ_{arc} of the arc column above the anode can be estimated only when the anode arc attachment is constricted, and the arc mode is restrike or takeover. The attachment movement must be visible, as it is in the case of plasma torches with an external anode. Gas plasma torches have a disadvantage because their anode attachment moves in 3D trajectories in cylindrical interiors of anodes and often lack any window to observe the anode attachment even in one dimension.

The estimation of σ_{arc} can be quite localized in the axial direction $\boldsymbol{x}$ if only

restrikes with small L (Fig. 4.7) at a certain distance x from the exit nozzle are used to calculate σ_{arc} by using equation (4.10). At present, to find local values of the electrical conductivity of the plasma in the hybrid or water plasma torches, we must use either spectroscopic temperature measurements + calculated theoretical dependence of the electrical conductivity of the plasma on the plasma temperature [35] or numerical simulations similar to those in [65].

6. Summary and Conclusions

The movement of the constricted anode arc attachment, the constricted and diffuse anode arc attachment itself, anode erosion, electric potential, electric field, electrical conductivity, and turbulent and supersonic structure of the plasma jet, in the anode area of the hybrid plasma torch, were experimentally investigated and described under different experimental conditions. The main experimental tools that were used are a high-speed camera, a high-voltage electric probe and other electric probes. The thesis also obtains some plasma temperature and plasma flow velocity data together with some numerically calculated data of plasma properties, all in the anode area. Regarding the physical phenomena, the main conclusions of the thesis are the following:

1) **A reduction in the ambient pressure** p causes
a **decrease** in

   - the average restrike period (Fig. 5.22(a)),
   - the average distance between the anode attachment and the exit nozzle (Fig. 5.16),
   - the anode erosion (Table 5.3, Fig. 5.28),

   an **increase** in

   - the average speed of the constricted anode arc attachment (Fig. 5.13),

   and a **transition**

   - from the constricted to the diffuse anode arc attachment (Table 5.2),
   - from subsonic to supersonic plasma flow (Table 5.2).

2) **Increases in the arc current** I cause
a **decrease** in

   - the average restrike period (Fig. 5.22(b)),

   an **increase** in

   - the average speed of the constricted anode arc attachment (Fig. 5.14, Fig. 5.15),
   - the anode erosion (Fig. 5.24),

   and a **transition**

   - from subsonic to supersonic plasma flow [63].

3) **Increases in the vertical distance** y_{E} **and horizontal distance** x_{A} between the exit nozzle and the anode cause
a **decrease** in

- the average speed of the constricted anode arc attachment (Fig. 5.13(a)),

an **increase** in

- the average restrike period (Fig. 5.22),

and a **transition**

- from the restrike to the steady arc mode (Fig. 5.9),
- from the diffuse to the constricted anode arc attachment (Fig. 5.10).

The experimental results that describe the movement of the constricted anode arc attachment could be beneficial in computer modeling like that in [75–77] or in practical applications of the hybrid plasma torch, especially in plasma spraying applications.

Regarding the experiments with the hybrid or water plasma torches themselves, the following conclusions are important:

1) There is a direct connection between the anode erosion and the movement of the constricted anode arc attachment.

Previously, this was supposed to be true. However, we found a specific variable [53,56] that quantitatively relates the anode erosion to the attachment movement, so that the connection can be expressed quantitatively.

2) The anode erosion of the hybrid or water plasma torch was amplified and consequently measured directly when the rotational frequency of the anode was low enough [56].

This low rotational frequency is, however, not suitable for hybrid plasma torch applications because of a high resultant anode erosion.

3) The anode erosion of the hybrid plasma torch was compared for different working conditions [56].

4) A high-speed camera was used to directly measure the constricted anode arc attachment speeds, hydrodynamic wave speeds, restrike periods, the extent of the anode erosion, and the range of movement of the attachment on the anode, and to estimate a mean plasma electrical field and a mean plasma electrical conductivity in the anode area of the hybrid plasma torch.

Previously, the attachment speed and hydrodynamic wave speed have been measured, but not directly. The attachment speed was only calculated from the derivative of the arc voltage with respect to time, and a rough approximation was used [78]. Regarding the hydrodynamic wave speed, only the phase speed of hydrodynamic coherent oscillations of the plasma jet was calculated from the phase shift of the oscillations detected by different photodiodes [54, 79, 80].

5) The hybrid plasma torch can also operate stably with an arc current between 40 A and 150 A [56]. We extended the previous investigation of its plasma jet by performing experiments at these low currents.

Previously, the plasma jet has been studied only for a minimum arc current of 150 A [9]. Arc currents of the hybrid plasma torch lower than 150 A have been used only in one case [7].

6) Electric probes were used for measurements of plasma characteristics of the hybrid plasma torch also in the anode area, even very close to the exit nozzle.

We conducted measurements with electric probes in the anode area at $I = 40$, 70, and 75 A [56]. The probes were not damaged, so they can be used in the anode area even for arc currents higher than 75 A. Previously, electric probes have not been inserted into the anode area (0-25 mm from the exit nozzle) of the hybrid plasma torch; they were inserted only into the anode area of the water plasma torch [81, 82] (where they were connected via a resistor to the cathode). In the case of the hybrid plasma torch, they have always been connected to the anode via a resistor, and previously, they have only been used at distances of approximately 30 mm and more from the exit nozzle [83, 84].

7) Enthalpy probes can be applied for the measurements of plasma characteristics (temperature, velocity, etc.) even in the anode area (0-25 mm from the exit nozzle) of the hybrid plasma torch when the arc current is very low.

In our experiments, we inserted an enthalpy probe into the anode area at $I =$ 40 A. The enthalpy probe was not damaged by the heat. It follows that it can be used in the anode area even for arc currents higher than 40 A. During experiments, an isolation transformer must be used to electrically isolate the enthalpy probe system from the power socket. Previously, enthalpy probes have been used only at distances greater than approximately 60 mm from the exit nozzle [9].

8) A diffuse anode arc attachment at atmospheric ambient pressure, common for gas plasma torches, was also obtained with the hybrid plasma torch (Fig. 5.10(b)). It follows it can be obtained with very similar water plasma torches too.

However, that diffuse attachment at atmospheric pressure seems not to be suitable for practical applications of the torch as there is a high-enough probability of the arc becoming connected to the exit nozzle, which consequently causes severe damage to the exit nozzle gap and consequently a releasing of water from the stabilizing water vortex. Further improvement to the plasma torch must be made to enable the use of that attachment, for example, an intensified cooling of the exit nozzle.

9) A stable position of the constricted anode arc attachment in the axial direction, common for gas plasma torches, was also obtained with the hybrid plasma torch ([53] or Fig. 5.9, and VIDEO 7 in the Supplement to this thesis). It follows that it can be obtained with the water plasma torches as well.

This steady mode is useful for the investigation of phenomena in the anode area, for example, when we need to have a stable plasma jet. It is not very suitable for practical applications of the plasma torch, however, because of a high anode erosion in this mode (especially at high arc currents).

Regarding the hybrid plasma torches, there are still challenges for the future: for example, to directly measure the anode erosion under the common working conditions used in practice; to create schlieren images of the shock waves in the supersonic plasma jet; or to measure the rate of the water evaporation in the stabilizing water vortex of the torch with reasonable uncertainty. New methods for plasma velocity measurements would also be appreciated – for example, tracking of solid particles inside the plasma jet by using a high-speed camera, which has already been used in the case of gas plasma torches.

It is also challenging to make the measurements mentioned in this thesis during plasma spraying, organic waste gasification, pyrolysis, or hydrocarbon reforming. Up to now, the experimental investigation of the plasma created by the hybrid plasma torches has been separated from the conducting or studying of the practical applications of the torches themselves.

Something that is even more challenging is finding a way to relate the findings about the hybrid or water plasma torches to gas plasma torches more closely. A wider application of the findings connected with the hybrid and water plasma torches to gas plasma torches would greatly increase the significance of those findings and attract more people to the issue of hybrid plasma torches.

Bibliography

[1] Hrabovsky M *et al* 2018 Plasma Waste Destruction *in Handbook of Thermal Science and Engineering* ed A F Kulacki (Basel: Springer, Cham)

[2] Hrabovsky M 2011 Thermal Plasma Gasification of Biomass *in Progress in Biomass and Bioenergy Production* ed S S Shaukat (Rijeka: IntechOpen)

[3] Hrabovsky M *et al* 2017 Steam Plasma Treatment of Organic Substances for Hydrogen and Syngas Production *Plasma Chem Plasma Process* **37** 739–762. Online ISSN 1572-8986

[4] Hlina M *et al* 2014 Production of high quality syngas from argon/water plasma gasification of biomass and waste *Waste Management* **34** 63–66. DOI: 10.1016/j.wasman.2013.09.018

[5] Hrabovsky M *et al* 2018 Steam Plasma Methane Reforming for Hydrogen Production *Plasma Chem Plasma Process* **38** 743–758. Online ISSN 1572-8986

[6] Kavka T *et al* 2011 Plasma Spraying of Copper by Hybrid Water-Gas DC Arc Plasma Torch *Journal of Thermal Spray Technology* **20** 760–774. Online ISSN 1544-1016

[7] Brezina V *et al* 2001 New plasma spraying torch with combined gas-liquid stabilization of arc *Proc of the 15th Int Symp on Plasma Chem* (Orléans, France) vol 3 pp 1021–1026

[8] Hrabovsky M *et al* 2006 Properties of Hybrid Water/Gas DC Arc Plasma Torch *IEEE Transactions on Plasma Science* **34** 1566–1575. Electronic ISSN: 1939-9375

[9] Kavka T 2006 *Study of Thermal Plasma Jets Generated by DC Arc Plasma Torches used in Plasma Spraying Applications* PhD thesis, Charles University, Faculty of Mathematics and Physics

[10] Ondac P 2014 *Study of tokamak plasma turbulence by means of reciprocating probes* Master's thesis, Charles University, Faculty of Mathematics and Physics

[11] Chung P M *et al* 1975 *Electric probes in stationary and flowing plasmas: Theory and Applications* (New York: Springer-Verlag New York)

[12] Boulos M I *et al* 1994 *THERMAL PLASMAS Fundamentals and Applications*, Volume 1 (New York and London: Plenum Press)

[13] Rutherford P H Goldston R J 1995 *Introduction to plasma physics* (Bristol, UK: Institute od Physics Publishing)

[14] Maecker H 1955 Plasmaströ mungen in lichtbögen infolge Eigenmagnetische Kompression *Zeitschrift für Physik* **141** 198–216

[15] Wutzke S A *et al* 1968 Symptomatic behavior of an electric arc with a superimposed flow *AIAA J* **6** 1474–1482

[16] Wutzke S A *et al* 1967 Study of electric arc behaviour with superimposed flow *AIAA J* **5** 707–713

[17] Duan Z *et al* 2002 Arc instabilities in a plasma spray torch *J Thermal Spray Technol* , **11** 44–51

[18] Rat V *et al* 2017 Electric arc fluctuations in DC plasma spray torch *Plasma Chemistry and Plasma Processing* **37** 549–580

[19] Wutzke S A 1967 *Conditions governing the symptomatic behavior of an electric arc in superimposed flow field* PhD thesis, University of Minnesota

[20] Hrabovsky M *et al* 1997 Motion of anode attachment and fluctuations of plasma jet in dc arc plasma torch *J. of High. Temp. Material Processes* **1** 167–178

[21] Hrabovsky M *et al* 1999 Effect of Anode Attachment on Flow Structure of Plasma Jet Generated in Water Stabilized Torch *Proc of the 2nd Int Symp on Heat and Mass transfer under Plasma Conditions* (Antalya, Turkey) vol 891 pp 98–105

[22] Hrabovsky M *et al* 2001 Investigation of propagation of perturbations in thermal dc arc plasma jet *Progress in Plasma Processing of Materials* 223–228. ISSN: 1-56700-165-3 (Print)

[23] Ghorui S *et al* 2007 Probing instabilities in arc plasma devices using binary gas mixtures *Phys. Rev. E* **76** Art. No. 016404, 13 pages. DOI: 10.1103/PhysRevE.76.016404

[24] Ghorui S *et al* 2015 Direct probing of anode arc root dynamics and voltage instability in a dc non-transferred arc plasma jet *Plasma Sources Science and Technology* **24** Art. No. 065003, 10 pages

[25] Hrabovsky M *et al* 2009 Thermal Plasma Generators with Water Stabilized Arc *The Open Plasma Physics Journal* **2** 99–104. DOI: 10.2174/1876534300902010099

[26] Gerdien H *et al* 1992 Wasserstabilisierter Lichtbogen *Wiss Veroff Siemenswerk* **2** 489–492

[27] Maecker H 1951 Ein Lichtbogen fü höhe Leistungen *Zeitschrift für Physik* **129** 108–122

[28] Burnhorn F *et al* 1951 Feldstärkemessungen an wasserstabilisierten Hochleistungsbögen *Z Phys* **129** 369–376

[29] Larentz R W 1951 Temperaturmessungen in der Säule eines Gerdien-Bogens *Z Phys* **129** 343–364

[30] Burnhorn F *et al* 1951 Temperaturmessungen am wasserstabilisierten Hochleistungsbogen *Z Phys* **131** 128–140

[31] Hrabovsky M 2013 DC torches with arc stabilization by liquids *in Plasma Assisted Combustion, Gasification, and Pollution Control: Volume 1. Methods of Plasma Generation for PAC* ed I B Matveev (Colorado, Denver: Outskirts Press, Inc.)

[32] Tendero C *et al* 2006 Atmospheric pressure plasmas: A review *Spectrochimica Acta Part B* **61** 2–30. DOI: 10.1016/j.sab.2005.10.003

[33] Iwata M *et al* 1998 Effects of arc current and electrode size on electrode erosion in ac plasma torches *Electr Eng Jpn* **124** 10–17

[34] Szente R N *et al* 1992 Electrode erosion in plasma torches *Plasma Chemistry and Plasma Processing* **12** 327–343

[35] Krenek P *et al* 2008 Thermophysical Properties of H20-Ar Plasmas at Temperatures 400-50,000k and Pressure 0.1 MPa *Plasma Chem Plasma Process* **28** 107–122

[36] Kavka T *et al* 2006 Experimental investigation of development of fully turbulent plasma jet generated by hybrid gas-water torch *Czechoslovak Journal of Physics* **56** B821–B829

[37] Kibble T W B *et al* 2004 *Classical Mechanics*, 5th Edition (London: Imperial College Press)

[38] Howatson A M 1976 *An Introduction to Gas Discharges*, Second Edition (Pergamon Press)

[39] Yoshizava A *at al* 2002 *Plasma and fluid turbulence: theory and modelling* (Teddington, Middlesex, United Kingdom: Taylor & Francis)

[40] Vortex formation in free jet caused by Kelvin-Helmholtz instability. In: *Youtube.com* [online]. [Cit. June 28, 2019]. Available from: https://www.youtube.com/watch?v=ELaZ2x42dkU&hd=1

[41] Bejan A 2013 *Convection heat transfer*, Fourth Edition (Hoboken, New Jersey: John Wiley & Sons, Inc.)

[42] Gindrat M *et al* 2004 Characterization of supersonic low pressure plasma jets with electrostatic probes *Plasma Sources Science and Technology* **13** 484–492

[43] Mayinger F *et al* 2001 *Optical Measurements, Techniques and Applications*, 2nd Edition (Germany: Springer-Verlag Berlin Heidelberg)

[44] Settles G S 2001 *Schlieren and Shadowgraph Techniques, Visualizing Phenomena in Transparent Media* (Germany: Springer-Verlag Berlin Heidelberg)

[45] Sexiest thing evah... Schlieren Imaging of a candle being blown out. In: *Youtube.com* [online]. [Cit. April 11, 2019]. Available from: https://www.youtube.com/watch?v=gxOeV658qgg

[46] Chen F F. Lecture Notes on Langmuir Probe Diagnostics. *Electrical Engineering Department University of California, Los Angeles. Mini-Course on Plasma Diagnostics, IEEE-ICOPS meeting, Jeju, Korea, June 5, 2003.* In: *http://www.seas.ucla.edu* [online]. [Cit. July 31, 2019]. Available from: http://www.seas.ucla.edu/ ffchen/Publs/Chen210R.pdf

[47] Lipschultz B *et al* 1986 Electric probes in plasmas *J. Vac. Sci. Technol. A.* **4** 1810–1816. DOI: 10.1116/1.573945

[48] Gick A E F *et al* 1973 The use of electrostatic probes to measure the temperature profiles of welding arcs *J. Phys. D: Appl. Phys* **6** 1941–1949

[49] Leveroni E *et al* 1989 Electric probe diagnostics in thermal plasmas: Double probe theory and experimental results *Review of Scientific Instruments* **60** 3744–3749

[50] Cherrington B E *et al* 1982 The use of Electrostatic Probes for Plasma Diagnostics—A Review *Plasma Chem Plasma Process* **2** 113–140

[51] Duan Z *et al* 2001 A langmuir multi-probe system for the characterization of atmospheric pressure arc plasmas *J. Phys. D: Appl. Phys* **34** 2715–2725

[52] Ondac P *et al* 2016 Investigation of the arc-anode attachment area by utilizing a high-speed camera *Plasma Physics and Technology* **3** 1–4

[53] Ondac P *et al* 2018 Measurement of Anode Arc Attachment Movement in DC Arc Plasma Torch at Atmospheric Pressure *Plasma Chem Plasma Process* **38** 637–654. DOI: 10.1007/s11090-018-9888-0

[54] Kopecky V *et al* 2004 Dependence of frequency and phase velocity of plasma jet hydrodynamic instability on sound velocity *Czechoslovak Journal of Physics* **54** C1056–C1061

[55] Szente R N *et al* 1992 Effect of the arc velocity on the cathode erosion rate in argon-nitrogen mixtures *J. Phys. D: Appl. Phys.* **12** 327–343

[56] Ondac P *et al* 2019 Experimental Investigation of Anode Arc Attachment Area in DC Arc Plasma Torch at Low Pressures *J. Phys. D: Appl. Phys.* **52** Art. No. 405201 (14 pages). DOI: 10.1088/1361-6463/ab3197

[57] Jenista J *et al* 2004 Numerical modeling of hybrid stabilized electric arc with uniform mixing of gases *IEEE Trans Plasma Sci* **32** 464–472

[58] Stephanie B 2001 *A Beginner's Guide to Uncertainty of Measurement* (Teddington, Middlesex, United Kingdom: Centre for Basic, Thermal and Length Metrology National Physical Laboratory)

[59] Chumak O *et al* 2006 Electric Probe Investigation of Arc Anode Region in Plasma Torch *High Temp Mater Proc* , **10** 515–524

[60] Jenista J *et al* 2011 Numerical Investigation of Hybrid-Stabilized Argon–Water Electric Arc Used for Biomass Gasification *in Progress in Biomass and Bioenergy Production* ed S S Shaukat (Rijeka: IntechOpen)

[61] Hrabovsky M *et al* 2004 Properties of Plasma Jet Generated in Hybrid Gas/Water Torch under Reduced Pressures *High Temperature Material Processes* **8** 575–584. ISSN Online: 1940-4360

[62] Jenista J *et al* 2003 Water-vortex-stabilized electric arc: III. Radial energy transport, determination of water-vapour-boundary and arc performance *J. Phys. D: Appl. Phys.* **36** 2995–3006

[63] Kavka T *et al* 2009 Transition of thermal plasma jet from subsonic to supersonic regime *Proc of the 19th Int Symp on Plasma Chem* (Bochum, Germany) pp Art. No. O5.06, pp 1–4

[64] Pfender E *et al* 1991 Entrainment of Cold Gas into Thermal Plasma Jets *Plasma Chemistry and Plasma Processing* **11** 529–543

[65] Jenista J *et al* 2011 Integrated parametric study of a hybrid-stabilized argon-water arc under subsonic, transonic and supersonic plasma flow regimes *J. Phys. D: Appl. Phys.* **44** Art. No. 435204

[66] Pan W *et al* 2007 Comparative Observation of Ar, Ar-H2 and Ar-N2 DC Arc Plasma Jets and Their Arc Root Behaviour at Reduced Pressure *Plasma Science and Technology* **9** 152–157

[67] Yang G *et al* 2007 The anode region of high intensity arcs with cold cross flow *J. Phys. D: Appl. Phys.* **40** 5649–5662

[68] Jenista J *et al* 1999 Effect of Vortex Motion of Stabilizing Liquid Wall on Properties of Arc in Water Plasma Torch *Proc of Int Symp on Heat and mass transfer under plasma conditions* (New York: Annal of the New York Academy of Sciences) vol 891 pp 64–71

[69] Tu X *et al* 2007 Dynamic behaviour of dc double anode plasma torch at atmospheric pressure *J. Phys. D: Appl. Phys.* **40** 3972–3979

[70] Terasaki H *et al* 2003 Effects of Anode Heat Transfer on Weld Penetration in Gas Tungsten Arc Welding *Proc of Int Symp on Joining and Welding Solution to Industrial Innovation* (JWRI, Osaka University) vol 32 pp 29–31

[71] Popov S A *et al* 2012 Anode jet in a high-current vacuum arc *Technical Physics* **57** 938–944

[72] Wang C *et al* 2019 Experimental Observations of Constricted and Diffuse Anode Attachment in a Magnetically Rotating Arc at Atmospheric Pressure *Plasma Chem Plasma Process* **39** 407–421. DOI: 10.1007/s11090-019-09954-z

[73] Sember V *et al* 2007 Investigation of supersonic thermal plasma jet *Proc of the 18th International Symposium on Plasma Chemistry* (Kyoto, Japan) pp Art. No. 30P–158, 4 pages

[74] Sember V *et al* 2009 A simple spectroscopic method for determining the temperature in $h_2$0-ar thermal plasma jet *High Temp Mat Proc* **13** 217–228

[75] Trelles J P *et al* 2007 Modelling of the arc reattachment process in plasma torches *J. Phys. D: Appl. Phys.* **40** Ar. No. 5635

[76] Baudry C *et al* 2005 Numerical modeling of a dc non-transferred plasma torch: movement of the arc anode attachment and resulting anode erosion *High Temp. Mater. Proess* **9** 1–15

[77] Moreau E *et al* 2006 Modeling of the restrike mode operation of a dc plasma spray torch *J. Thermal Spray Technol.* **15** 524–530

[78] Hrabovsky M *et al* 2005 Effect of pressure on behavior of anode attachment of dc arc plasma torch *High Temperature Material Processes* **9** 391–399. DOI: 10.1615/HighTempMatProc.v9.i3.60

[79] Hrabovsky M *et al* 2001 Investigation of Rayleigh instability in thermal plasma jet generated by plasma torch with external anode *Proc of the 15th Int Symp on Plasma Chem* (Orléans, France) vol 3 pp 861–866

[80] Kopecky V *et al* 2003 Determination of flow velocity from analysis of hydrodynamic oscillations of thermal plasma jet *High Temperature Material Processes* **7** 6 pages. DOI: 10.1615/HighTempMatProc.v7.i1.40

[81] Hrabovsky M *et al* 1994 Electrical probe investigation of structure of dc arc plasma jet *Proceedings of the International Symposium on Heat Mass Transfer under Plasma Conditions* (Cesme, Turkey) pp 61–66

[82] Hrabovsky M *et al* 1993 Application of electric probes for study of structure of thermal plasma jet *Proceedings of the 16th symposium on plasma physics and technology* (Prague, Czech Republic) vol 24 pp 236–242

[83] Hurba O *et al* 2016 Diagnostics of Plasma Jet Generated in Water/Argon DC Arc Torch *Plasma Physics and Technology* **3** 5–8

[84] Hurba O *et al* 2015 Electric probe diagnostics of low pressure dc arc steam-argon plasma jet *Proc of the 22nd Int Symp on Plasma Chem* (Antwerp, Belgium) pp Art. No. P–II–12–7 (4 pages)

List of Abbreviations

IPP CAS	—	**I**nstitute of **P**lasma **P**hysics of the **C**zech **A**cademy of **S**ciences
WSP®-H 2011	—	**H**ybrid **W**ater-gas **S**tabilized **P**lasma torch developed in **2011**
TP	—	**T**hermal **P**lasma
LPT	—	**L**aboratory of **P**lasma **T**echnologies
WSP®-HR	—	**H**ybrid **W**ater-gas **S**tabilized **P**lasma torch inside a **R**eactor
WSP® 500	—	**W**ater **S**tabilized **P**lasma torch with the maximal safe value of the arc current of **500** A
LTE	—	**L**ocal **T**hermodynamic **E**quilibrium

List of publications by Ondac related to the thesis

Related publications in scientific journals

- **Ondac P**, Maslani A and Hrabovsky M 2019 Experimental Investigation of Anode Arc Attachment Area in DC Arc Plasma Torch at Low Pressures *J. Phys. D: Appl. Phys.* **52** Art. No. 405201 (14 pages)
  DOI: 10.1088/1361-6463/ab3197

- **Ondac P**, Maslani A, Hrabovsky M and Jenista J 2018 Measurement of Anode Arc Attachment Movement in DC Arc Plasma Torch at Atmospheric Pressure *Plasma Chem Plasma Process* **38** 637-654
  DOI: 10.1007/s11090-018-9888-0

- **Ondac P**, Maslani A and Hrabovsky M 2016 Investigation of the arc-anode attachment area by utilizing a high-speed camera *Plasma Physics and Technology* **3** 1-4

- Maslani A, **Ondac P**, Sember V and Hrabovsky M 2018 Time-Resolved Emission Spectroscopy Measurements during the Restrike Period in Arc Plasma Torch *Journal of Spectroscopy* Art. ID 4614028 (7 pages)
  DOI: 10.1155/2018/4614028

Related publications in proceedings of international conferences

- **Ondac P**, Maslani A and Hrabovsky M 2017 Measuring of Mean Plasma Electrical Conductivity in Anode Area of Plasma Torches with an External Anode *WDS'17 Proceedings of Contributed Papers — Physics (eds. J. Safrankova and J. Pavlu)* (Prague: MATFYZPRESS) pp 88-93

- **Ondac P**, Maslani A, Hrabovsky M, Jenista J and Sember V 2017 Measuring of mean electrical conductivity of a plasma volume in hot anode area of DC arc plasma torches *Proc. of the 44th European Physical Society Conference on Plasma Physics* (Mulhouse: European Physical Society) vol 41F Art. No. O2.306 (4 pages)

- **Ondac P**, Maslani A and Hrabovsky M 2016 Arc–Anode Attachment Area in DC Arc Plasma Torch at Low Pressure *WDS'16 Proceedings of Contributed Papers — Physics (eds. J. Safrankova and J. Pavlu)* (Prague: MATFYZPRESS) pp 132-136

- **Ondac P**, Maslani A and Hrabovsky M 2015 Investigation of Anode Attachment Area in Water/Argon Stabilized Plasma Arc *WDS'15 Proceedings of Contributed Papers — Physics (eds. J. Safrankova and J. Pavlu)* (Prague: MATFYZPRESS) pp 245-251

MATLAB scripts

MATLAB script for attachment movement investigation

```
%SCRIPT1_Attachment_movement_LOW
% Updated: 17.04.2019

tic;
clear VYSTUP_M
clear a
clear A
graphs='1';
J0=900; % starting ambient pressure in mbar
JN=900; % ending ambient pressure in mbar
VYSTUP_M=zeros((JN-J0)/50+1,13);
s=1; % line in the output of this script: VYSTUP_M
for v=J0:50:JN
clear chybajuce
chybajuce=0;
Videos_paths_LOW_Linux  % in this script, there are
   different values of "text" and "retazec" variable
text=text5;
retazec=retazec4;
POHYB='CELY';  % variable determining whether the whole
   attachment movement is investigated or only its part
%POHYB='CIASTOCNY';
path=[text,retazec,'avi'];
Videos_properties_LOW % in this script, there are e.g.
   zaciatok, koniec, N0, Nf, faktor, riadok and down
   variables for various videos/measuremetns
vid=VideoReader(path);
time=((N0-1)*(10/3):(10/3):(Nf-1)*(10/3)); % time vector
   for attachment position
pixel_pos=zeros(1,Nf-N0+1);
position=zeros(1,Nf-N0+1);

if (strcmp(POHYB,'CIASTOCNY')) %  --> ATTACHMENT MOVEMENT
   is investigated only along A PART OF THE ANODE (without
    the end of the anode)
for f = N0:1:Nf
  frame = read(vid,f);
   a=find((frame(riadok,zaciatok:koniec)>down)&(frame(
      riadok,zaciatok:koniec)<(2^vid.BitsPerPixel-1)));
   % variable "a" containts position of the pixels that
      have value greater
```

```
33      % than the value "down", because they represent a
            bright plasma in the
34      % attachment
35      % variable "riadok" represents the line in the videos'
            frames in which
36      % the attachment position was finding
37      % "zaciatok" represents the pixel position from which
            the attachment
38      % movement was investigated
39      % "koniec" represents the pixel position until which
            the attachment
40      % movement was investigated
41      if isempty(a)
42       pixel_pos(f-N0+1)=NaN;
43        position(f-N0+1)=(pixel_pos(f-N0+1)+zaciatok-1-koniec
              )*faktor+14;
44      else
45      pixel_pos(f-N0+1)=a(1);
46       position(f-N0+1)=(pixel_pos(f-N0+1)+zaciatok-1-koniec)
             *faktor+14;
47      end
48  % "position" is a vector that contains the attachment
      positions in mm
49  end % end for f = N0:1:Nf
50
51  elseif (strcmp(POHYB,'CELY')) % --> THE WHOLE ATTACHMENT
      MOVEMENT is investigated
52  for f = N0:1:Nf
53    frame = read(vid,f);
54   a=find((frame(riadok,zaciatok:end)>down)&(frame(riadok,
        zaciatok:end)<(2^vid.BitsPerPixel-1)));
55       if isempty(a)
56       chybajuce=chybajuce+1
57       f_video_cih=f-1
58        pixel_pos(f-N0+1)=NaN;
59        position(f-N0+1)=(pixel_pos(f-N0+1)+zaciatok-1-koniec
              )*faktor+14;
60       % attachment position in mm from the beginning of the
            anode, because the variable "koniec" is the pixel
            value
61       % ... in the position 6 mm from the end of the anode
62       else
63       pixel_pos(f-N0+1)=a(1);
64       position(f-N0+1)=(pixel_pos(f-N0+1)+zaciatok-1-koniec)
             *faktor+14;
65       % attachment position in mm from the beginning of the
            anode, because the variable "koniec" is the pixel
            value
```

```
    % ... in the position 6 mm from the end of the anode
    end
    clear a
end
end
 % %%%%%%%%%%%%%%%%%%%%%%%%%%%%%%%%%%%%%%%%%%%%%%%%%%%%%%%%%%%%%%%%%%%%%%%%%%%%%%%%%%%%%

if 1 % for calculating t_periods
clear ymax ymin imax imin
if (strcmp(POHYB,'CELY'))
k=1;
for i=1:(length(position)-1)
    if ((position(i)-position(i+1)) > 1)
        ymax(k)=position(i);
        imax(k)=i;
        ymin(k)=position(i+1);
        imin(k)=i+1;
        % imax, imin are indexes for maxima and minima vectors in the time
        % dependence of the attachment position
        k=k+1;
    else
    end
end
elseif (strcmp(POHYB,'CIASTOCNY'))
k=1;
for i=2:(length(position)-1)
    if ( ( ((position(i-1)-position(i)) > 1)  && (~isnan(position(i+1))) )  || ( (isnan(position(i-1))) && (~isnan(position(i+1))) && (~isnan(position(i))) ) )
        ymin(k)=position(i);
        imin(k)=i;
        z=1;
        while ( ((i+z+1)<=length(position)) && (~isnan(position(i+z+1))) && ((position(i+z)-position(i+z+1)) < 1) )
            z=z+1;
        end
        ymax(k)=position(i+z);
        imax(k)=i+z;
        k=k+1;
    else
    end
end
end
%% I want the following order: max, min, ..., min
```

```
if ((length(ymin)==length(ymax)+1)  && (imax(1)>imin(1)) )
     %% if min, max, ..., min
      % ymin=ymin(2:end); % remove the first min
       imin=imin(2:end);
elseif ((length(ymax)==length(ymin))  && (imax(1)>imin(1)) )
     %% if min, max, ..., max
      % ymax=ymax(1:end-1); % remove the last max
       imax=imax(1:end-1);
      % ymin=ymin(2:end);   % remove the first min
       imin=imin(2:end);
elseif ((length(ymax)==length(ymin)+1)  && (imax(1)<imin(1)) )
     %% if max, min, ..., max
      % ymax=ymax(1:end-1);  % remove the last max
       imax=imax(1:end-1);
elseif ((length(ymax)==length(ymin)) && (imax(1)<imin(1)) )
     %% if max, min, ..., min
end
restrike_length=mean(ymax-ymin);
%% I took only periods corresonding to the large drops
periods_max=abs(diff(time(imax)));
periods_min=abs(diff(time(imin)));
t_average_help=mean([mean(periods_max) mean(periods_min)]);
t_periods=mean([mean(periods_max(periods_max<2*t_average_help)) mean(periods_min(periods_min<2*t_average_help))]);
end % for calculating t_periods
%%%%%%%%%%%%%%%%%%%%%%%%%%%%%%%%%%%%%%%%%%%%%%%%%%%%%%%%%%%%%%%

%% finding extrema in the time dependence of the attachment position
clear ymax ymin imax imin
if (strcmp(POHYB,'CELY'))
k=1;
for i=1:(length(position)-1)
    if ((position(i)-position(i+1)) > 1)
         ymax(k)=position(i);
         imax(k)=i;
         ymin(k)=position(i+1);
         imin(k)=i+1;
         k=k+1;
    else
    end
end
```

```
145 elseif (strcmp(POHYB,'CIASTOCNY'))
146 k=1;
147 for i=2:(length(position)-1)
148     if ( ( ((position(i-1)-position(i)) > 1) && (~isnan(
            position(i+1))) ) || ( (isnan(position(i-1))) &&
            (~isnan(position(i+1))) && (~isnan(position(i))) )
            )
149         ymin(k)=position(i);
150         imin(k)=i;
151         z=1;
152          while ( ((i+z+1)<=length(position)) && (~isnan(
                position(i+z+1))) && ((position(i+z)-position(
                i+z+1)) < 1) )
153              z=z+1;
154         end
155         ymax(k)=position(i+z);
156         imax(k)=i+z;
157         k=k+1;
158     else
159     end
160 end
161 end
162     %% I want the following order: min, max, ..., max,
            that is: min(1), max(1), min (2), max(2), ..., max(
            end)
163
164   if ((length(ymin)==length(ymax)+1) && (imax(1)>imin(1))
          )
165     %% if  min, max, ..., min
166       ymin=ymin(1:end-1); % remove the last min
167       imin=imin(1:end-1);
168   elseif ((length(ymax)==length(ymin)) && (imax(1)>imin
        (1)) )
169     %% if min, max, ..., max
170   elseif ((length(ymax)==length(ymin)+1) && (imax(1)<imin
        (1)) )
171     %% if  max, min, ..., max
172       ymax=ymax(2:end);  % remove the first max
173       imax=imax(2:end);
174   elseif ((length(ymax)==length(ymin)) && (imax(1)<imin(1)
        ) )
175     %% if max, min, ..., min
176      ymax=ymax(2:end);  % remove the first max
177       imax=imax(2:end);
178       ymin=ymin(1:end-1); % remove the last min
179       imin=imin(1:end-1);
180   end
181 distances=ymax-ymin; % in mm
```

```
182 if (sum(isnan(distances))>0)
183     TEXT='SU TAM NaN HODNOTY distances' %  this situation
        should not happen
184 end
185 d_average=mean(distances); % in mm
186 Lmax_average=mean(ymax); % in mm from the beginning of the
    anode
187 Lmin_average=mean(ymin); % in mm from the beginning of the
    anode
188 times=time(imax)-time(imin); % in us
189 t_average=mean(times); % in us
190 velocities=(distances./times)*1e3; % in m/s
191 v_average=MY_nanmean(velocities); % in m/s % MY_nanmean is
    a mean fucntion that ignors NaNs
192 % if everything OK, NaNs values should not be generated
    and the standard
193 % mean function is enough
194
195 %% GENERATING THE OUTPUT (VYSTUP_M) OF THIS SCRIPT
196 VYSTUP_M(s,1)=v; % ambient pressure in mbar
197 VYSTUP_M(s,2)=v_average; % average attachment velocity in
    m/s
198 VYSTUP_M(s,3)=t_average; % average time of the attachment
    movement in microseconds
199 VYSTUP_M(s,4)=t_periods; % average restrike period in
    microseconds
200 VYSTUP_M(s,5)=d_average; % average distance travelled by
    the attachment on the anode in mm
201 VYSTUP_M(s,6)=Lmin_average; % average position on the
    anode where a new attachment is created (by the
    restrike) in mm
202 VYSTUP_M(s,7)=Lmax_average; % average position on the
    anode where a previoius attachment ceases to exist (
    during the restrike) in mm
203
204 if 1 %% UNCERTAINTIES CALCULATION
205 velocity=v_average;
206 U=0; % only because this variable is in the "
    UNCERTAINTIES_LOW" script
207 UNCERTAINTIES_LOW % the script with systematic
    uncertainties of various variables
208 % % uncertainty of L
209 std_d=2*uncertainty(3); % nasobok 2 lebo odcitavam 2
    hodnoty
210 Lmax_std=2*sqrt( (std(ymax)/sqrt(length(ymax))).^2 +
    uncertainty(3)^2 ); % level of confidence approximately
     95%
211 Lmin_std=2*sqrt( (std(ymin)/sqrt(length(ymin))).^2 +
```

```
    uncertainty(3)^2 );  % level of confidence
    approximately 95%
212
213 d_std=2*sqrt( (MY_nanstd(distances)/sqrt(length(distances
    (~isnan(distances))))).^2 + std_d^2 ); % level of
    confidence approximately 95%
214 % multiplication of 2, becasuse it represents 2*sigma =
    level of confidence  95 %
215 v_std_A=MY_nanstd(velocities)/sqrt(length(velocities(~
    isnan(velocities))));
216 % in m/s % MY_nanstd is a std fucntion that ignors NaNs
217 % if everything OK, NaNs values should not be generated
    and the standard
218 % mean function is enough
219 std_t=2*uncertainty(14);
220 t_std=2*sqrt( (std(times)/sqrt(length(times))).^2 + std_t
    ^2 );
221 v_std_B=v_average*sqrt( (std_d/d_average)^2  + (std_t/
    t_average)^2 ); % in m/s
222 v_std=2*sqrt( v_std_A^2 + v_std_B^2 ); % level of
    confidence approximately 95%
223 %%%%%
224 t_periods_std_A=((std(periods_max)/sqrt(length(periods_max
    ))) +(std(periods_min)/sqrt(length(periods_min))) )/2;
225 t_periods_std_B=sqrt((2*uncertainty(14)).^2);
226 t_periods_std=2*sqrt( t_periods_std_A^2 + t_periods_std_B
    ^2 ); % level of confidence 95%
227 %%%%%
228 else
229     v_std=0;
230 t_std=0;
231 d_std=0;
232 t_periods_std=0;
233 end
234 VYSTUP_M(s,8)=v_std;
235 VYSTUP_M(s,9)=t_std;
236 VYSTUP_M(s,10)=t_periods_std;
237 VYSTUP_M(s,11)=d_std;
238 VYSTUP_M(s,12)=Lmin_std;
239 VYSTUP_M(s,13)=Lmax_std;
240 s=s+1;
241
242 %% FIGURES DRAWING - optional part - only for visual
    checking of finded extrema
243 if strcmp(graphs,'1')
244 red=[1 0 0];
245 yellow=[1 1 0];
246 magenta=[1 0 1];
```

```
black=[0 0 0];
green=[0 1 0];
blue=[0 0 1];
cyan=[0 1 1];
brown=[0.7 0.5 0];
col={brown,yellow,magenta,black,green,blue,[0.15 0 0.75],brown,[0.5 0 0], [0.75 0 0.15], [0 0 0.5], [0 0.5 0], cyan};
figure(11)
plot(time/1e3,position,'x-m','MarkerSize',20);
hold on
plot(time(imax)/1e3,ymax,'ro','MarkerSize',28)
plot(time(imin)/1e3,ymin,'go','MarkerSize',25)
hold off
xlabel('time [ms]')
ylabel('position [mm]')
ylim([0 20])
set(gca,'fontsize',40,'fontweight','bold')
set(get(gca,'xlabel'),'fontsize',37,'fontweight','bold')
set(get(gca,'ylabel'),'fontsize',37,'fontweight','bold')
title([num2str(v),' mbar'])
 set(get(gca,'title'),'fontsize',40,'fontweight','bold')
grid on
set(gca,'LineWidth',4)
end
% %%%%%%%%%%%%%%%%%%%%%%%%%%%%%%%%%%%%%%%%%%%%%%%%%%%%%%%%%%%%%%%%%%%%%%%%%%%%%%%%%%%%%

clear a
end % end for j=J0:50:JN

TimeSpent = toc; %elapsed time (duraton of the processing of this script) in s
```

MATLAB script for finding attachment’s dwellings

It can be downloaded here:
`https://ln.sync.com/dl/096ff10c0/dewh8gz5-fe48zspk-42mkqxxf-4cfkwx4u`.
The password is SCRIPT3.

MATLAB script to calculate electrical conductivity

It can be downloaded here:
`https://ln.sync.com/dl/8e5e656f0/vthjavem-csruirsv-fwmttbcg-sijir78j`.
The password is SCRIPT2.

Drawings

Plasma torch drawings

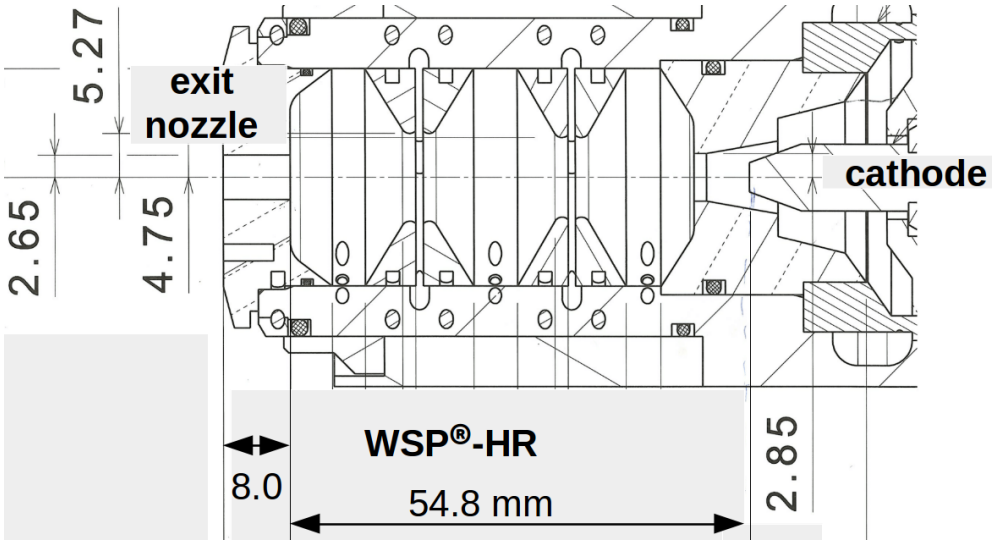

Figure 6.1: Engineering drawing of axial cross section of WSP®-HR

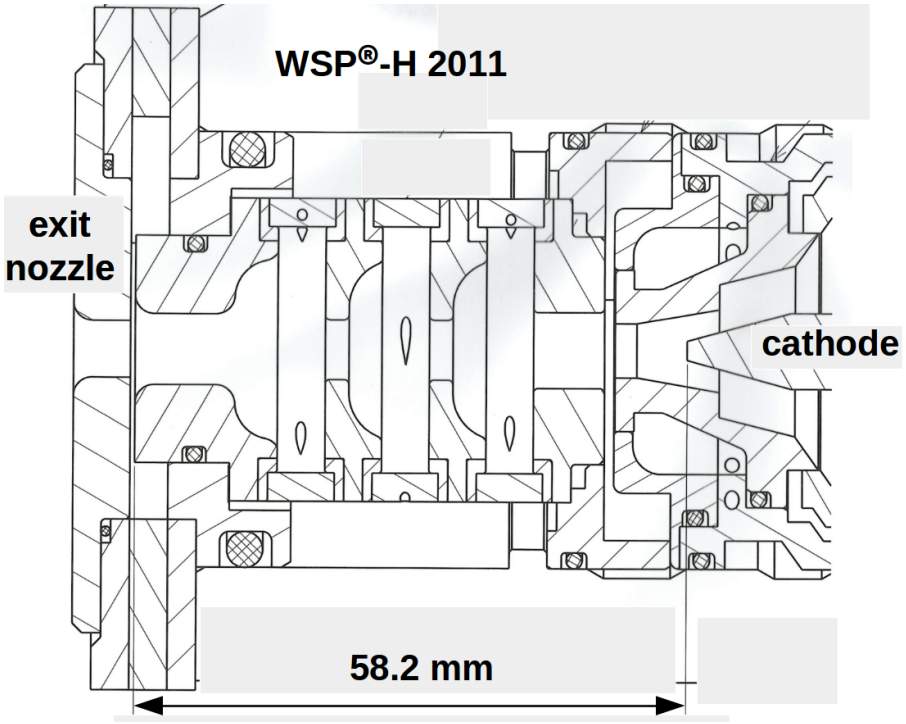

Figure 6.2: Engineering drawing of axial cross section of WSP®-H 2011

List of attached articles

(1) **Ondac P**, Maslani A and Hrabovsky M 2019 Experimental Investigation of Anode Arc Attachment Area in DC Arc Plasma Torch at Low Pressures *J. Phys. D: Appl. Phys.* **52** Art. No. 405201 (14 pages)
DOI: 10.1088/1361-6463/ab3197

(2) **Ondac P**, Maslani A, Hrabovsky M and Jenista J 2018 Measurement of Anode Arc Attachment Movement in DC Arc Plasma Torch at Atmospheric Pressure *Plasma Chem Plasma Process* **38** 637-654
DOI: 10.1007/s11090-018-9888-0

(3) **Ondac P**, Maslani A and Hrabovsky M 2016 Investigation of the arc-anode attachment area by utilizing a high-speed camera *Plasma Physics and Technology* **3** 1-4